



UNIVERSITÀ
DEGLI STUDI
DI PADOVA

Head Office: Università degli Studi di Padova, Via 8 Febbraio 2 35122 Padova

Department of Industrial Engineering

PHD COURSE: Industrial Engineering

CURRICULUM: Energy

COHORT: XXIX

**NUMERICAL MODELING AND FLUID-DYNAMIC
OPTIMISATION OF FUEL CELLS AND
FLOW BATTERIES SYSTEMS**

Coordinator: Prof. Paolo Colombo

Supervisor: Prof. Massimo Guarnieri

Co-Supervisor: Prof. Francesco Picano

PhD Candidate: Dario Maggiolo

This dissertation is submitted for the degree of
Doctor of Philosophy

This work has been supported by the strategic
project MAESTRA funded by the University of Padova

January 2017

“What is great in man is that he is a bridge and not a goal.”

Friedrich Nietzsche

Declaration

I hereby declare that except where specific reference is made to the work of others, the contents of this dissertation are original and have not been submitted in whole or in part for consideration for any other degree or qualification in this, or any other university. This dissertation is my own work and contains nothing which is the outcome of work done in collaboration with others, except as specified in the text and Acknowledgements.

Dario Maggiolo
January 2017

Acknowledgements

First I would like to acknowledge my family, my parents and my brothers for teaching me values of curiosity, liberty, respect, humility and self-awareness. The challenge they offered me to find my own way was the greatest of my life.

I would like to acknowledge my supervisor, Massimo Guarnieri, who have always supported me all throughout my PhD project. I have always felt my work to be welcomed and appreciated and I must be grateful for this.

Also I would like to thank all the person who have strongly supported my academic work throughout my career, Federico Toschi and Andrea Marion with whom I have enjoyed sharing my ideas and from whom I have learnt a lot. They have been fundamental in rising my self-confidence.

A very special thanks goes to Francesco Picano and Costantino Manes. They both have introduced me to the world of fluid dynamics and have instilled in me the love for science, often more as friends, rather than as teachers.

I also would like to acknowledge my colleagues in Padova, Francesco, Davide, Mattia, Andrea, Paolo and my colleagues in Eindhoven, Gianluca, Francesca, Matteo, Alessandro, Abhineet (and Achint), Wolfram, Hadi, Sebastian, Steven, Kim, Marlies, Samuel, Xiao, Jonathan, Matias, Beppe, Vittorio, Philippos and Andrea. I would like to thank my friends (of all kind) that made my life better all along. A final special thanks to music and all musicians who have been playing with me so far.

Abstract

Nowadays, the energy challenge is one of the largest driving forces behind many research efforts. Future energy strategies include smart ways to store and convert energy on demand. On this exciting perspective, fuel cells and flow batteries play a key role, the former in converting energy into propulsion, the latter in storing renewable energy surplus. Nevertheless, some main technological issues still must be overcome, such as limited peak performances often caused by poor fluid-mechanic efficiency. The fluid-dynamic optimisation of fuel cells and flow batteries systems is the main aim of the present thesis work. To this end, the focus is set on studying liquid-vapour two-phase flows and dispersion dynamics in fibrous porous media, by means of Lattice-Boltzmann numerical models, in order to catch the effects of microscale phenomena on macroscale features of both technologies. Present findings offer new insights into understanding fundamental physical behaviours in fuel cells and flow batteries, and give a guideline for good and innovative design practice.

Table of contents

1	Introduction	1
1.1	Green Decarbonated Energy	1
1.2	PEM Fuel Cells	2
1.3	Redox Flow Batteries	5
1.4	Outline of the thesis	6
2	Numerical Methodology	9
2.1	The Lattice-Boltzmann Method	9
2.1.1	From the Boltzmann Equation to Navier-Stokes	9
2.1.2	The Lattice Gas Cellular Automata	14
2.1.3	The Lattice-Boltzmann Equation	16
2.2	Multi-Relaxation Method	19
2.3	Two-phase flows	20
2.4	Two-phase thermally-coupled flows	22
2.5	Interpolation bounce-back algorithm	22
2.6	Model validation	24
3	Fluid Dynamics in Fuel Cells	31
3.1	Characteristic length scales in fuel cells	31
3.2	Water management and liquid water cumulation in fuel cells	32
3.2.1	Introduction	32
3.2.2	Simulations of water cumulation	34
3.2.3	Remarks	41
4	Drainage Dynamics in Fuel Cells	43
4.1	Fuel cells drainage and wettabilities	43
4.2	Wettability effects on imbibition and drainage in porous media	45
4.2.1	Introduction	45

4.2.2	Simulations of imbibition and drainage dynamics	47
4.3	Simulations of condensation and drainage in fuel cells	62
5	Fluid Dynamics in Flow Batteries	67
5.1	Design of flow batteries	67
5.2	Study on electrolyte distribution in redox flow batteries	68
5.2.1	Introduction	68
5.2.2	Set-up and numerical methods	69
5.2.3	Simulations of electrolyte distribution	73
5.2.4	Remarks	78
6	Dispersion Dynamics in Flow Batteries	81
6.1	Dispersion dynamics in porous media	81
6.2	Anisotropy effects on dispersion in fibrous porous media	82
6.2.1	Introduction	82
6.2.2	Methodology	84
6.2.3	Simulations of dispersion	86
6.2.4	Remarks	100
7	Conclusions	103
	List of figures	107
	List of tables	113
	References	115

Chapter 1

Introduction

1.1 Green Decarbonated Energy

Nowadays, the rapid rise of green decarbonated energy demand provides new opportunities for scientific community to participate in renewable energy technology development. The energy challenge is one of the main topic in the European framework programme Horizon 2020. From chemists to biologists and from engineers to physicists, the need of new general understanding about renewal energies involves many scientific fields.

Among all the European calls of Horizon 2020, the fuel cell topic is of great importance in the short term perspective of the European community. For instance, the second call Fuel Cells and Hydrogen Joint Undertaking (FCH2 JU) “aims to accelerate the commercial development of hydrogen-based energy and transport solutions across Europe through a total investment of €1.33 billion”.¹ The main target for the scientific and industrial community is to improve fuel cells performances and reduce the cost of products in order to prove their competitiveness in the mobility market. In fact, while the fuel cells technology is well known since the second half of the twentieth century, several technological and industrial issue still remain in order to make them ready for the global market. [1]

In future fuel cells are expected to dominate the electric automotive sector along with batteries and hybrid vehicles. Instead, their application to the stationary storage is considered secondary, even though, at present, they are already well exploited to this aim, e.g. in Combined Heat and Power (CHP) systems. Projects of 1 MW and larger fuel cell batteries have been undertaken, while smaller fuel cells in the range of 50-75 kW have been developed for automotive applications. Anyway, their low emission feature strongly promote them to be applied for transportation, simply because they appear to be the most efficient and clean way

¹<http://www.fch.europa.eu/>

to convert energy into propulsion, being characterised by larger range and faster refuelling in comparison with batteries. [2, 3] On this perspective, fuel generation and storage, as well as the delivery infrastructure and the limited peak performances are still significant issues. [3]

Redox Flow Batteries (RFBs, also called “flow batteries”) are instead believed to potentially solve the problem of stationary energy storage. RFBs are similar to fuel cells but they are closed systems, that means the fuel must not be supplied from outside. Rather, the reduction and oxidation (from which the term “redox”) reactions occur inside the cell which, in turn, hosts fully reversible chemical reactions. [4] The reversibility and scalability of this technology are the characteristics which make RFBs appealing as part of the European strategy for future energy storage. [1]

The present thesis deals with transport phenomena, from gas distribution to liquid movement and condensation, in fuel cells and flow batteries, by means of advanced computational fluid dynamics. In the current Chapter 1 a brief introduction to fuel cells and redox flow batteries will be given along with the state-of-art and still-open issues of both technologies. In the next Chapter 2 the numerical methodology used for simulating flows will be presented. Chapter 3 regards a study of liquid water cumulation in fuel cells, focusing on implication on cell design. Chapter 4 instead will present results of simulations of liquid imbibition and drainage in unsaturated fibrous porous media. Chapter 5 will largely describe the combined effect of flow and dispersion in redox flow batteries and finally Chapter 6 will summarise the main results and attainments.

1.2 PEM Fuel Cells

The present study focuses on Polymer Electrolyte Membrane Fuel Cells (PEMFC or PEM Fuel Cells). PEM fuel cells are electro-chemical energy converters. They are composed of two graphite plates, named “bipolar plates”, with engraved Gas Channels (GCs) that provide fuel distribution over the active area as well as current collectors, two fibrous porous media which serve as gas distributors, and a proton exchange membrane that prevent electrons passage, see Fig. 1.1. The fuel is hydrogen and it is continuously supplied to the anode side while at the cathode oxygen is provided as oxidising agent. During the chemical reaction in the cell, fuel donates electrons from the anode side of the membrane while oxidising receives them on the other side after they have migrated in the external circuit. The membrane acts as an electrical insulator while allowing proton transport. In turn, the electrons transport occurs in the external electrical circuit where they produce electrical work. [3]

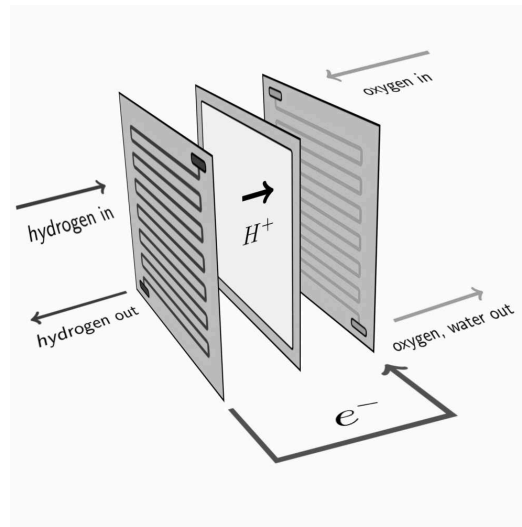
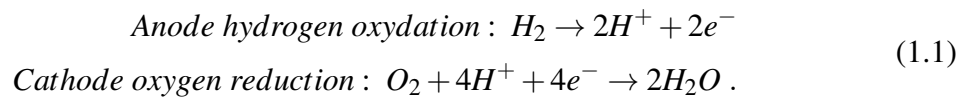


Fig. 1.1 Sketch of a fuel cell.

The global oxidation and reduction reactions occurring at the anode and cathode are:



It should be stressed that many alternatives exist to describe the latter reactions, depending on the kind of fuel cell and fuel (methane and methanol are also used in other fuel cells). Moreover, the full chain of subsequent chemical reactions in real systems is much less trivial than the one expressed in Eq. 1.2; anyway this is beyond the purpose of the present work and the reader is suggested to consult more specific publications for a thorough description of the full chain of reactions, see e.g. [5].

Porous media act as electrodes by hosting chemical reactions in a thin region of themselves, i.e. the catalyst layer (CL), as well as by conveying electrons to the current collectors. Given their porous microstructure, they also facilitate the distribution of species all over the catalyst layers, so that they are usually called Gas Diffusion Layers (GDLs). GDLs are usually characterised by high porosity, i.e. $\varepsilon = 0.7 \div 0.9$, and composed by carbon fibers randomly distributed throughout the media. From a fluid-dynamic point of view, the GDL is the most interesting part of the cell since the pertinence of classic macroscopic equation for modelling mass and momentum transport in porous media is still on debate. [6–8]

The very complex transport phenomena inside GDL greatly affects fuel cell performances. In fact, the current density of the cell is generally limited by two main factors: activation over-potential and mass transport losses. The former and the latter dominate the low-current and the high-current operative conditions, respectively, while the ohmic losses are present

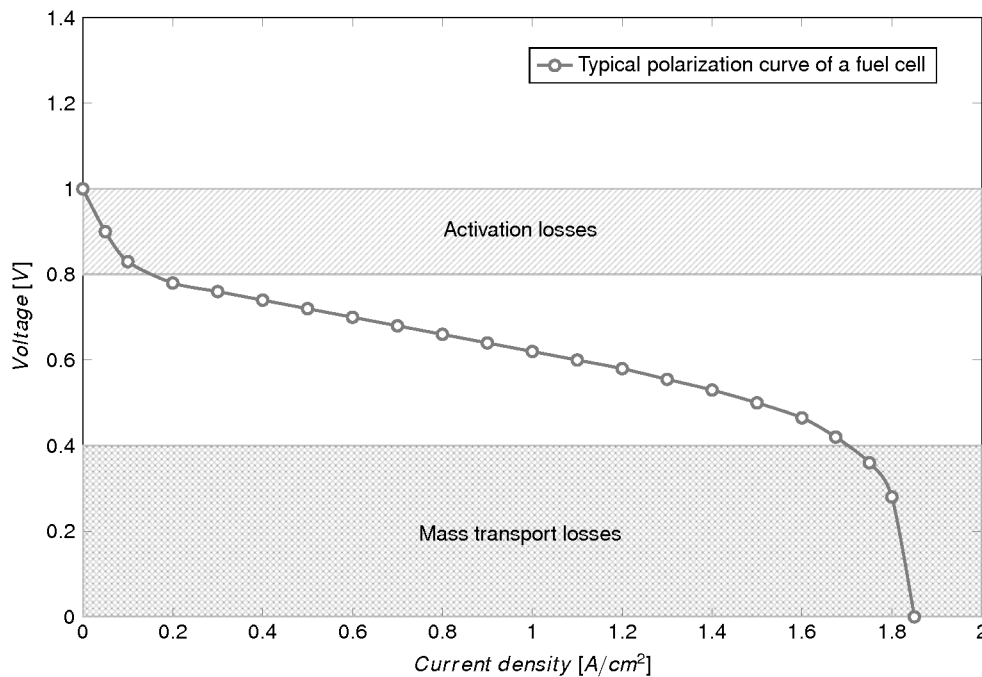


Fig. 1.2 Polarisation curve of a cell. The activation and mass transport losses are highlighted.

particularly in the membrane, due to proton motion, but have a smaller impact on current density, see Fig. 1.2. From Fig. 1.2 it is also clear that the mass transport losses are generally considered responsible of the dramatic decrease of the voltage at high current densities. They are also associate with the flooding phenomenon, that is, the significant presence of water in liquid form inside the GDL which potentially limits the gas diffusion.

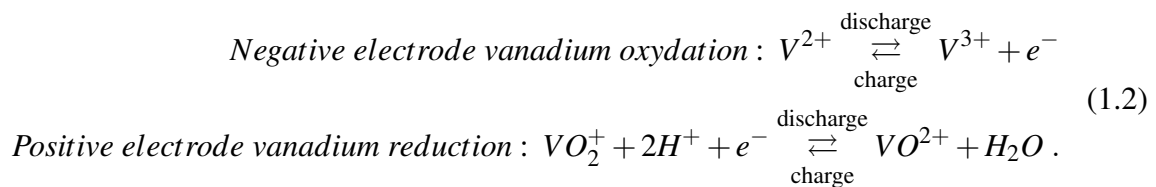
The bottlenecks of fuel cell technology are the limited performances at high current densities and the cost of the catalyst layer. Other issues are cold start and safe hydrogen storage. Recently, the Japanese company Toyota launched their commercial vehicle *Toyota Mirai*. The Mirai is the first vehicle able to reach global market standards, in terms of cruising range and peak performances, even if it is still quite expensive. Toyota engineers claimed that this improvement have been possible thanks to some new features in the cell stack, in particular the new design of the distribution channels and gas diffusion layers. [9] The innovative design is described as “three-dimensional”, in order to stress the change of gas and liquid transport inside the cell, which is generally approximated as two-dimensional in fuel cell computational models. Moreover, authors highlight the prominent role which hydrophobicity is playing in order to manage the liquid water transport.

1.3 Redox Flow Batteries

Redox flow batteries are electro-chemical energy conversion devices, in which a fully reversible redox processes of species in fluid solution take place. The solutions are stored in external tanks. Appealing features of RFBs are: scalability and flexibility, independent sizing of power and energy, high round-trip efficiency, long durability, fast responsiveness, and reduced environmental impact. [4] These benefits make RFBs capable of assisting electricity from renewable sources, by storing the excess of generated energy. In fact, in RFBs, power and energy are separated and easily tunable, by adjusting the number of cells and the size of tanks, respectively. Thus, they can be easily adapted for different kind and size of energy storage, at a minimum cost. [4, 10]

The technology of RFBs is known since the late 1980s, but just recently it has gained popularity, along with the rapid rise of chemical and engineering technology for energy applications. [11] RFBs can be supplied with different kind of electrolyte solutions, from iron-chromium to zinc-bromine, and from vanadium-bromine to vanadium-vanadium. Among all, today the vanadium-vanadium electrolytes are promising to overcome some drawbacks of this technology, such as cross-over contamination. The vanadium solutions are able to hold four stable oxidation states of the vanadium element; these oxidation states exchange between themselves electrons and protons inside the cell to produce electric work. [4] The presence of four stable state of the same chemical element significantly reduces the performance drop caused by cross-contamination inside the cell, from cathode to anode and viceversa, allowing for a high cell capacity for long time. This is the main benefit of using all-Vanadium Redox Flow Batteries (VRFBs).

Vanadium is dissolved in an aqueous sulphuric acid with some differences in the metal ion charge oxidation at the electrodes: vanadium IV–V (tetra- valent–pentavalent) is used on the positive side and vanadium II–III (bivalent–trivalent) on the negative. The half-reactions reads as follows:



From the above equation, it is clear the similarity with fuel cells, with a major difference: the reversibility of the reactions fully inside the cell. As in fuel cells, the migration of hydrogen ions H^+ is promoted by a proton exchange membrane, while electrons are transported in an external circuit. The typical current density of all-vanadium cells is in the order of $5 \div 8 \cdot 10^2$

A/m², to which correspond a lower power density compared to PEMFCs. This limitation on power density, along with the intrinsic scalability of the technology, suggests the use for stationary applications.

Regarding the state of art of VRFBs, during recent years, several power plants based on such technology have been built. Among them, the plant installed by SEI for J-Power in 2005 is the largest, with a capacity of 4 MW / 6 MWh. The plant has 96 stacks rated about 1 MW which consist of 108 cells each one. [4] From the academic perspective much has been done for achieving a better knowledge of the physical phenomena inside VRFBs. As for fuel cells, the chemical behaviour is very complex. For this reason chemists are spending efforts in understanding the full chain of electro-chemical reactions in order to enhance reactions and limit secondary products, see e.g. Kim *et al.* [12] The fluid mechanics is complex as well. The microstructure of the electrode which act both as fluid mixers, active surfaces (conversely to fuel cells) and current collectors, is typically composed of randomly placed carbon fibers. Such complex structure is able to spread and diffuse vanadium species all along the cell, even if it is not known to what extent this diffusion process can be enhanced.

1.4 Outline of the thesis

The present thesis deals with the fluid-dynamic optimisation of fuel cells and flow batteries systems, from the micro to the macro scale. The fluid-dynamic study has been carried out by means of numerical simulations based on the Lattice-Boltzmann Method. Figure 1.3 schematises the thesis structure and the content of every chapter.

The main question that this study tries to address is: “Is it possible to improve fuel cells and flow batteries performances by improving the fluid dynamics of the systems? And if yes, how?”. In order to answer these questions, the present study is focused on water management in fuel cells and dispersion of species in flow batteries. Indeed, these aspects are considered crucial for increasing peak performances of such systems.

In fuel cells the optimal water management strategy would enhance gas transport to the gas diffusion layers and catalyst layers while promoting liquid water removal. This strategy can be achieved by identifying the optimal micro and macro structure design and tuning the microscopic properties of cell components. In Chapter 3 the main mechanism of liquid water cumulation and its dependence on GDL and GC macroscopic design will be investigated. Several simulations with varying the cell design will be analysed. These simulations aim to investigate the case when water erupts from the catalyst layer in vapour form. Water can also be transported from catalyst layers to diffusion layers in liquid form; this issue will be investigated in Chapter 4. The dynamics of liquid infiltration and drainage in fibrous porous

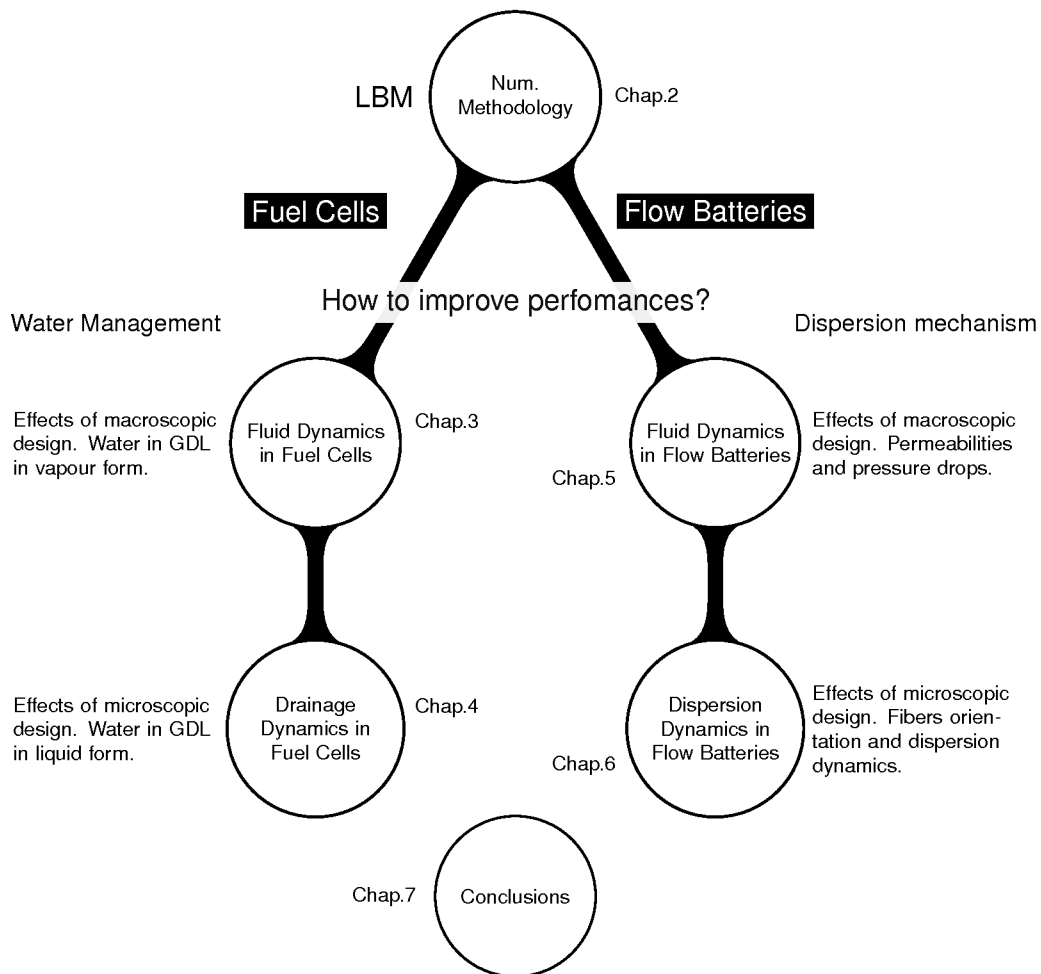


Fig. 1.3 Schematic outline of the present thesis.

media and the effects of material hydrophobicity will be discussed in order to establish the optimal design of a fuel cell which promotes liquid water removal from the diffusion layers.

In Chapter 5 some main issues related to flow batteries technology will be briefly discussed, focusing on fluid-dynamics aspects, and a study of the effect of distribution-channels macroscopic design on electrolyte distribution in RFBs will be presented. In Chapter 6 a thorough study of dispersion mechanisms inside porous media will be presented and an optimal configuration of the porous microstructure for RFBs applications will be identified.

In the next Chapter 2 the Lattice-Boltzmann numerical methodology and its applicability to the cases discussed in the present thesis work will be discussed, as well as the model validation.

The present thesis work has been supported by the strategic project MAESTRA funded by the University of Padova with 809 k€.

Chapter 2

Numerical Methodology

2.1 The Lattice-Boltzmann Method

The Lattice-Boltzmann Method (LBM) is an alternative way to solve Navier-Stokes equations. It has been developed from its ancestor method, the Lattice Gas Cellular Automata. The LBM solves the Boltzmann Transport equation which determines the statistical distribution of fluid molecules at the mesoscale.

Without going into the details of its formulation and derivation, the Boltzmann equation is inherently different of its macroscopic counterpart, that is, Navier-Stokes equation: while the latter satisfies the mass and momentum conservation laws at the macroscale, the former satisfies them at the mesoscale in the theoretical framework of kinetics and statistical mechanics. [13] In comparison with conventional Navier-Stokes solvers, the main advantages of the Lattice-Boltzmann Method are its capability of easily handling multiphysics problems and the ease with which it can be parallelised. Sure enough, it is extensively used for directly solving two-phase flows without tracking the interface or flows in complex geometries, in a regular computational grid perfectly suited for parallelisation.

2.1.1 From the Boltzmann Equation to Navier-Stokes

The Boltzmann Transport equation describes the physical state of a thermodynamic system through the distribution functions $f(\vec{x}, \vec{p}, t)$. Let be m the mass and \vec{v} the velocity of a particle; if \vec{x} is the particle position and $\vec{p} = m\vec{v}$ its momentum, the distribution function $f(\vec{x}, \vec{p}, t)$ conveys the probable number of fluid particles with such velocity in such position, that is:

$$\Delta n = f \Delta \vec{x} \Delta \vec{p} \tag{2.1}$$

Actually, Eq. (2.1) describes the probable number of fluid particles in the neighbourhood $(\vec{x} \pm \Delta\vec{x}, \vec{p} \pm \Delta\vec{p})$. Taking into account one particles (*one-body kinetic level*) the Boltzmann equation reads as:

$$\left\{ \frac{\partial}{\partial t} + \frac{\vec{p}}{m} \cdot \frac{\partial}{\partial \vec{x}} + \vec{F} \cdot \frac{\partial}{\partial \vec{p}} \right\} f(\vec{x}, \vec{p}, t) = \int (\hat{f}_{12} - f_{12}) g \sigma(g, \vartheta) d\vartheta d\vec{p} \quad (2.2)$$

where \vec{F} is the external forcing, \hat{f} the post-collision distribution, σ the differential cross section of the collision, $g = \vec{v}_1 - \vec{v}_2$ the relative velocity and ϑ the characteristic angle of collision.

Equation (2.2) can be shortly written as:

$$\mathcal{S}f = \mathcal{C}_{12} \quad (2.3)$$

The Boltzmann Transport equation describes the relationship between the *streaming* operator \mathcal{S} , that is the “free streaming” of particles along their trajectories, and the *collision* operator \mathcal{C}_{12} , which represents the collision between two particles 1, 2 and, consequently, involves the probable state of two particles (*two-body kinetic level*). These particles, in turn, depend on trajectories and collisions of others and so on.¹

Boltzmann thus conceived the hypothesis of *molecular chaos* for which particles going to collide are completely independent each other: [13, 14]

$$f_1 f_2 = f_{12} \quad (2.4)$$

To what extent this assumption can be applied to liquids, which are characterised by high density, has been subject to a great debate. Without entering into the merits of this debate, it should be stressed that several studies has demonstrate its applicability to liquids dynamics.

In the Boltzmann equation the distribution function at the thermodynamic equilibrium satisfies the condition of *local equilibrium*. Local equilibrium is defined as the state in which particles entering the local fluid element are perfectly balanced by the outgoing one. In this state the collision operator is null, not because there are no collisions, but rather because collisions are balanced along different directions. Consequently at equilibrium $\mathcal{C}^e = 0$, from which it follows:

$$\hat{f}_1 \hat{f}_2 = f_1 f_2 \quad (2.5)$$

¹ f_{12} is the probability to find the particle 1 in $\Delta\vec{x}_1$ with velocity $\Delta\vec{v}_1$ and the particle 2 in $\Delta\vec{x}_2$ with velocity $\Delta\vec{v}_2$ at the same instant t .

In logarithmic form:

$$\ln \hat{f}_1 + \ln \hat{f}_2 = \ln f_1 + \ln f_2 \quad (2.6)$$

Equation (2.6) states that the variable $\ln f$ is an additive invariant of collision. Thus, if the fluid is in a state of thermodynamic equilibrium, $\ln f$ will be a function of the collision invariants, i.e the conserved properties during collision: the particle number, the momentum and the energy $\mathcal{I} = (1, m\vec{v}, mv^2/2)$ These collision invariants are related to their macroscopic counterparts as follows:

$$\begin{aligned} \rho &= m \int f d\vec{v} \\ \rho u_i &= m \int f v_i d\vec{v} \\ \rho e &= m \int f \frac{v^2}{2} d\vec{v} \end{aligned} \quad (2.7)$$

where m is the mass, ρ is the density, u_i the macroscopic velocity and ρe the energy density.² The variable $\ln f$ can then be written in polynomial form:³

$$\ln f = A + B_i v_i + \frac{1}{2} C v^2 \quad (2.8)$$

It should be noted that the “contact point” between microscopic and macroscopic world is the *equilibrium distribution function* f^e , which inherently satisfies the local equilibrium condition. The latter can be expressed by means of the Maxwell-Boltzmann formulation:

$$f_i^e = \rho (2\pi v_T^2)^{-D/2} e^{-\omega_i^2 v_T^2 / 2} \quad (2.9)$$

where $\omega_i = v_i - u_i$ is the relative velocity, D the number of dimensions, $v_T = \sqrt{k_B T / m}$ the thermal velocity, T the temperature and k_B the Boltzmann constant.⁴

Fluids tend to local equilibrium and this tendency is called *local equilibrium relaxation*. Thermodynamic equilibrium can be reached globally, that is when fluid velocities and temperature are constant throughout the domain, and the fluid can be defined in *global equilibrium*.

The fluid relaxation towards equilibrium can be characterised by three main timescales corresponding to three different dynamic steps:

²the subscript i indicates a Cartesian coordinate components.

³ A , B and C are generic polynomial coefficients.

⁴ v_T is the mean quadratic velocity of the Maxwell-Boltzmann distribution

- fast relaxation towards *one-body* distribution, with the timescale t_{int} ;
- relaxation towards local Maxwellian equilibrium distribution, with time and spatial-dependent hydrodynamic variables. The timescale is $t_\mu = l_\mu/v$;
- slow relaxation towards global Maxwellian equilibrium, with hydrodynamic variables constant in time and space. The timescale is $t_M = l_M/v$.

In the aforementioned formulation, l_{mu} is the *mean free path* of particles, while l_M is a characteristic macroscale length. Summarising:

$$f_{1,2\dots N} \xrightarrow{t_{int}} f_1 \xrightarrow{t_\mu} f^e(v, u, T) \xrightarrow{t_M} f^e(v_0, u_0, T_0) \quad (2.10)$$

Citing Sauro Succi:

the fluid dynamics can be seen as the (family) picture that emerges from the study of the kinetic equations. [13]

From the above sentence, the meaning of the LBM appears more clear: a junction between variables at different space and time-scales, i.e. the microscopic and the macroscopic scale. In order to prove that Boltzmann equation leads to the Navier-Stokes equation at the macroscopic scale, a multiscale expansion can be performed. In practice, it consists in treating each variable with its own scale. Among all, the Chapman-Enskog multiscale expansion is one the most famous tool:

$$\begin{aligned} f &= f^e + \varepsilon f^{ne} \\ x &= \varepsilon^{-1} x_1 \\ t &= \varepsilon^{-1} t_1 + \varepsilon^{-2} t_2 \\ \partial/\partial x &= \varepsilon \partial/\partial x_1 \\ \partial/\partial t &= \varepsilon \partial/\partial t_1 + \varepsilon^2 \partial/\partial t_2 \end{aligned} \quad (2.11)$$

In Eq. (2.11) x_1 e t_1 refer to the speed of sound scale while t_2 is the timescale of hydrodynamic diffusion. The streaming operator can be rewritten on the basis of Eq. (2.11) along the Cartesian coordinate i (being j the other coordinate):

$$\mathcal{S}_t = \varepsilon \frac{\partial}{\partial t_1} + \varepsilon^2 \frac{\partial}{\partial t_2} + \varepsilon v_i \frac{\partial}{\partial x_{1i}} + \frac{1}{2} \varepsilon^2 v_i v_j \frac{\partial}{\partial x_{1i}} \frac{\partial}{\partial x_{1j}} \quad (2.12)$$

Following the same logic, the collision operator becomes:

$$\mathcal{C}(f) = \mathcal{C}(f^e) + \varepsilon \mathcal{C}(f^{ne}) \quad (2.13)$$

At equilibrium the collision operator is null, see Eq. (2.5). If one multiplies Eqs. (2.12) and (2.13) by any collision invariant \mathcal{I} and integrates in the domain $d\vec{v}$ Eq. (2.2), (he) obtains:

$$\begin{aligned} \int \left[\varepsilon \frac{\partial}{\partial t_1} + \varepsilon^2 \frac{\partial}{\partial t_2} + \varepsilon v_i \frac{\partial}{\partial x_{1i}} + \frac{1}{2} \varepsilon^2 v_i v_j \frac{\partial}{\partial x_{1i}} \frac{\partial}{\partial x_{1j}} \right] \mathcal{I} f d\vec{v} = \\ = \int \varepsilon \mathcal{I} \mathcal{C}(f^{ne}) d\vec{v} = 0 \end{aligned} \quad (2.14)$$

The integral of the collision operator in the domain $d\vec{v}$ must be null in order to do not violate the conservation law of number of molecules. In order to get the macroscopic hydrodynamic variables, the collision invariant $\mathcal{I} = (1, m\vec{v}, mv^2/2)$ and the the proper scale, ε or ε^2 , must be chosen. For instance, the continuity equation can be attained from Equation (2.14) by choosing $\mathcal{I} = 1$ and ε :

$$\int \varepsilon \mathcal{I} \frac{\partial f}{\partial t_1} d\vec{v} + \int \varepsilon \mathcal{I} v_i \frac{\partial f}{\partial x_{1i}} d\vec{v} = 0 . \quad (2.15)$$

Equation (2.15) can be rewritten as:

$$\frac{\partial}{\partial t_1} \int \mathcal{I} f d\vec{v} - \int f \frac{\partial \mathcal{I}}{\partial t_1} d\vec{v} + \frac{\partial}{\partial x_{1i}} \int \mathcal{I} v_i f d\vec{v} - \int f v_i \frac{\partial \mathcal{I}}{\partial x_{1i}} d\vec{v} = 0 . \quad (2.16)$$

Since \mathcal{I} is not time dependent, the second member of Eq. (2.16) is null. Finally, on the basis of the definitions given in Eq. (2.7) and imposing $\mathcal{I} = 1$, the continuity equation can be derived:

$$\frac{\partial \rho}{\partial t_1} + \frac{\partial(\rho u_i)}{\partial x_{1i}} = 0 \quad (2.17)$$

In a similar matter one can derive Navier-Stokes equations by imposing $\mathcal{I} = m\vec{v}$ with the scale ε^2 . It should be lastly noted that the system tends to local equilibrium in a faster time t_1 in comparison with the time t_2 required to reach global equilibrium by diffusing momentum. The Navier-Stokes equation results:

$$\frac{\partial u_i}{\partial t_2} + u_j \frac{\partial u_i}{\partial x_{1j}} = -\frac{1}{\rho} \frac{\partial p}{\partial x_{1i}} + \nu \frac{\partial^2 u_i}{\partial x_{1j}^2} + \frac{F_i}{m} \quad (2.18)$$

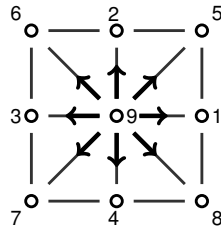


Fig. 2.1 Two-dimensional lattice cell in LGCA and in LBM

2.1.2 The Lattice Gas Cellular Automata

The ancestor of the Lattice-Boltzmann Method is the Lattice Gas Cellular Automata (LGCA). It is based on the *cellular automaton*, a mathematical model developed in the first 1950s: the space is divided in discrete parts (the cells) to each of which a proper condition or state subjected to some set of rules is assigned. In 1986 Frisch, Hasslacher e Pomeau [15] introduced a new set of rules in order to satisfy the laws of the fluid dynamics which gave rise to the Lattice Gas Cellular Automata method.

In the LGCA method the domain decomposition into cells can be several on the basis of the cells shape, e.g. squared or hexagonal. Figure 2.1 shows a two-dimensional example of a squared cell of a lattice. Each cell consists of some “links” which are addressed by the vector $\vec{c}_r \equiv [c_{ri}, c_{rj}]$, with $r = 1, \dots, 9$ and $i, j = x, y$ (Cartesian coordinates), and which connect the cell to the others. Moreover, each cell can host up to 8 fluid particles, provided that all the following rules are satisfied:

- all particles have the same mass $m = 1$;
- each particle can move along just one direction \vec{c}_r in a single time interval;
- by the end of this time interval, each particles will move from the position \vec{x} to the position $\vec{x} + \vec{c}_r$;
- two particles in the position cannot move along the same direction (*exclusion principle*).

Surprisingly, even though the aforementioned rules are apparently so far from the real nature of fluids, they can describe a flow field with sufficient accuracy.⁵ The latter rules allows to univocally define the condition of each cell of the lattice at any instant of time; the two possible states are defined by the *occupation number* n_r :

⁵In a real gas particles can move in an infinite number of directions and velocities.

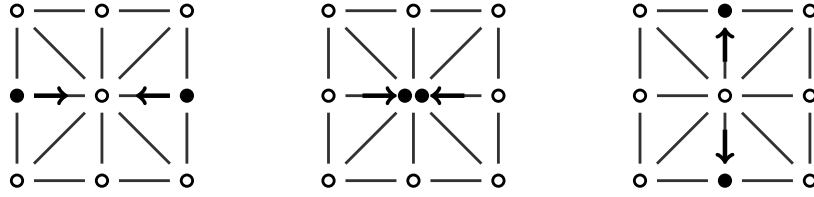


Fig. 2.2 Example of collision in LGCA

$$\begin{aligned} n_r(\vec{x}, t) &= 0 \quad \text{no particles} \\ n_r(\vec{x}, t) &= 1 \quad \text{particle is present} \end{aligned} \quad (2.19)$$

In the LGCA method the streaming operator describes the particle transfer from one position to another one while the collision operator describes the possible change of direction of particles that collide with others:

$$\mathcal{S}_r n_r = n_r(\vec{x} + \vec{c}_r, t + 1) - n_r(\vec{x}, t) \quad (2.20)$$

$$\mathcal{C}_r(n_1, \dots, n_9) = \tilde{n}_r(\vec{x}, t) - n_r(\vec{x}, t) \quad (2.21)$$

where \tilde{n} indicates the post-collision state. If $\mathcal{S} = 0$, the particle is free to move and there is not collision $\mathcal{C} = 0$. Conversely, if there is collision, the particle will move to another position following the rules of the lattice. In the example given in Fig. 2.2, the cell is squared and its state is $(n_1, \dots, n_9) = [101000000]$; the collision operator transforms the state in $[010100000]$ and the two particles can eventually move from n_1 to n_2 and n_3 to n_4 .

In order to simulate fluids, the possible collisions in this system must satisfy the conservation laws of mass and momentum, and one more condition: the *rotational invariance* of Navier-Stokes equations. Therefore one must choose the shape of the cell among the possible shapes which respect to this condition.

Summarising, the equation of the LGCA method is:

$$\mathcal{S}_r n_r = \mathcal{C}_r(\underline{n}) \quad , \quad (2.22)$$

where $\underline{n} = (n_1, \dots, n_9)$. The same equation can be written as follow:

$$n_r(\vec{x} + \vec{c}_r, t + 1) = \tilde{n}_r(\vec{x}, t) \quad . \quad (2.23)$$

The funny story of the LGCA is that it was not really conceived at the beginning for simulating fluid flows, but rather for applications in computer processors and cryptography.

Only later, the logic of *cellular automaton* was surprisingly found to be able to describe the behaviour of viscous flows at the macroscopic scale.

2.1.3 The Lattice-Boltzmann Equation

One of the major drawback of the LGCA method is the statistical noise. In fact, every “particle method” (i.e. every method which describe the properties of each particle) is inherently characterised by a great number of statistical fluctuations. In order to deal with this excess of information and make the method computationally efficient, McNamara and Zanetti in 1988 [16] substituted the Boolean value of the occupation number with the corresponding spatial and temporal mean value. More to the point, instead of assigning one particle to a specific position, they assigned the mean probability to find a particle to that specific position. Even though this procedure filters a lot of information from the microscale, it reduces the statistical noise at the hydrodynamic macroscale.

From the mathematical point of view, the occupation number can be split into two parts: the mean $f_r = \langle n_r \rangle$ and its fluctuation r_r :

$$n_r = f_r + r_r \quad . \quad (2.24)$$

By substituting Eq. (2.24) in Eq. (2.22) it results:

$$\mathcal{S}_r f_r = \mathcal{C}_r(\underline{f}) + R_r \quad (2.25)$$

where R_r indicates all the fluctuations around the mean value. If particles are uncorrelated, each of them will have the same probability of being in a specific position with a given velocity so that $R_r = 0$. Actually this corresponds to the *molecular chaos* hypothesis [14]. With this hypothesis, the non-linear formulation of the Lattice-Boltzmann equation can be obtained as:

$$\mathcal{S}_r f_r = \mathcal{C}_r(\underline{f}) \quad (2.26)$$

The non-linearity is intrinsic in the collision operator. It should be noted that Boolean variables in Eq. (2.26) have been substitute with continuous variables which require higher computational efforts; nevertheless this drawback is widely compensated by the lower computational efforts required to compute the statistical noise.

Another drawback is the non linearity of the collision operator. In order to overcome this issue McNamara e Zanetti [16] and Higuera e Jimenez [17] contemporary suggested to use

the Chapman-Enskog procedure. In particular they both proposed to expand the variable f around its global equilibrium value f_r^{e0} , so that Eq. (2.11) results:

$$f_r = f_r^{e0} + f_r^{e1} + f_r^{e2} + f_r^{ne} + O(\mathcal{M}^2) , \quad (2.27)$$

where \mathcal{M} is the Mach number. In a similar manner the collision operator along the generic direction r (being $r2, r3$ other directions) can be rewritten as:

$$\begin{aligned} \mathcal{C}_r(f) = & \mathcal{C}_r \Big|_{f_r^{e0}} + \frac{\partial \mathcal{C}_r}{\partial f_{r2}} \Big|_{f_r^{e0}} (f_{r2}^{e1} + f_{r2}^{e2} + f_{r2}^{ne}) \\ & + \frac{1}{2} \frac{\partial^2 \mathcal{C}_{r2}}{\partial f_{r2} \partial f_{r3}} \Big|_{f_r^{e0}} (f_{r2}^{e1} + f_{r2}^{e2} + f_{r2}^{ne})(f_{r3}^{e1} + f_{r3}^{e2} + f_{r3}^{ne}) + \dots \end{aligned} \quad (2.28)$$

At *global equilibrium* condition $\mathcal{C}_r(f_r^{e0}) = 0$. Therefore the first term in the right hand side of Eq. (2.28) is null. If one consider the higher-order terms $O(\mathcal{M}^2)$ negligible, the equation results simpler:

$$\mathcal{C}_r(f) = \frac{\partial \mathcal{C}_r}{\partial f_{r2}} \Big|_{f_r^{e0}} (f_{r2}^{e1}) + \frac{\partial \mathcal{C}_r}{\partial f_{r2}} \Big|_{f_r^{e0}} (f_{r2}^{ne}) \quad (2.29)$$

At this point it should be noted that Eq. (2.29) must satisfy the *local equilibrium* condition, i.e. when $f_r^{ne} = 0$ the collision operator must be null. Therefore the first term of Eq. (2.29) is null as well. The *quasi linear* Lattice-Boltzmann equation can be thus derived:

$$\mathcal{S}_r f_r = A_{rr2} (f_r - f_r^e) \quad (2.30)$$

where $A_{rr2} = \frac{\partial \mathcal{C}_r}{\partial f_{r2}} \Big|_{f_r^{e0}}$ is called “scattering” matrix. Equation Eq. (2.30) is called *quasi-linear* since it actually solves the non linearity of the Navier-Stokes equations.

The quasi-linear formulation of the Lattice-Boltzmann equation was a significant simplification. Anyway some years later another simplification was introduced with the the Lattice-Bhatnagar-Gross-Krook (LBGK) model, even called *single time relaxation model*.

The basic idea of the LBGK model was to replace the scattering matrix A_{rr2} with a single parameter τ_f , which is the only one required to define the physics of the fluid. The LBGK equation reads as:

$$\mathcal{S}_r f_r = -\frac{1}{\tau_f} (f_r - f_r^e) \quad (2.31)$$

In the quasi-linear formulation the scattering matrix is set in order to satisfy the conservation laws, while, in the LBGK formulation, distribution functions must satisfy them. In particular, the discrete counterpart of Eq. (2.7) must be satisfied:

$$\begin{aligned}\rho &= \sum_r f_r^e = \sum_r f_r \\ \rho u_i &= \sum_r f_r^e c_{ri} = \sum_r f_r c_{ri}\end{aligned}\tag{2.32}$$

From Eq. (2.32) it becomes clear that the Lattice-Boltzmann equation is the discrete counterpart of Boltzmann Equation. Qian *et al.* [18] proposed several solutions in order to satisfy conservation laws and isotropy. As an example, the two-dimensional model D2Q9 depicted in Fig. 3.3 is characterised by the speed of sound $c_s^2 = 1/3$ and the following equilibrium conditions

$$f_r^e = w_r \rho \left[1 + 3(\vec{c}_r \cdot \vec{u}) + \frac{9}{2}(\vec{c}_r \cdot \vec{u})^2 - \frac{3}{2}(u_i^2 + u_j^2) \right]\tag{2.33}$$

where $w_{1,2,3,4} = 4/36$, $w_{5,6,7,8} = 1/36$ and $w_9 = 16/36$.

Finally it should be noted that the choice of the value of τ_f is partially free since it is related to the choice of fluid kinematic viscosity:

$$\nu = c_s^2(\tau_f - 0.5).\tag{2.34}$$

One can tune this parameter and fix the Reynolds number. For stability issues the minimum value is 0.5 since for $\tau_f \rightarrow 0.5 \Rightarrow \nu \rightarrow 0$.

From the numerical point of view one would like to have the maximum value of τ_f since with increasing it, the computational time diminishes. In fact, the higher the value of τ_f , the higher the average time between collisions and the lower the number of iterations necessary to reach equilibrium. Anyway, the higher τ_f , the higher the viscosity, so that one should increase the forcing for reaching the desired Reynolds number, decreasing numerical stability and accuracy. In light of this one should accurately choose τ_f on the basis of the complexity of the problem and of the stability of the model in reaching the solution.

2.2 Multi-Relaxation Method

The lattice Boltzmann equation in the most simple formulation (LBGK) reads as the following equation which is equivalent to the compact form expressed in Eq. (2.31):

$$f_r(\mathbf{x} + \mathbf{c}_r, t + 1) - f_r(\mathbf{x}, t) = -\frac{1}{\tau_f} (f_r(\mathbf{x}, t) - f_r^e(\mathbf{x}, t)), \quad (2.35)$$

where $f_r(\mathbf{x}, t)$, $f_r^e(\mathbf{x}, t)$ are the distribution function and the equilibrium distribution function in the position \mathbf{x} at the time t along the r -th lattice direction, \mathbf{c} is the discrete speed vector and τ_f is the relaxation time to equilibrium. The left hand side of Eq. (2.35) represents the free streaming of the fluid whereas the right hand side represents collisions between particles: the effect of the latter is to bring the distribution function f_r closer to the equilibrium distribution function f_r^e . As already mentioned in the previous section, Eq. (2.35) is the discrete formulation of the Boltzmann Equation. [13]

The Multiple-Relaxation-Time (MRT) scheme allows to overcome some drawbacks of the Bhatnagar-Gross-Krook (BGK) formulation, such as the viscosity-dependent numerical errors, especially in the case of very complex geometries. [19] In order to simulate a pressure gradient $\Delta P/L$ in the flow, an equivalent body force is usually implemented. In presence of a body force, the Lattice-Boltzmann MRT equation reads as follows:

$$\begin{aligned} f_r(\vec{x} + c_r \delta t, t + \delta t) - f_r(\vec{x}, t) = \\ = -\mathcal{M}^{-1} \left\{ \mathcal{S} (m_r(\vec{x}, t) - m_r^{eq}(\vec{x}, t)) - \left(\mathcal{I} - \frac{1}{2} \mathcal{S} \right) (\mathcal{M} F_r) \right\} \end{aligned} \quad (2.36)$$

where $f_r(\vec{x}, t)$ is the distribution function along the r -th lattice direction at the position \vec{x} and time t , c_r is the so-called discrete velocity along the r -th direction, \mathcal{M} is the transformation matrix, \mathcal{S} the collision matrix, \mathcal{I} the identity matrix, and m_r , m_r^{eq} are the moment and the equilibrium moment along the r -th lattice direction, respectively. The set of moments m_r consists of the hydrodynamic moments, which are conserved during collision, e.g. mass and momentum, and the non-conserved moments. For details of the MRT scheme the reader is encouraged to see the paper of Ginzburg *et al.* [19].

In order to recover the correct Navier-Stokes equation and avoid discrete lattice effects, the body force F_r in the MRT model used in the present work has been added during the collision step as follows: [20]

$$F_r = w_r \left(\frac{c_{r,i} - u_i}{c_s^2} + \frac{c_{r,i} u_i}{c_s^4} c_{r,i} \right) \left(\frac{\Delta P}{L} \right)_i, \quad (2.37)$$

where w_r is the weight of the LBM scheme along the r -th lattice direction and $c_{r,i}$, u_i and $(\Delta P/L)_i$ are the eulerian component of the discrete speed, velocity, and pressure gradient,

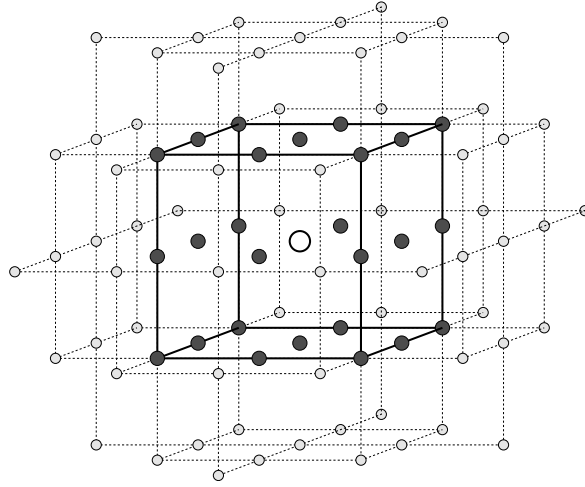


Fig. 2.3 The 92-neighbours fluid sites of the two-belt three dimensional lattice; the dark and grey circles indicate sites belonging to the first and second belt respectively. [23, 24]

along the directions $i = x, y, z$. The macroscopic density ρ and velocity u_i are accurately recovered from the distribution functions f_r :

$$\begin{aligned}\rho &= \sum_r f_r \\ \rho u_i &= \sum_r c_{r,i} f_r + \frac{1}{2} \left(\frac{\Delta P}{L} \right)_i.\end{aligned}\tag{2.38}$$

The MRT model will be used in Chapters 3 and 5 while in Chapter 4 the simplest LBGK scheme will be adopted.

2.3 Two-phase flows

In Lattice Boltzmann models it is possible to implement several cubic Equations Of State (EOS) which represent two-phase gas-liquid flows. In comparison with other numerical methods, the LBM presents the advantage of spontaneously simulate phase separation when liquid-vapour coexistence conditions are reached. The values of the gas and liquid densities at equilibrium satisfy the Maxwell equal-area construction. [21] There are different kind of models to simulate the interaction between the liquid and the vapour phase. The simplest and more used one is the Shan-and-Chen model. [22] In the latter, the liquid-vapour interaction is simulate by a density-dependent pseudo-potential ψ : in other words ψ conveys information about the intermolecular force, i.e. the Van der Waals force.

This model presents a main drawback: the lack of lattice isotropy beyond fourth-order which can generate spurious currents at the interface. Moreover, the classic Shan-and-Chen formulation cannot reach high values of density ratio. In order to overcome this limitation, Falcucci *et al.* [23] and Sbragaglia *et al.* [24] developed the so called “two-belt” or “mid-range” Shan-and-Chen model. The Shan-and-Chen mid-range approach simulates multiphase flows by means of an intermolecular force which acts not only on the first neighbour nodes but even further. The increasing of molecular interactions in the lattice enhance the isotropy and allows to reach higher density ratio. The intermolecular force F is:

$$F_r = -c_s^2 \psi(\mathbf{x}) \sum_l G_l w_l \psi(\mathbf{x} + \mathbf{c}_l) c_{lr} , \quad (2.39)$$

where \mathbf{c}_l is the discrete speed vector which runs over a given set of grid points l , w_l and G_l are the lattice weight and a free parameter, relative to the l -th position, and ψ is the density-dependent pseudo-potential function. The pseudo-potential can have different formulations. In the present work two different formulations have been used. The first one will be used in Chapter 3 along with the MRT scheme, in order to allow a higher density ratio:

$$\psi = \sqrt{\rho_0} \left[1 - \exp\left(-\frac{\rho_0}{\rho}\right) \right] . \quad (2.40)$$

On the other side, in Chapter 4, the pseudo-potential will be chosen in order to correctly simulate phase change along with the LB heat equation (see next section for further details):

$$\psi = \exp\left(-\frac{1}{\rho}\right) . \quad (2.41)$$

The Shan-and-Chen model yields to a two-phase EOS once the free parameters ρ_0 and G_l are properly chosen. Taking into account the 92-neighbours scheme used in Chapter 3 (2-belt and three-dimensional lattice), the macroscopic pressure equation is determined as follows:

$$P = c_s^2 \rho + \frac{1}{2} (G_1 + G_2) c_s^2 \psi^2 , \quad (2.42)$$

where P is the pressure, ρ is the density and G_1 , G_2 are the free parameter G_l relative to the first and second belt of lattice fluid sites respectively (details are given in the paper by Falcucci *et al.* [23]). The 92-neighbours model is depicted in Fig. (2.3).

2.4 Two-phase thermally-coupled flows ⁶

One of the main benefits of the lattice Boltzmann method is the possibility to implement an Heat Equation along with the fluid flow simulation. In practice, this is done by solving another lattice for the scalar quantity T , temperature. In the temperature lattice one solves the Heat Equation in the same way as in the fluid flow lattice one solves the Navier-Stokes Equation. In Chapter 4 this approach, which is often called “passive-scalar” approach, will be exploited in order to simulate liquid-vapour phase-change inside a fuel cell Gas Diffusion Layer. In particular, the resulting Heat Equation is:

$$\frac{\delta T}{\delta t} + \mathbf{u} \cdot \nabla T = \nabla \cdot (\alpha \nabla T) + \Psi, \quad (2.43)$$

where T is the temperature, \mathbf{u} the velocity vector, α is the thermal diffusivity, and Ψ is the source term. [25] By using this method and by choosing the correct form of the pseudo-potential ψ , one can simulate phase change in a thermodynamically consistent way, with a proper description of the latent heat. [26, 27] In Chapter 4 Eq. 2.41 will be adopted; the resulting equation of state is:

$$P = c_s^2 T + \frac{1}{2} (G_1) c_s^2 \psi^2. \quad (2.44)$$

Details of the two-phase and thermal model are given in the paper by Biferale *et al.* [26]

2.5 Interpolation bounce-back algorithm

The Lattice-Boltzmann Method works on a lattice, so that curved boundaries must be approximated with stair-shaped boundaries. From one side, this facilitate the parallelisation of the code and reduce the computational effort. From the other side, this stair-shaped approximation reduce the accuracy of the solution at the boundaries. Bouzidi *et al.* [28] introduced an interpolation algorithm for the velocities at the boundaries, which allows to get rid of the stair-shaped approximation, without increasing the resolution. Once the distance δ_w between the fluid node and the wall is known, the following correction for the value of the distribution function can be applied:

⁶The Lattice-Boltzmann thermally-coupled code with interpolated bounce-back algorithm is an improvement of the code developed by Prof. Federico Toschi of the Applied Physics Department of Eindhoven University of Technology.

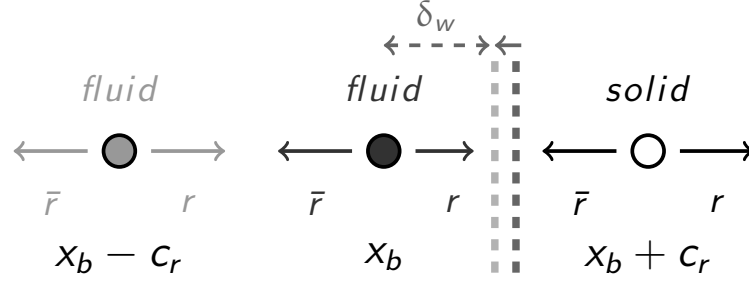


Fig. 2.4 One-dimensional example of interpolation algorithm.

$$\begin{aligned} \tilde{f}_{\bar{r}}(\mathbf{x}_b + \mathbf{c}_r, t) &= k_1 \cdot \tilde{f}_r(\mathbf{x}_b, t) + k_0 \cdot \tilde{f}_r(\mathbf{x}_b - \mathbf{c}_r, t) + \bar{k}_{-1} \cdot \tilde{f}_{\bar{r}}(\mathbf{x}_b, t) \\ k_1 &= 2\delta_w; k_0 = 1 - 2\delta_w; \bar{k}_{-1} = 0; (\delta_w < 0.5) \\ k_1 &= 1/(2\delta_w); k_0 = 0; \bar{k}_{-1} = 1 - 1/(2\delta_w); (\delta_w > 0.5) \end{aligned} \quad (2.45)$$

where \tilde{f}_q is the post-collision distribution function relative to the r -th direction, \mathbf{x}_b is the fluid position next to the boundary, \hat{r} represents the opposite direction of r and k_1 , k_0 , \bar{k}_{-1} are the parameter related to the wall distance δ_w . Figure 2.4 depicts the interpolation scheme. The interpolation algorithm conserves momentum up to second order but it does not conserve mass. This leakage or gain of mass can be easily predicted by Eq. (2.45), taking into account that the mass exchange at the boundary between the fluid and the solid node is $\rho_{lack} = \tilde{f}_{\bar{r}}(\mathbf{x}_b + \mathbf{c}_r, t) - \tilde{f}_r(\mathbf{x}_b, t)$. In fact, while with a normal bounce-back, i.e. for $\delta_w = 0.5$, the aforementioned difference is equal to zero, it is not when $\delta_w \neq 0.5$. Actually, the fluid node is not more an unitary lattice cube when $\delta_w \neq 0.5$ and its mass lack or excess must be taken into consideration. To do that, in the present work, a further correction at the boundary is herein proposed and implemented: after the streaming step the mass difference ρ_{lack} is added to the distribution functions of the fluid node \mathbf{x}_b in a symmetric way as follows:

$$f_r(\mathbf{x}_b, t) = \tilde{f}_r(\mathbf{x}_b, t) + w_r \rho_{lack} . \quad (2.46)$$

This correction ensures the conservation of mass without changing the velocity field at the boundary which remains the one described by the interpolation algorithm. The velocity at the boundary is given by Eq. (2.38), which in the one-dimensional case results:

$$u_r(\mathbf{x}_b, t) = [f_r(\mathbf{x}_b, t) + w_r \rho_{lack}] c_r - [f_{\hat{r}}(\mathbf{x}_b, t) + w_{\hat{r}} \rho_{lack}] c_{\hat{r}} . \quad (2.47)$$

Since $c_r = -c_{\hat{r}}$, the velocity $u_r(\mathbf{x}_b, t)$ is not affected by the mass correction.

2.6 Model validation

The Lattice-Boltzmann model used in the present thesis has been validated in several ways. Since the model involves different physical variables and conditions, e.g. liquid and gas densities with no-slip boundary condition or temperature with fixed temperature at the wall, different validations have been performed.

Single-phase validation

Firstly, the single-phase flow field through a channel in contact with a porous medium has been compared with the theoretical solution of the Volume-Averaged Navier-Stokes (VANS) equations, see Fig 2.5. The VANS equations are determined by spatially averaging over a representative thin volume the Navier-Stokes equations. The volume where the spatial averaging is applied must be long enough along the main directions of the flow in order to catch the largest length scale of the flow. In turn it must be thin enough along the other direction (typically the wall-normal direction) to ensure enough accuracy of the solution. [29]

Let be the Cartesian coordinates x, y, z and the velocities u, v, w . The generic spatially averaged variable φ can be determined as:

$$\begin{aligned} \varphi &= \langle \varphi \rangle + \varphi' \\ \langle \varphi \rangle(z) &= \frac{1}{\varepsilon(z)V_0} \int \int_{V_f} \varphi(x, y, z) dx dy \end{aligned} \quad (2.48)$$

where V_0 is the averaging volume, $V_f = \varepsilon V_0$ is the fluid averaging volume, ε the porosity, $\langle \cdot \rangle$ the spatial averaging operator, x, y the main directions of the flow and z the wall-normal direction. In the case of laminar, steady, uniform and two-dimensional flow the VANS equation obtained by applying the averaging procedure reads as:

$$0 = g_x - \frac{1}{\varepsilon} \frac{\partial \varepsilon \langle u'w' \rangle}{\partial z} + \frac{1}{\varepsilon} \frac{\partial}{\partial z} \varepsilon \left\langle v \frac{\partial u}{\partial z} \right\rangle + \frac{1}{\rho V_f} \int_S p n_x dS - \frac{1}{\rho V_f} \int_S v \left[\frac{\partial u}{\partial x} n_x + \frac{\partial u}{\partial z} n_z \right] dS \quad (2.49)$$

where g_x is the generic body force acting along x , S is the boundary surface between fluid and solid phase inside the averaging volume V_0 and n_x, n_z the Cartesian components of the

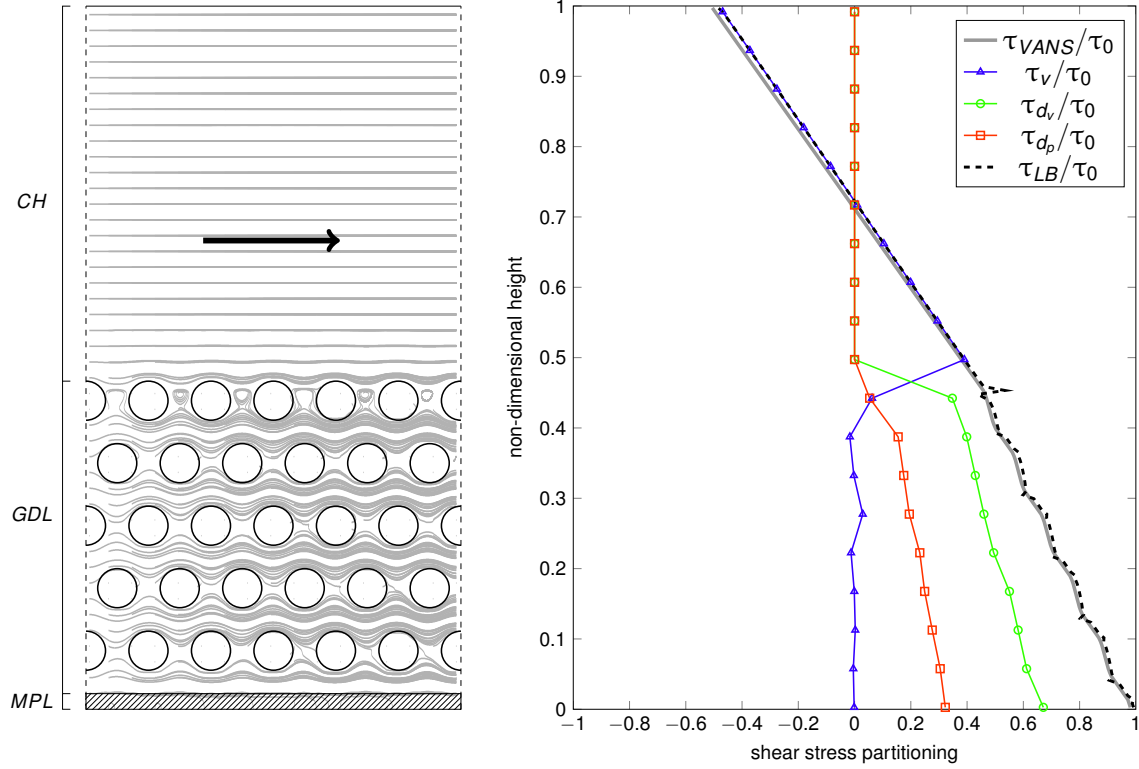


Fig. 2.5 Flow field (left panel) and shear stress partitioning (right panel). At the bottom the total wall shear stress calculated from the LB flow field is correctly balancing the stresses computed in the medium, as predicted by the VANS equation.

versor normal to S . By integrating along z Eq. (2.49) one obtains the shear stress partitioning:

$$\begin{aligned}
 \frac{\tau(z)}{\rho} &= \int_z^{z_0} \varepsilon g_x dz = \\
 &= \underbrace{\varepsilon \langle \tilde{u}\tilde{w} \rangle \Big|_z^{z_0}}_{\tau_{fi}/\rho} - \underbrace{\varepsilon \left\langle \mathbf{v} \frac{\partial u}{\partial z} \right\rangle \Big|_z^{z_0}}_{\tau_v/\rho} - \underbrace{\int_z^{z_0} \frac{1}{\rho V_0} \int_S p n_x dS}_{\tau_{d_p}/\rho} + \underbrace{\int_z^{z_0} \frac{1}{\rho V_0} \int_S \mathbf{v} \left[\frac{\partial u}{\partial x} n_x + \frac{\partial u}{\partial z} n_z \right] dS}_{\tau_{d_v}/\rho} \quad (2.50)
 \end{aligned}$$

where z_0 is the position corresponding to $du/dz = 0$. It should be noted that for laminar flows the total shear stress at the wall τ balances the sum of the viscous stress τ_v , the form-induced stress τ_{fi} , the pressure drag τ_{d_p} and the skin friction τ_{d_v} acting on the porous medium.

Figure 2.5 depicted the shear partitioning determined from the LB flow field. The stresses have been calculated by using Eq. (2.50) and a finite difference scheme in order to obtain $\tau_{LB} = \tau_v + \tau_{fi} + \tau_{d_p} + \tau_{d_v}$ and compared it with the theoretical solution $\tau_{VANS} = \rho \int_z^{z_0} \varepsilon g_x dz$. The computed value of the total shear stress is perfectly overlapping the theoretical solution.

The geometry is representative of the typical design of fuel cells and flow batteries where a channel distributes the gas over a porous medium and the Reynolds number is low. It is interesting to notice that the skin friction is much higher than pressure drag in the porous medium so that the main force which opposes the flow is the tangential friction at fluid-solid boundary. Moreover the abrupt change in the shear stress partitioning between the channel and the porous medium give rise to laminar separation zones at the interface and highlight the significant role the GC-GDL interface is playing.

It should be finally noted that the flow develops vorticity at the interface which are repeated over a length $\ell_{interface}$ which is approximately three times the distance between spheres. This length is considered to be the dominant length scale at the interface.

Permeability validation

In order to further validate the single-phase LB model, the permeability values of flow through a tube bundle have been compared with the theoretical solution given by Gebart *et al.* [30] with varying the fiber diameter d_f and porosity ε . Permeabilities have been determined by means of the Darcy law:

$$K = \varepsilon U \mu \left(\frac{\Delta P}{L} \right)^{-1}, \quad (2.51)$$

while the Gebart solution is:

$$K = d_f^2 C \left(\sqrt{\frac{1 - \varepsilon_c}{1 - \varepsilon}} - 1 \right)^{5/2}, \quad (2.52)$$

with $C = 4/(9\sqrt{2}\pi)$ and $\varepsilon_c = 1 - \pi/4$. Figure 2.6 shows the comparison: the values of the permeability with $d_f = 4$ and the bounce back algorithm are satisfactorily close to the theoretical solution. In turn, with a normal bounce-back rule at the boundary one should increase the number of lattice nodes to represent the fibers. This result should be hailed as a proof of the goodness of the interpolation algorithm.

Vapour quality test

When using the Shan-and-Chen model, once the interaction force G is chosen, the equilibrium liquid-vapour densities ρ_{liq} and ρ_{gas} are defined. Anyway, in both phases densities fluctuate around these values and separation phenomena happen spontaneously. The interface is not “tracked” and there is no information apart from the density field. Consequently, one needs to fix two *density thresholds* ρ_{thre} which define where the fluid is gas or liquid. A good way to

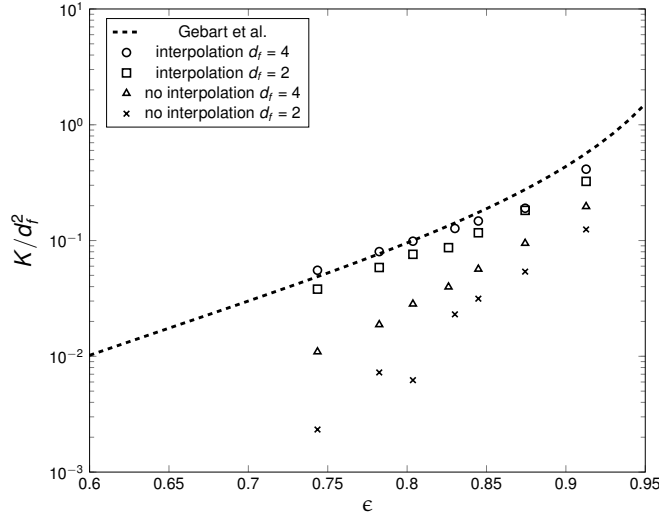


Fig. 2.6 Non-dimensional permeability K/d_f^2 against porosity ϵ compared with the theoretical solution of Gebart et al. [30]

determine the thresholds is to ensure that the ratio between the mean value of liquid density $\langle \rho_{liq} \rangle$ and gas density $\langle \rho_{gas} \rangle$ which are calculated on the basis of the threshold, equals the ratio between the equilibrium densities, that is:

$$\langle \rho_{liq} \rangle / \langle \rho_{gas} \rangle = \rho_{liq} / \rho_{gas} . \quad (2.53)$$

In order to calibrate such parameters, a vapour quality test in a tube bundle has been carried out. Figure 2.7 depicts the gas-phase volume void fraction $\epsilon = n_{gas} / (n_{gas} + n_{liq})$ plotted against the value of the vapour quality Q , with varying the thresholds ρ_{thre} ; n_{gas} and n_{liq} are the number of nodes belonging to the gas and liquid phase, respectively, determined on the basis of ρ_{thre} . If Eq. (2.53) is satisfied, the following equation holds:

$$\epsilon_{gas} = \left[1 + \frac{\rho_{gas}}{\rho_{liq}} \left(\frac{1}{Q} - 1 \right) \right]^{-1} \quad (2.54)$$

with the vapour quality Q define as follows:

$$Q = \frac{n_{gas} \langle \rho_{gas} \rangle}{n_{gas} \langle \rho_{gas} \rangle + n_{liq} \langle \rho_{liq} \rangle} . \quad (2.55)$$

From Figure 2.7 the effect of varying the threshold can be seen. This approach has been used in the present work before simulations in order to tune the density values and increase the confidence of data.

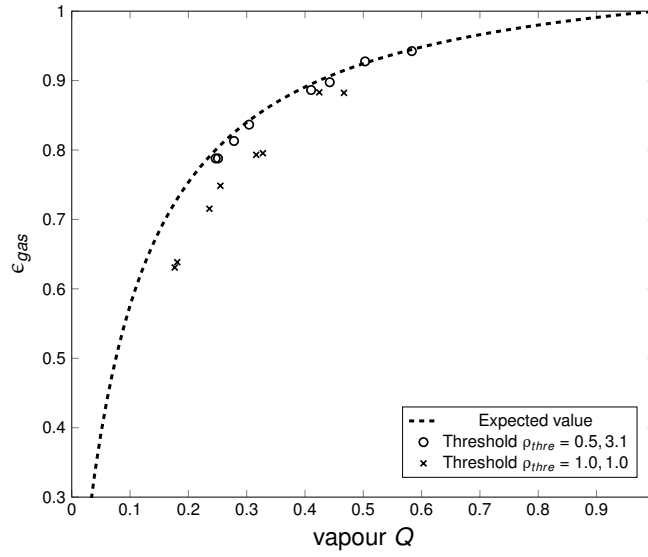


Fig. 2.7 Gas volume void fraction ϵ_{gas} plotted with the vapour quality Q .

Film condensation and latent heat validation

Finally, the coupling between two-phase flow and temperature fields has been evaluated by simulating film condensation on a subcooled surface inside a two-dimensional pipe. The comparison have been done both with the famous Nusselt theory [31] and with the Asano theoretical solution which take into account the shear stress between the liquid film and the surrounding gaseous phase. [32] The subcooled wall temperature T_{cool} and the initial density of the system have been set in order to match the thermodynamic condition of liquid-vapour coexistence, in contrast with the higher initial temperature of the fluid $T_0 > T_{cool}$. Following the Asano approach, the film thickness growth $\delta_{film}(x)$ along the streamwise direction x can be described by the following quartic function:

$$\delta_{film}^4 \frac{\Delta P}{4L\nu_{liq}} + \delta_{film}^3 \frac{\tau_s}{3\nu_{liq}} = \frac{1}{\lambda_h} \kappa (T_s - T_{cool})(x - x_0) \quad (2.56)$$

where $\Delta P/L$ is the body force, ν_{liq} is the liquid kinematic viscosity, λ_h is the latent heat, $\kappa = 5/3 \rho_{liq} \alpha$ is the liquid thermal conductivity, $T_s(x)$ is the temperature at the liquid-gas interface, x_0 is the position where the film starts to grow and $\tau_s(x)$ is shear stress at the interface. By assuming that the pipe width is much larger than the film thickness, i.e. $H \gg \delta_{film}$, the shear stress τ_s can be determined on the basis of the local gas Reynolds number: [32]

$$\tau_s = 0.332 \frac{Re_{x,gas}^{3/2} \nu_{gas} \mu_{gas}}{x^2}. \quad (2.57)$$

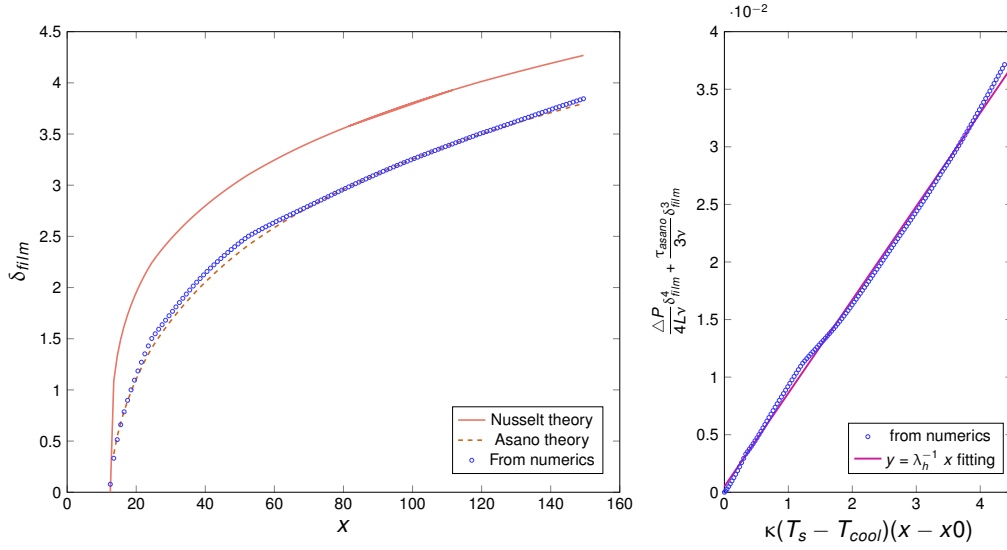


Fig. 2.8 Left panel: condensed film thickness δ_{film} plotted with distance x . The numerical solution is well overlapping the theoretical solution of Asano et al. [32] Right panel: the slope of the curve represents the latent heat λ_h which is approximately constant along the film thickness.

where the local gas Reynolds number $Re_{x,gas}$ is define with the free stream gas velocity $U_{\infty,gas} = (\Delta P/L) H^2/(12\mu_{gas})$ as follows:

$$Re_{x,gas} = \frac{U_{\infty,gas} x}{\nu_{gas}}. \quad (2.58)$$

Left panel of Fig. 2.8 shows the film thickness growth along x . The numerical solution is well described by the Asano theory, while the discrepancy with the Nusselt theory highlights the not negligible effect of the shear exerted by the gaseous phase on the film thickness. The latent heat λ_h has been determined from by fitting Eq. 2.56 with the numerical values of δ_{film} , T_s and τ_s : the slope of the curve in right panel of Fig. 2.8 represents the value of the latent heat and it is almost always constant along x . This result confirms that the description of latent heat is thermodynamically consistent in the present model.

Chapter 3

Fluid Dynamics in Fuel Cells ¹

3.1 Characteristic length scales in fuel cells

In fuel cells several physical phenomena take place, from current transport to molecular diffusion, from phase-change to thermal conductance, each of them dependent on the others. Thus, the general picture from the outside is representative of dozen of other processes happening inside the cell. Even if one focused only on the fluid-dynamic aspects, he would observe a chain of phenomena which contribute to the macroscopic mass and momentum transport. Each link in the chain has his own characteristic length scale.

For instance, taking into account hydrogen transport from fuel cell inlet to the place where the last reaction occurs, one observes the following type of mass and momentum transport: a convective transport inside the distribution gas channels (GC), with typical length scale $\ell_{GC} = O(mm)$, a diffusive transport inside the gas diffusion layer (GDL), with mean pore size $\ell_{GDL} = O(\mu m)$, a diffusive transport in the micro-porous-layer (MPL) all the way to the catalyst layer (CL), where the mean pore size is $\ell_{MPL} = O(nm \div \mu m)$, and a proton transport inside the proton exchange membrane (PEM), with a typical length scale $\ell_{PEM} = O(nm)$. Figure 3.1 schematises the transport mechanisms.

In the present Chapter the two-phase mechanism of gas-liquid transport in the GC, in the GDL and in the GC-GDL interface will be discussed. In particular, the influence of cell design on liquid water cumulation will be investigated, in order to better explain the importance of water management in fuel cells and the effects of length scale separation on cell performances. Simulations presented in this chapter aim to investigate the case when water erupts from the catalyst layer in vapour form.

¹A version of this chapter has been published in *Journal of Fuel Cell Science and Technology*: D. Maggiolo, A. Marion and M. Guarnieri, *Lattice Boltzmann modeling of water cumulation at the gas channel-gas diffusion layer interface in polymer electrolyte membrane fuel cells*, Vol.11(6), 061008, DOI:10.1115/1.4028952.

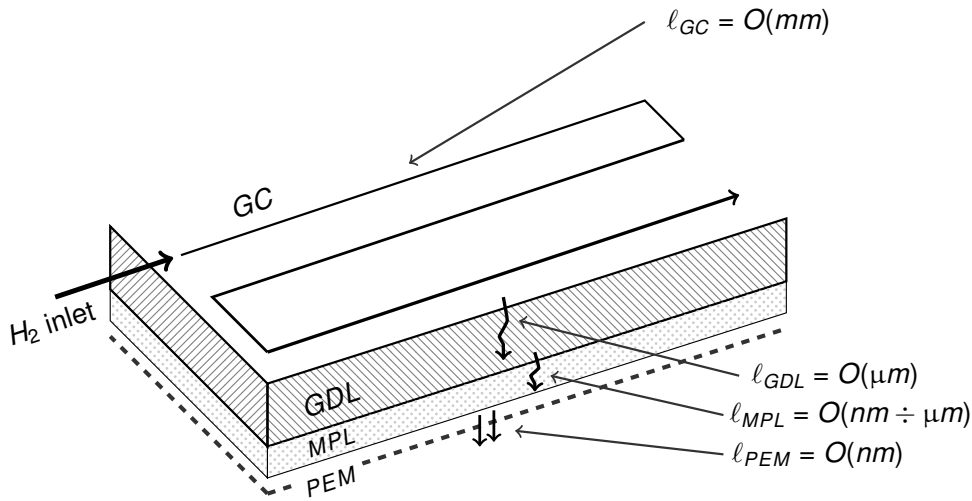


Fig. 3.1 Characteristic length scales in fuel cells.

3.2 Water management and liquid water cumulation in fuel cells

3.2.1 Introduction

In Polymer Electrolyte Membrane Fuel Cells (PEMFCs) water management is a key factor to ensure best performances. In fact, flooding in the Gas Diffusion Layer (GDL) clogs the voids in the porous medium, so limiting reactant diffusion. Moreover, water in liquid phase can reach and obstruct the Gas Channel (GC) increasing pressure drops along the channels.

Water in liquid phase is produced at the cathode due to the electro-chemical reactions and can be present at the anode due to vapour condensation. [33, 34] Several attempts have been made in order to measure water content in PEMFCs. The majority of them concern the cathode side and only few studies have considered flooding at the anode. Ge and Wang [35] observed droplets formation in the anode gas channel via optical photography and compared results from different experiments. They measured high relative humidity (RH) and supersaturation at the anode outlet at a cell temperature of $T = 50^\circ\text{C}$ at any conditions and they found that water tends to condense on the channel walls rather than inside the GDL. Siegel *et al.* [36] measured the mass of liquid water at the anode through neutron imaging. They observed a significant voltage decrease caused by channel water clogging, confirming the importance of efficient anode water management. Hartnig *et al.* [37] found that at high current densities liquid water accumulated at both anode and cathode, near the channel ribs and near the microporous layer. Yamauchi *et al.* [34] investigated

the flooding/plugging phenomena on the anode side of a PEMFC by means of a two-pole (anode/cathode) simultaneous image measurement. The cumulation of water in liquid phase at the anode in low humidity condition has been described as a consequence of the steam back-diffusion mechanism from the cathode side.

There are three main factors that influence water vapour concentration at the anode: the RH value of the inlet gas and the water back diffusion from the cathode to the anode, partially balanced by electro-osmotic drag from the anode to the cathode. These factors can cause condensation. However it is not yet clear whether the design of the GC and GDL could be optimised to limit water cumulation and pores clogging. Li *et al.* [38] proposed a model to determine the design of the GC suitable to facilitate the evaporation of liquid water. Thuran *et al.* [39] evaluated the influence of the land-channel ratio. They found that the liquid stored in the cell decreases, as the land-channel ratio decreases. Recently Sruoji *et al.* [40] proposed a new flow field architecture, named Open Metallic Element (OME). Its concept is elimination of lands, that is achieved substituting a porous medium to the conventional channel-land design. Cell's performance dramatically improved. The authors ascribe such result to the absence of lands, that facilitates water removal.

The active areas in PEMFCs are typically two planar region separated by a thin electrolyte and supported by highly permeable GDLs which spread the fuel over the whole catalyst areas and facilitate the removal of reaction product. In turn the fluids are taken to the GDLs by means of plates put in contact with them and provided of a dense serpentine of thin GCs. Many factors affect the interaction between GCs and GDLs, that is, the fluid behaviour at the GC-GDL interfaces. From a hydrodynamic point of view, the GC-GDL interface corresponds to the so called Transition Layer (TL) which is the portion of the flow in the porous medium (i.e. the GDL) influenced by the flow in the channel (i.e. the GC). The hydrodynamic mechanism of mass transfer in the TL has been widely studied [41–44] but, to the best of the authors' knowledge, there are no studies about water cumulation phenomena in the TL.

In the light of these evidences, the present study proposes a three-dimensional two-phase model of the flow in the GC and GDL based on the Lattice Boltzmann method (LBM). It is a further development of Maggiolo *et al.* [45] The aim is to investigate the effect of the GC-GDL geometry on water cumulation at the anode and, in particular, at the GC-GDL interface.

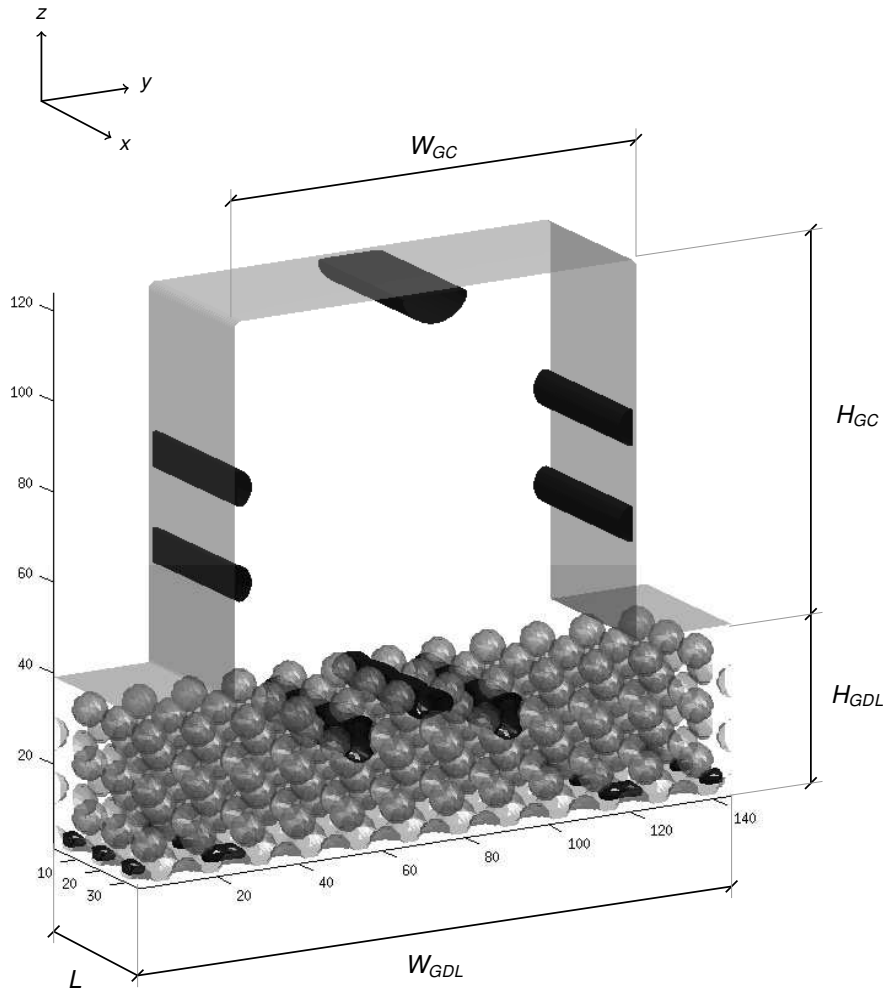


Fig. 3.2 Sketch of the simulation domain $h = 0.3$, $d_p = 33 \mu\text{m}$, $d_s = 67 \mu\text{m}$, $\phi = 0.69$ and density fields at the equilibrium. The darker zones indicate liquid density.

3.2.2 Simulations of water cumulation

Simulation set-up

In order to simulate the gas-liquid phase separation and the water cumulation, a simplified GC-GDL element is herein considered, as represented in Figs. 3.2 and 3.3. The total height of the domain is $H = 1 \text{ mm}$, and the length is $L = 0.3 \text{ mm}$, which is statistically consistent with the heterogeneity of the porous medium (the dominant length scale at the interface approximately equals three times the distance between spheres, see Chapter 2 Section 2.6). The GC and GDL widths are $W_{GC} = 0.8$ and $W_{GDL} = 1.2 \text{ mm}$ respectively, to take into account the true land-gap structure of the GC. The GDL height H_{GDL} is varied so that the

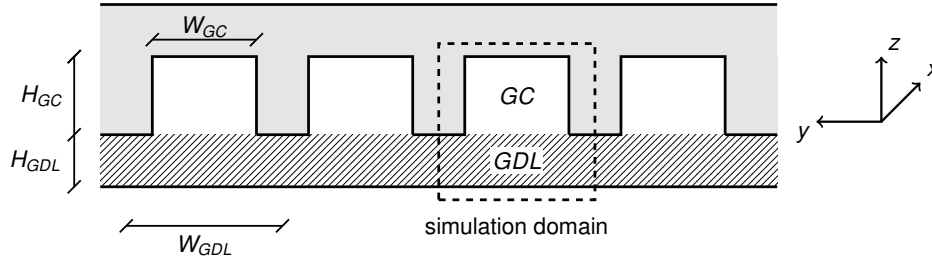


Fig. 3.3 Scheme of GC and GDL cross section of a PEMFC. The dashed lines indicate the simulation domain cross-sectional area.

relative GDL height h (i.e. the ratio of the GDL height to the total height H) is varied within the range $h = 0.3 - 0.9$.

For the sake of simplicity, in the present chapter, the geometry of the GDL is represented by a Body Centered Cubic (BCC) packing of spheres as depicted in Fig. 3.2; the diameter of the spheres, the minimum pore size and the porosity will be addressed as d_s , d_p and ϕ respectively.

The flow is assumed to be steady, uniform and driven by a pressure gradient $\Delta P/L$ which is implemented as an equivalent body force. [13] Periodic boundary conditions are imposed at the inlet and the outlet along the stream-wise direction x and at open boundaries along the span-wise direction y ; no-slip boundary conditions on fluid-solid boundaries are given via a bouncing-back mechanism. A wall fictitious density is set at the solid boundaries so as to simulate a gas-liquid-solid contact angle of about 90° . [46]

The typical value of the Reynolds number in the gas channel (i.e. Re_{GC}^*) can be calculated with typical values of geometric and fluid properties in PEMFCs:

$$Re_{GC}^* = \frac{Q_{cell} d_h}{N ab v_{H_2}} \sim 14, \quad (3.1)$$

where $Q_{cell} = 1.4$ l/min/cell is the imposed inlet flow rate per cell, that is the maximum advised inlet flow rate of UBzM PEMFC stacks (to which correspond an 80% gas utilisation). $N = 23$ is the number of gas channels per cell in the anode, $a = 0.8$ mm and $b = 0.7$ mm are the cross-sectional width and height of the gas channels, $d_h = 2ab/(a+b)$ is the gas channel hydraulic diameter and $v_{H_2} = 1 \cdot 10^{-4}$ m²/s is the kinematic viscosity of the hydrogen.

In general, the pressure gradient can be related to the Reynolds number in the gas channel by means of the Hagen-Poiseuille law:

$$\frac{\Delta P}{L} = \frac{12}{H_{GC}^3} v \mu Re_{GC}, \quad (3.2)$$

Table 3.1 Parameters used in the four sets of simulations> in each set the relative height has been varied within the range $h = 0.3 - 0.9$.

Set	d_p	d_s	ϕ	Fixed physical quantity
1st	33 μm	67 μm	0.69	$\Delta P/L = (\Delta P/L)^*$
2nd	50 μm	50 μm	0.84	$\Delta P/L = (\Delta P/L)^*$
3rd	33 μm	67 μm	0.69	$Re_{GC} = Re_{GC}^*$
4th	50 μm	50 μm	0.84	$Re_{GC} = Re_{GC}^*$

where μ e ν are the dynamic and kinematic viscosities of the fluid. Eq. (3.2) can be applied to any kind of fluid, such as pure hydrogen or water-hydrogen ($\text{H}_2\text{-H}_2\text{O}$) mixture, so that $\mu = \mu_{mix}$ and $\nu = \nu_{mix}$ are used herein in order to simulate the $\text{H}_2\text{-H}_2\text{O}$ mixture flow. For sake of clarity, the value of the pressure gradient for $Re_{GC} = Re_{GC}^*$ and $H_{GC} = 0.7$ mm will be addressed as $(\Delta P/L)^*$.

Four sets of simulations have been run varying the relative GDL height h : in the first and second one the pressure gradient is fixed at $\Delta P/L = (\Delta P/L)^*$ whereas in the third and fourth one the Reynolds number in the GC is fixed at $Re_{GC} = Re_{GC}^*$ by adjusting the corresponding pressure gradient evaluated by Eq. (3.2). All the main properties of the four sets of simulations are listed in Tab. (6.1).

Equation of state

Three main hypotheses have been assumed: (i) the two-mixture components in the gas phase (H_2 and H_2O) occupy the same volume, (ii) the intermolecular force between the two gas mixture components is negligible compared to the force between components in different phases and (iii) the phase-separation is isothermal.

Based on the aforesaid hypotheses, starting from a metastable condition, it's possible to simulate the spontaneous phase separation which leads to the phase equilibrium described by a mixture EOS, by means of the present model. The phase separation occurs when the attractive forces are strong enough and the temperature (i.e. $G_1 + G_2$) is low enough. The model is isothermal, hence the temperature and the pressure are set to be homogeneous and critical over the all domain. With these conditions, the phase separation can take place and it is possible to investigate where, under critical conditions, the gas and the liquid phases preferably exist. It should be noted that all simulations starts in a metastable condition and no water is added to the domain during simulations. Hence the model does not simulate

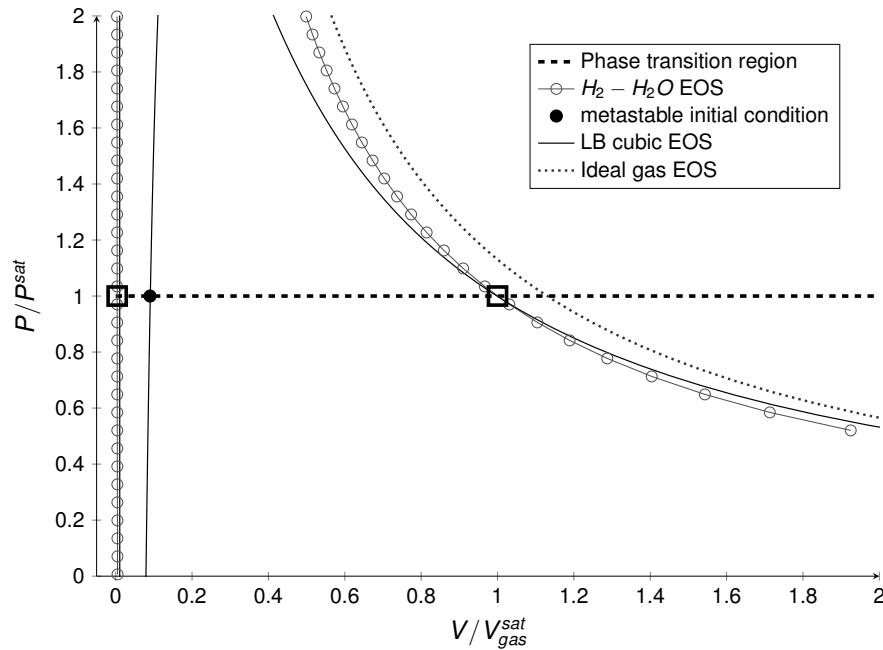


Fig. 3.4 Comparison between the Lattice-Boltzmann EOS and the Rimbach and Chatterjee EOS. [47] The square-shaped markers indicate the gas (i.e. $\rho_{gas} \sim 0.028$) and liquid (i.e. $\rho_{liq} \sim 2.5$) equilibrium phases at P_{sat} .

condensation phenomena but rather the behaviour of two-phase flow in equilibrium in saturation condition.

The EOS is calibrated in order to reproduce the EOS of the H_2 - H_2O -mixture proposed by Rimbach and Chatterjee with the following imposed conditions: [47]

- temperature $T = 70^\circ\text{C}$;
- mole water fraction $X_{H_2O} = 0.2$;
- relative humidity $RH = 100\%$.

to which correspond the critical pressure $P = P_{sat}$. The latter values are arbitrarily chosen in order to simulate a possible saturation condition of the cell.

Figure 3.4 shows the good correspondence between the lattice Boltzmann EOS given by Eq. (2.42) and the H_2 - H_2O -mixture EOS of Rimbach *et al.* [47] The resulting liquid-gas dynamic viscosity and density ratios are of the order of 100. It has been mathematically demonstrated that the two-phase capillary filling is driven by the dynamic viscosity ratio when inertial forces are negligible. [48] Therefore, although the LBM density ratio results two order of magnitude lower than the real one, the model can qualitatively simulate phase-separation and two-phase flow phenomena given that the dynamic viscosity ratio is comparable with the

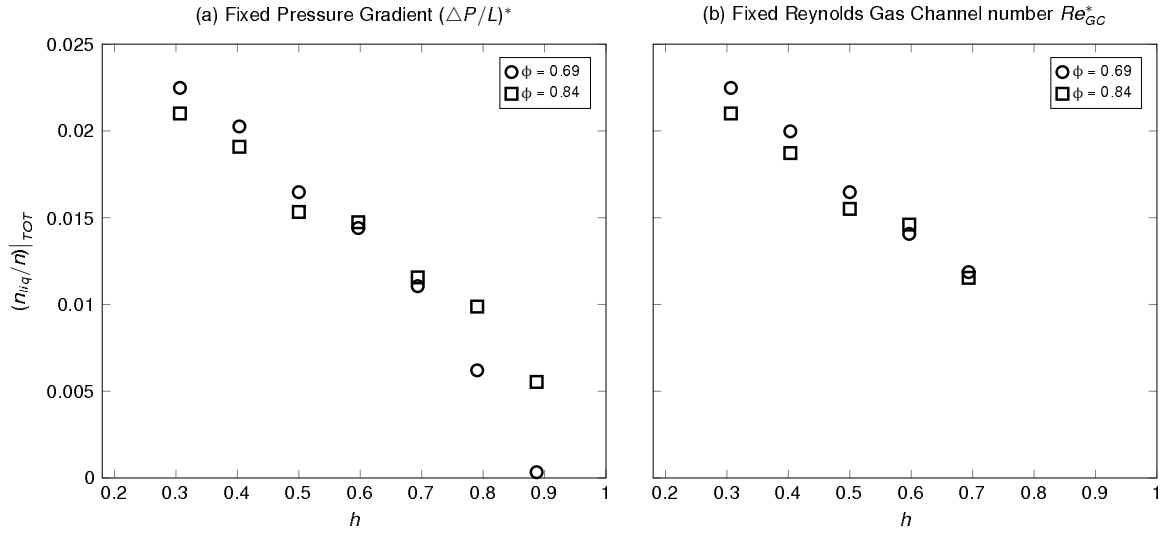


Fig. 3.5 Number of liquid sites over total fluid sites versus the relative GDL height $h = H_{GDL}/H$: (a) for a fixed pressure gradient and (b) for a fixed Reynolds number in the GC.

real one and the Reynolds number is small.

Results

All simulations start with the fluid in a metastable state as depicted in Fig. 3.4. The equilibrium state is considered to be reached when two convergence criteria are simultaneously satisfied at the t -th iteration: (i) the relative error between the Reynolds number at the t -th iteration and the previous iteration value (i.e. $|Re^t - Re^{t-1}|/Re^t$) is less than 10^{-4} , and (ii) the relative error between the mean density value of sites that overcome the initial density value at the t -th iteration and the previous iteration value (i.e. $|\bar{\rho}_{>meta}^t - \bar{\rho}_{>meta}^{t-1}|/\bar{\rho}_{>meta}^t$) is less than 10^{-4} . Re is given by:

$$Re = \frac{UH}{\nu}, \quad (3.3)$$

where U is the average velocity of the two-phase flow along the stream-wise direction x and ν is the kinematic viscosity. A lattice site is considered to belong to the liquid or gas phase when the density value exceeds or falls short of the threshold value $\rho_{lim} = 2.15$, respectively.

Figure 3.5 shows the ratio of the number of liquid-phase fluid sites n_{liq} on the total number of fluid sites n , at different values of relative GDL height h . First of all, for almost all the data-set, as the relative GDL height h increases, the liquid-phase fluid sites decreases with respect to the total number of fluid sites. Secondly, the values of n_{liq}/n obtained in the

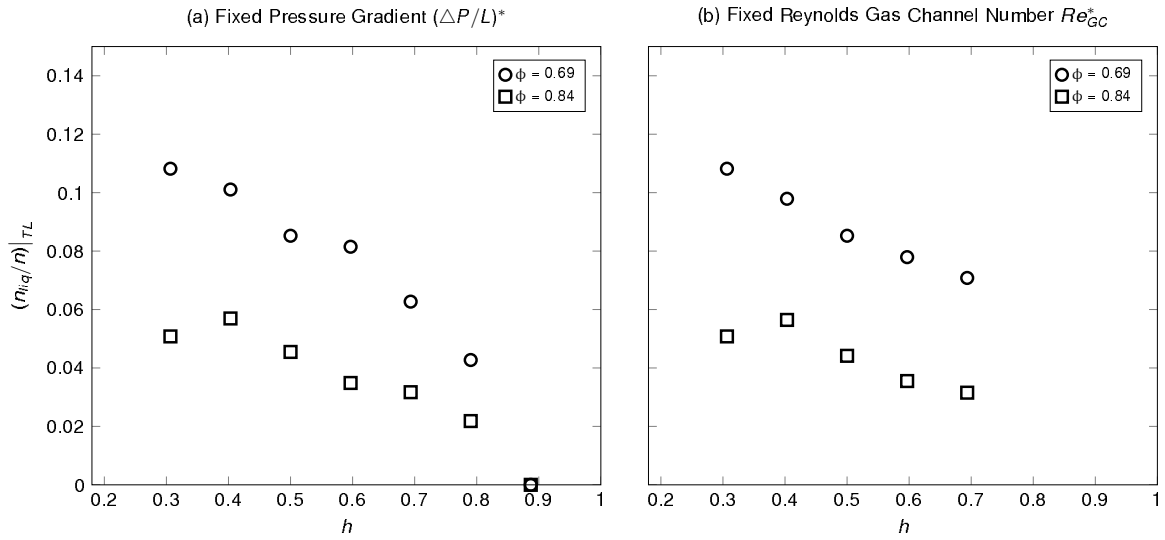


Fig. 3.6 Number of liquid sites over total fluid sites in the Transition Layer (TL) versus the relative GDL height $h = H_{GDL}/H$: (a) for a fixed pressure gradient and (b) for a fixed Reynolds number in the GC.

first and second sets of simulations (i.e. with a fixed pressure gradient) remain more or less the same in the third and fourth ones (i.e. with a fixed Re_{GC}), indicating that the value of n_{liq}/n neither depends on the gas channel Reynolds number within the range $Re_{GC} \sim 0 - 14$ nor on the porosity of the GDL. It's intuitive to think that the strong effect of the relative GDL height on water cumulation phenomena is related to the mechanism of mass transfer in the GC, in the GDL and, especially, in the GC-GDL interface. [45]

As remarked in the second section of this chapter, in order to study the mechanism of mass transfer at the GC-GDL interface is crucial to identify the TL, that is the portion of flow in the porous medium affected by the flow in the channel. In the present work the TL is defined as the region under the GC-GDL boundary long as the domain length L , wide as the GC width and high as two times the sum of d_p and d_s . Figure 3.6 shows the ratio of the number of liquid-phase fluid sites n_{liq} on the total number of fluid sites n in the TL at different values of relative GDL height h , whereas Fig. 3.7 depicts the cross-sectional area of the TL and the location of liquid-phase sites for three different values of h .

The number of liquid-phase sites at the GC-GDL interface decreases as the relative GDL height increases, in a similar manner to the total number of liquid sites shown in Fig. 3.5, confirming the influence of the fluid behaviour in the TL on the number of liquid-phase sites in the whole domain. Moreover, Fig. 3.6 shows that water cumulation depends somehow on the porosity ϕ and on the minimum pore size d_p . However the relationship between n_{liq}/n and ϕ , d_p is not straightforward.

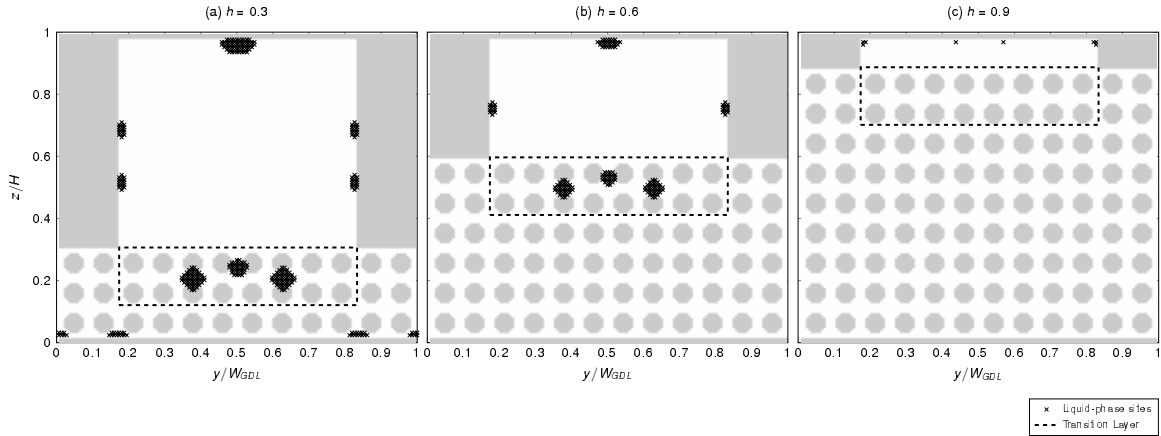


Fig. 3.7 Liquid-phase fluid sites location in the cross-sectional area and transition layer location for three different values of the relative GDL height h : (a) $h = 0.3$, (b) $h = 0.6$ and (c) $h = 0.9$.

Figure 3.7 shows the location of liquid-phase fluid sites for only three cases but results can be applied to all the other cases. They indicate that there are two main regions where water preferably tends to cumulate: (i) the upper (i.e. $z/H \sim 1$) and side walls of the GC and (ii) the interface between the GC and the GDL (i.e. $z/H \sim h$), being the latter the preferred region where water tends to cumulate.

These results confirm the key role of the TL in water cumulation phenomena. As a matter of fact, the TL is characterised by vertical pressure gradients: over it, in the GC, the flow is pressure-driven along the stream-wise direction x , while under it, in the diffusion-dominated GDL, the pressure field is altered because of the presence of solid boundaries (i.e. the GDL fibers). This induces density fluctuations and can lead to water cumulation phenomena. At a given value of the pressure gradient along x or of the Reynolds gas channel number, the bigger the relative GDL height h , the smaller the fluid shear stress variation and the vertical pressure gradient at the GC-GDL interface.

In order to prove the mechanism of density fluctuation in the TL, it can be useful to evaluate the mean density value of sites in the TL that overcome the metastable density value $\bar{\rho}_{>meta}|_{TL}$, that is, the mean value of the density fluctuations towards the liquid phase. The comparison between $\bar{\rho}_{>meta}$ averaged over the all domain and $\bar{\rho}_{>meta}|_{TL}$ on varying the relative GDL height value h reveals that the density fluctuation is more significant in the TL, as depicted in Fig. 3.8, and confirms that the GC-GDL interface is the preferred region where water tends to cumulate. Figure 3.8 also shows that the density fluctuations in the TL are more significant in the case of lower porosity (i.e. $d_p = 33\mu\text{m}$ and $d_s = 67\mu\text{m}$). Further studies will be devoted to address this issue.

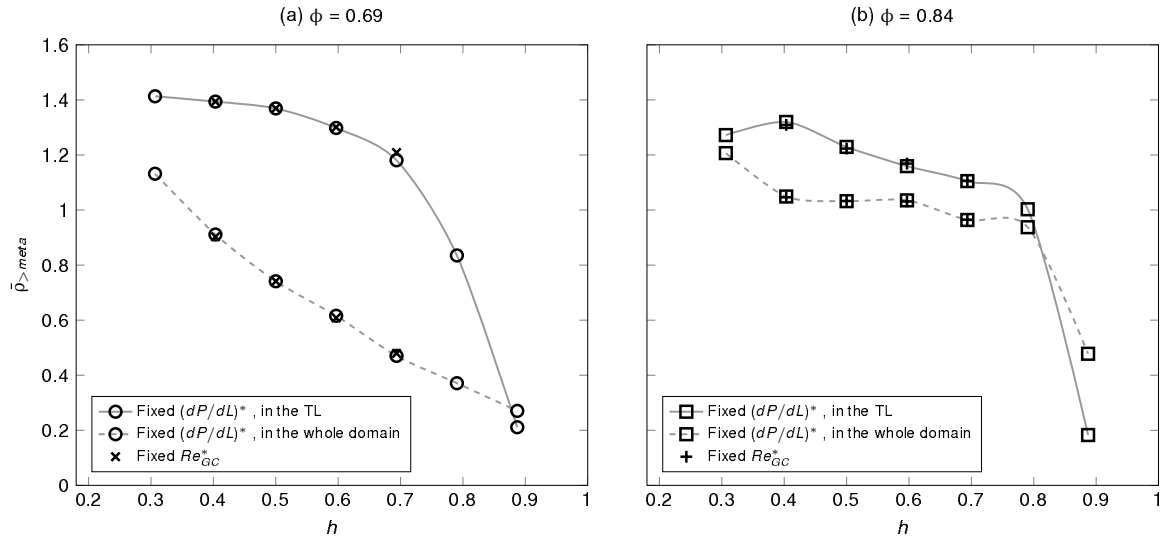


Fig. 3.8 mean density values of sites that overcome the initial metastable density value in the TL and in the whole domain with varying the relative GDL height h for: (a) $\phi = 0.69$, $dp = 33\mu\text{m}$, $ds = 67\mu\text{m}$ AND (b) $\phi = 0.84$, $dp = 50\mu\text{m}$, $ds = 50\mu\text{m}$.

However, Fig. 3.8 shows that the increase of h contributes to decrease the density fluctuations and limits water cumulation at the GC-GDL layer interface for all the considered cases. This is of vital importance in order to limit and possibly avoid the GC-GDL interface pore clogging phenomena which can significantly prevent the diffusion of reactant from the GC to the GDL.

3.2.3 Remarks

In this study the mechanism of water cumulation at the anode of PEMFCs has been investigated. In particular a three-dimensional lattice Boltzmann multiphase model has been developed in order to study the influence of geometric parameters on the mechanism of cumulation of liquid water in the GC, in the GDL and in the GC-GDL interface.

Several simulations have been carried out under different geometrical and physical conditions, leading to two main findings. First, results qualitatively agree with the experimental observation of water cumulation at the upper wall of the GC given by Hartnig et al [37] and Ge and Wang [35], but also reveal a new mechanism of water cumulation at the GC-GDL interface, more to the point, in the so called transition layer. The transition layer (i.e. the portion of flow in the GDL influenced by the flow in the GC) has been identified as the preferred region where water tends to cumulate at the anode of PEMFCs.

Second, the bigger the relative GDL height, the smaller the number of sites in liquid phase (i.e. the percent of liquid water) in the whole domain and particularly in the GC-GDL interface. This relation indicates that water cumulation phenomena are less significant in more spatially uniform flows, e.g. in a porous medium rather than in a channel-porous medium design.

The present model is a first attempt to understand the microscopic mechanism of water cumulation in PEMFCs, but it still does not consider species and thermal diffusion. Even though the latter phenomena can significantly condition the water content in fuel cells, interesting information on water cumulation can be deduced from the present results. Further studies with more realistic geometries of GDLs are necessary to attain a comprehensive insight of the relation between the porosity and water cumulation phenomena and to confirm the results of this study.

Chapter 4

Drainage Dynamics in Fuel Cells ¹

4.1 Fuel cells drainage and wettabilities

In fuel cells chemical reactions occur continuously at the membrane producing a considerable amount of water both in vapour and liquid form. In order to maintain high performances the amount of liquid in water form must be efficiently removed from the gas diffusion layer. As aforementioned in the previous chapter, if water diffuses in vapour phase from the membrane all along the gas diffusion layers cross section, it tends to condense preferentially at the GC-GDL interface. Increasing the ratio between the GDL and GC heights can help to avoid such liquid cumulation, although it requires an higher pump power. Anyway, if the water diffuses from the membrane in liquid form, the latter strategy may be not sufficient to drain the porous medium. In fact, liquid water diffusion in porous media is a very slow process compared to vapour diffusion; moreover, liquid can remain trapped in the vicinity of the membrane for very long time. This is an even worse scenario than liquid cumulation at the GC-GDL interface, since hydrogen would not reach the catalyst layer which will be covered by liquid water and any chemical reaction will be impeded.

In order to overcome this issue a Micro-Porous Layer (MPL) has been recently adopted as supplementary layer between the GDL and the membrane. [49] The main feature of the MPL is the average pore size which is between that of the catalyst layer and the GDL. As a consequence of this, there will be a capillary pressure gradient between the MPL and the GDL which forces the liquid towards the GDL. [50] Anyway this capillary pressure gradient is not sufficient to ensure an efficient drainage of the GDL since the liquid water can remain trapped in the vicinity of the MPL if no other forces are present. Adopting hydro-phobic/philic

¹ Results of this chapter have been presented at the *EFMC11* congress: D. Maggiolo, F. Picano, F. Toschi and M. Guarnieri, *Lattice-Boltzmann simulations of two-phase flows in fuel cell gas diffusion layers*, 11th European Fluid Mechaincs Conference, Seville, Sept. 12-16, 2016.

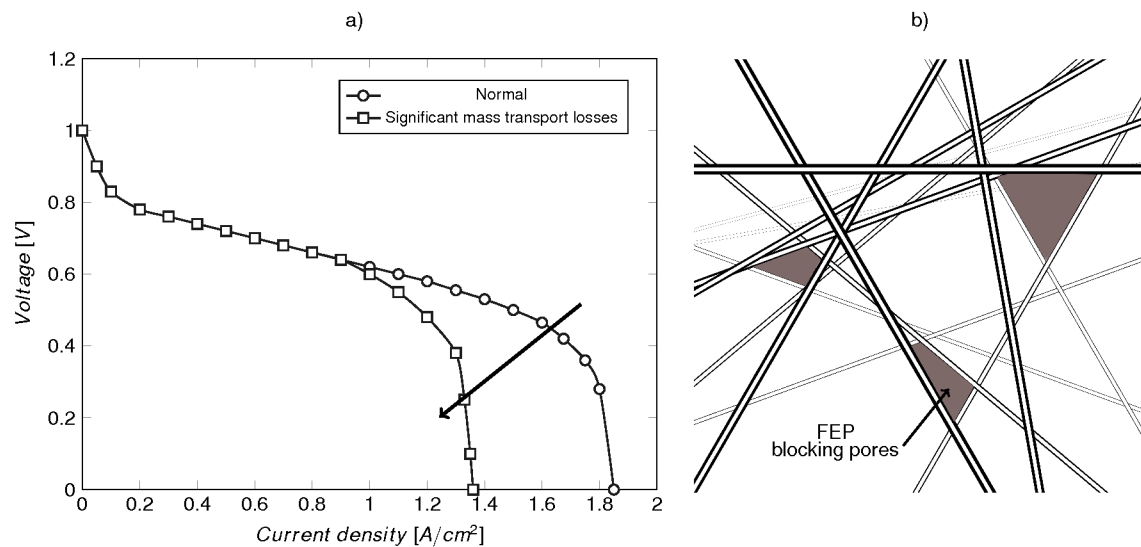


Fig. 4.1 a) Polarisation curve and possible mass losses due to pores blocked by FEP; b) sketch of FEP blocking pores as in the experimental observation of Lim and Wang [51].

materials can be a possible solution; e.g. the presence of different hydrophobicity values in the material can create a supplementary forcing and sustain the drainage mechanism of the GDL.

In fuel cells the mechanism of liquid transport in GDLs is even more complicated by the presence of phase-change phenomena (i.e. evaporation and condensation) since the thermodynamic state of the system is often close to saturation conditions. The humidification of the hydrogen, the temperature of the cell and the hydrophobic and geometric features of diffusion layers are all main factors affecting the liquid transport. Lim and Wang [51] investigated the effects of hydrophobic polymer content (fluorinated ethylene propylene, FEP) in GDLs. Their analysis evidences that an excessive FEP content in the GDL modifies its geometric characteristics by blocking surface pores and limiting cell performances, see Fig. 4.1. On the other hand, a small amount of FEP should enhance cell performances by sustaining the drainage process. Park et al. [52] stressed that the driving forces for GDL liquid removal should be other forces rather than capillarity, such as evaporation and shear forces. However, among the wide literature about liquid transport in fuel cells, experimental observations often lend themselves to different interpretations since they strongly depend, for instance, on materials, environment conditions and cell system size. [53]

Other studies focused on the fundamental understanding of the water transport in porous medium [54, 55], even recently. [56] The complex mechanism of imbibition and drainage in porous media with different wetting conditions (i.e. values of hydrophobicity) is still under investigation, especially for real porous media which presents a very complex structure. [53]

Gostick *et al.* [57] investigated the relation between capillary pressure and saturation in the GDL. The authors were able to predict a pressure-saturation curve for modelling the liquid transport more accurately. Nevertheless, to what extent the hydrophobicity of the medium influences the imbibition and drainage phenomena is still to be understood.

In this chapter theoretical models for imbibition in porous media will be briefly described and the main findings from different numerical simulations of imbibition and drainage in hydrophobic and hydrophilic fibrous porous media will be presented.

4.2 Wettability effects on imbibition and drainage in porous media

4.2.1 Introduction

The most famous equation for describing the dynamics of imbibition in porous media is the Washburn's equation. [58]. It is even called the Bell-Cameron-Lucas-Washburn equation since Bell, Cameron and Lucas derived similar relations earlier. It reads as follows:

$$h(t)^2 = \frac{\gamma \cos(\theta) R_c}{\mu} \frac{t}{2}, \quad (4.1)$$

where $h(t)$ is the time-dependent liquid penetration along the main direction x (see Fig. 4.2), γ is the capillary surface tension, θ is the liquid-vapour contact angle, μ the liquid dynamic viscosity and R_c the capillary radius.

Equation (4.1) describe the so called "spontaneous" imbibition, that is, when the only forcing is given by the wetting properties of the pores wall (and possibly gravity, not considered here). It can be directly derived from the Stokes equation:

$$\underbrace{\frac{2\gamma \cos(\theta)}{R_c}}_{\text{wetting}} = \underbrace{\left(\frac{\Delta P}{L}\right) \ell_{\Delta P}}_{\text{pressure gradient}} + \underbrace{\frac{dh}{dt} \frac{8\mu h}{R_c^2}}_{\text{viscous}} + \underbrace{\rho \frac{d}{dt} \left(h \frac{dh}{dt}\right)}_{\text{inertia}}, \quad (4.2)$$

where $\Delta P/L$ is the pressure gradient and $\ell_{\Delta P}$ is the thickness of the liquid volume. Eq. (4.2) can be integrated in order to obtain an analytic solution for imbibition dynamics. By imposing the initial condition $h(0) = 0$ and in the hypothesis of negligible inertia effects, such as in fuel cells, it follows:

$$h(t) = \left[- \left(\frac{\Delta P}{L}\right) \frac{\ell_{\Delta P} R_c^2}{4\mu} + \frac{\gamma \cos(\theta) R_c}{2\mu} \right]^{1/2} t^{1/2}. \quad (4.3)$$

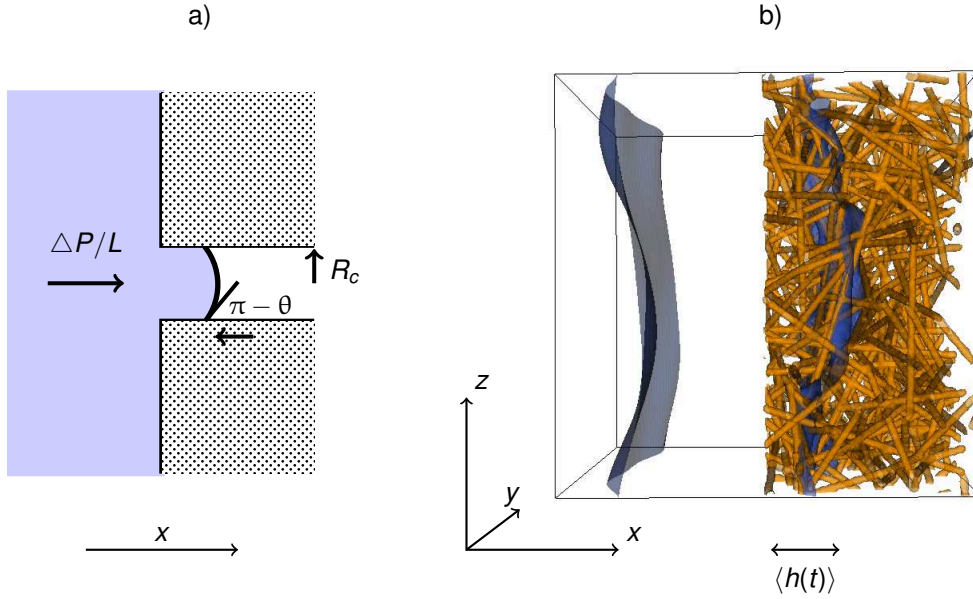


Fig. 4.2 a) Capillary imbibition model. b) Real porous medium imbibition; the blue surface represent the liquid-vapour interface

Wahburn equation can be obtained if the imbibition is spontaneous, that is the pressure gradient is null. In order to predict the saturation of a real porous medium (i.e. the ratio between the liquid volume V_l and the volume of the void-space V_v) during liquid front imbibition, one can follow the analogy proposed in Fig. 4.2 and consider that a liquid front should penetrate the pores of the medium following Eq. 4.3, on average:

$$Sat(t) = \frac{V_l}{V_v} \approx \frac{\langle h(t) \rangle}{H} = \left[- \left(\frac{\Delta P}{L} \right) \frac{\ell_{\Delta P} R_c^2}{4\mu H^2} + \frac{\gamma \cos(\theta) R_c}{2\mu H^2} \right]^{1/2} t^{1/2}, \quad (4.4)$$

where H is the thickness of the porous medium and $\langle \cdot \rangle$ denotes the spatial averaging operator so that $\langle h(t) \rangle = 1/(\varepsilon L_z L_y) \int \int h dz dy$, with L_z and L_y the lengths of the medium along z and y . Equation (4.4) conveys useful information about the two characteristic velocities of the system. The first is given by the ratio between capillary and viscous forces, while the second is given by the ratio between pressure gradient and viscous forces:

$$U_\gamma = \frac{\gamma \cos(\theta) 2R_c}{\mu H}, \quad U_{\Delta P} = - \left(\frac{\Delta P}{L} \right) \frac{\ell_{\Delta P} R_c^2}{\mu H}. \quad (4.5)$$

Given the equations above, one can rewrite Eq. (4.4) in dimensionless form simply as:

$$Sat(t) \approx 1/2 t^{*1/2}, \quad (4.6)$$

being $t^* = t(U_{\Delta P} + U_{\gamma})/H$ the dimensionless time. Equation (4.6) has been derived under the assumptions that (i) gravity and inertia effects are negligible, (ii) all variables are neither dependent on time nor dependent on space, except $h(t)$, and (iii) the tortuosity of the medium $\tau_m \approx 1$. Obviously, these assumptions are not always satisfied in real system. For instance, for the very first moments of the imbibition process inertia must be considered while viscous effects can be neglected; under these hypothesis the liquid penetration is faster in time, i.e $h \propto t$. [59] Instead, if gravity effects are important, one expects the liquid penetration growing a bit slower in time, with the imbibition at corners growing with $h \propto t^{1/3}$. [60]

Concerning the second hypothesis, significant deviation from Eq. (4.6) are expected when the contact angle θ and/or the capillary radius R_c are time dependent. For example, it is well known that the dynamic contact angle $\theta_{dyn}(t)$ can be significantly different than the equilibrium one θ , leading to different behaviours of the imbibition process. [61, 62] From another perspective, this hypothesis is equivalent to assuming that the diffusion coefficient of a liquid front imbibing a porous medium is a constant and do not depend on time or on saturation. [63]

4.2.2 Simulations of imbibition and drainage dynamics

Mechanical imbibition

In the present subsection results of different simulations of initial liquid infiltration will be presented. A liquid front has the possibility of imbibing a medium if the following inequation is satisfied:

$$\underbrace{\frac{\Delta P}{L} \ell_{\Delta P}}_{\text{pressure from forcing}} + \underbrace{\frac{2\gamma \cos(\theta)}{R_c}}_{\text{capillary pressure}} > 0. \quad (4.7)$$

Actually, Eq. (4.7) expresses the same balance between forces in Stokes equation (4.2) neglecting inertia and viscous forces at the initial time $t = 0$. In other words, if the medium is hydrophobic, the pressure given by the external forcing must overcome the opposite capillary pressure which tends to reject the water. Equation (4.7) can be reformulated as function of the characteristic velocities of the systems:

$$\frac{U_{\gamma}}{U_{\Delta P}} > -1. \quad (4.8)$$

	Forcing	θ		Forcing	θ
1	$1 \cdot 10^{-5}$	90°	3	$5 \cdot 10^{-5}$	135°
2	$5 \cdot 10^{-5}$	90°	4	$5 \cdot 10^{-5}$	129°
3	$10 \cdot 10^{-5}$	90°	5	$5 \cdot 10^{-5}$	120°
1	$1 \cdot 10^{-5}$	45°	6	$5 \cdot 10^{-5}$	108°
2	$1 \cdot 10^{-5}$	60°	7	$5 \cdot 10^{-5}$	100°
3	$10 \cdot 10^{-5}$	60°	8	$10 \cdot 10^{-5}$	135°
1	$1 \cdot 10^{-5}$	135°	9	$10 \cdot 10^{-5}$	129°
2	$1 \cdot 10^{-5}$	120°	10	$10 \cdot 10^{-5}$	120°

Fig. 4.3 Forcing pressure gradient $\Delta P/L$ and equilibrium contact angle θ values for all the considered cases of initial imbibition in lattice units.

In the case of an hydrophilic medium $U_\gamma > 0$, so that even if the external forcing is negligible, the ratio $U_\gamma/U_{\Delta P}$ will be a positive number or infinite and imbibition will occur: this is the case of the so-called “spontaneous imbibition”. In the case of no wetting, i.e. $U_\gamma \approx 0$, there must be a positive forcing for imbibition. More interestingly, in the case of hydrophobic medium, Eq. (4.8) will predict if the liquid front will penetrate on the basis of the hydrophobicity and pressure gradient values. Anyway the prediction may be inaccurate if the aforementioned characteristic velocities are not well computed. In fact, while values of pressure gradient and superficial tension, as well as values of the equilibrium contact angle are usually well know a priori, the estimation of the capillary radius can lead to significant errors.

In order to verify the applicability of Eq. (4.8), different preliminary simulations of front imbibition has been carried out by varying the medium hydrophobicity, and the external forcing. A triperiodic box has been used, see Fig. 4.2, and a liquid front of the same thickness of the porous medium has been juxtaposed it. A body force acts as a pressure gradient and push the liquid front inside the medium along the streamwise direction x . The total domain size is $L^3 = 100^3$ computational cells; the porous medium thickness is $H = L/2$ and his width $W = L$ along both y and z directions. The porous medium is composed of $n_f = 35$ fibers possibly overlapping themselves, with fiber length and diameter $\ell_f = L$ and $d_f = L/25$, respectively. Fibers are placed randomly following an uniform distribution.

The Shan and Chen multiphase model coupled with temperature (see Section 2.4) has been used in order to take into account possible effects of evaporation and condensation. The temperature at the walls and the initial temperature have been set as $T_0 = T_{wall} = 0.63 T_c$ in order to allow liquid-vapour coexistence and achieve numerical stability.

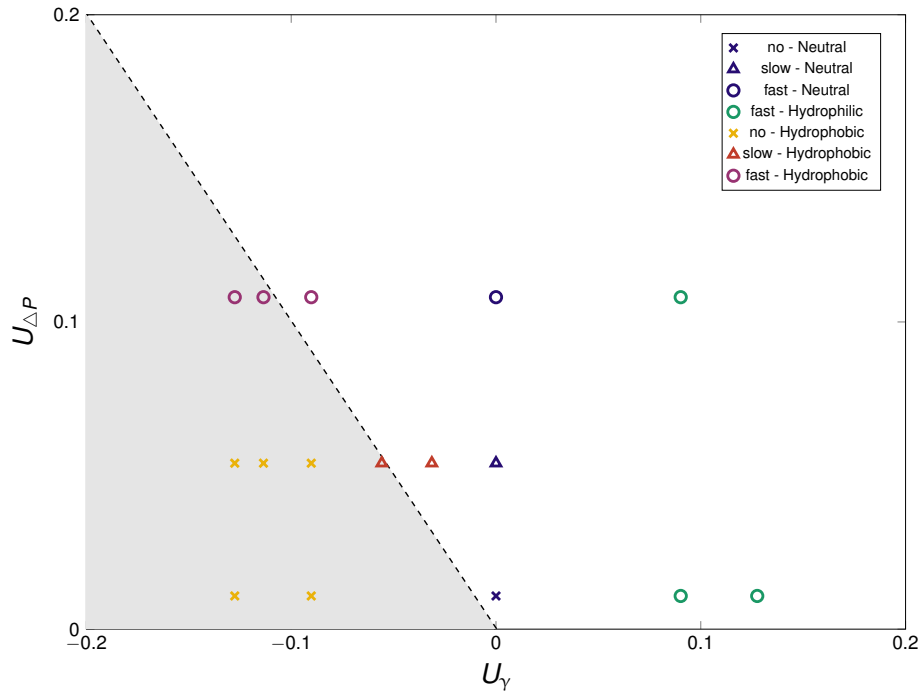


Fig. 4.4 Characteristic velocity $U_{\Delta P}$ plotted against the other characteristic velocity of the system U_{γ} . Cross, triangle and circle markers indicates no infiltration, slow infiltration and fast infiltration, respectively. Yellow, red and violet markers refer to hydrophobic media while blue and green markers refer to “neutral” and hydrophilic media, respectively.

The capillary radius R_c has been estimated as two times the hydraulic radius, i.e. $R_c = 2R_h$. The latter has been determined on the basis of the fibers diameter d_f , length ℓ_f and number n_f as follows:

$$R_h = \frac{\text{Void volume}}{\text{Wetted surface}} = \frac{W^2 H - n_f \pi d_f^2 / 4 \ell_f}{n_f \pi d_f \ell_f}. \quad (4.9)$$

Values of characteristic velocities are plotted in Fig. 4.4 while values of equilibrium contact angles and pressure gradients for each considered case are listed in Tab. 4.3. Results show a good matching between numerical values and the prediction of initial infiltration based on Eq. (4.8). When the inequality is not satisfied liquid cannot penetrate the porous medium, as expected. Small deviation from the prediction can be observed for some few cases. This can be due to the estimation of the hydraulic radius. Anyway, without loss of generality, Fig. 4.4 verifies the goodness of Eqs. (4.8) and (4.9).

After the very first times, when the infiltration is governed by the equilibrium between capillary and external forces $\Delta P/L$, viscous forces start to play a significant role and the

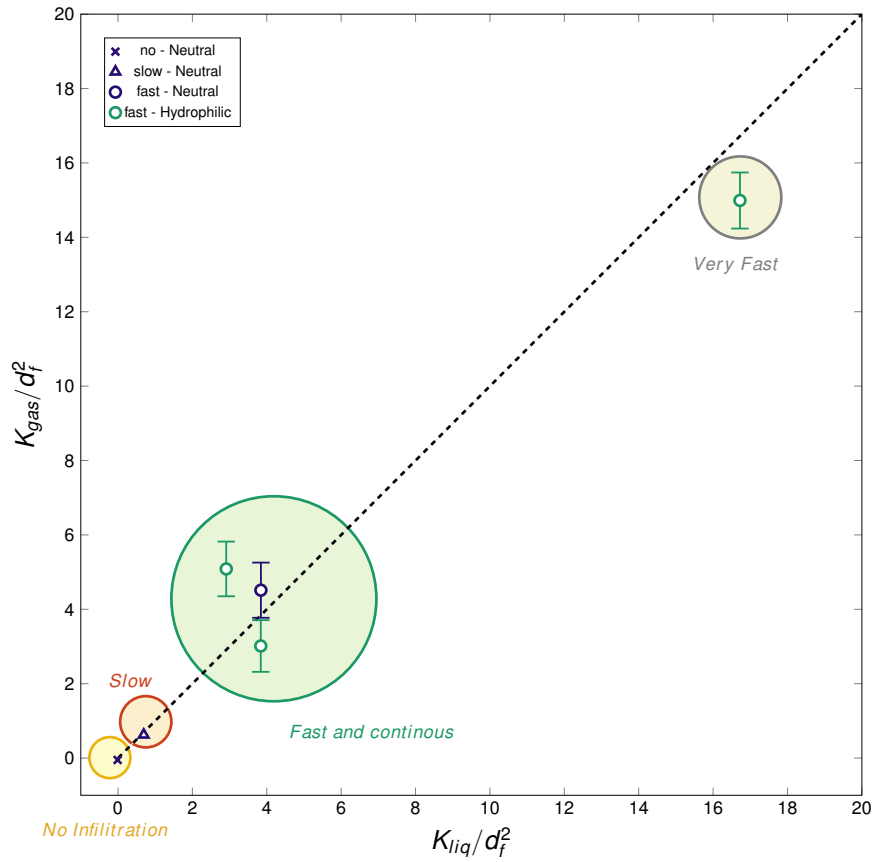


Fig. 4.5 Neutral and hydrophilic cases. Dimensionless permeability values K/d_f^2 for gas phase plotted against the dimensionless permeability for the liquid phase. Values gather around the dashed lines (the bisection $y = x$), indicating similar velocities of the phases and uniform fronts for low values. For higher values of permeability the front is broken up.

mechanism of imbibition can change case-by-case. In order to characterise the two-phase flows, permeability values K have been computed for both liquid and gas phases as follows:

$$K_{liq,gas} = \frac{\epsilon u_{liq,gas} \mu}{\Delta P/L}, \quad (4.10)$$

being $u_{liq,gas}$ the mean intrinsic velocity of the liquid and gas phase, respectively. The dynamics of the imbibing front can be strongly intermittent in time, so that K values are time-averaged in a sufficiently long range of time after initial infiltration. Figures 4.5 and 4.6 shows K values for the neutral and hydrophilic, and hydrophobic case, respectively.

If the medium has no wetting properties (i.e. $\theta = 90^\circ$, “neutral” medium), or is hydrophilic (i.e. $\theta < 90^\circ$) the liquid front can penetrate slowly or fast on the basis of the balance between forcing and capillarity. The front is maintained uniform as long as inertia effects are negligible. Conversely, in the case of strong forcing, the infiltration is much faster

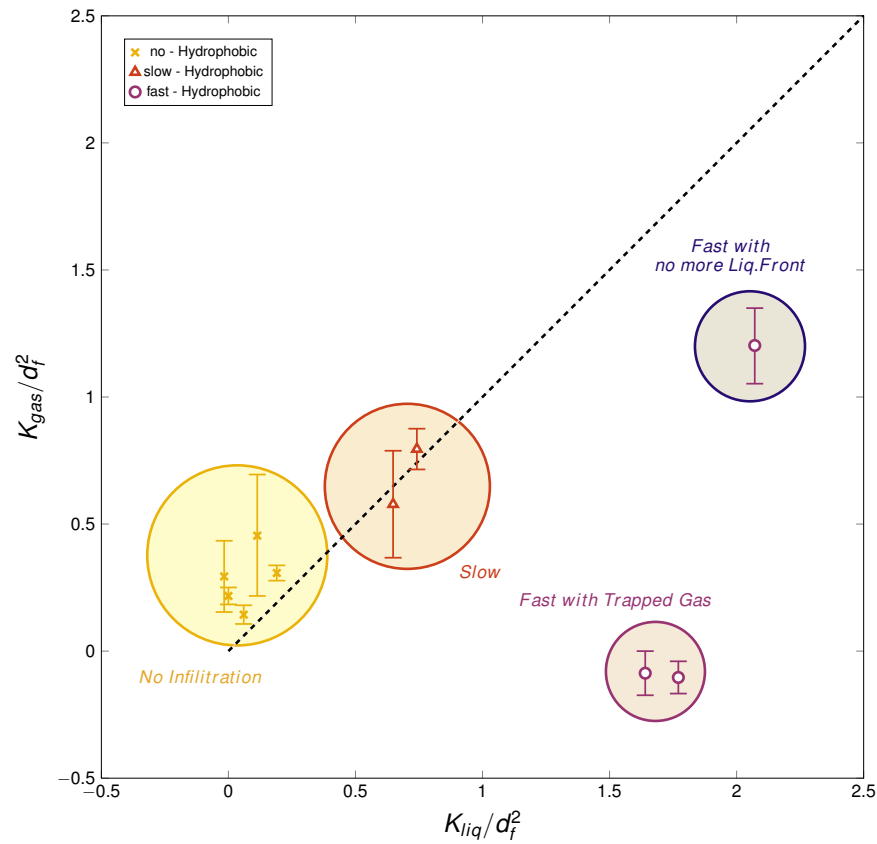


Fig. 4.6 Hydrophobic case. Dimensionless permeability values K/d_f^2 for gas phase plotted against the dimensionless permeability for the liquid phase.

and the permeability values K_{liq} and K_{gas} can be much higher, as depicted in Fig. 4.5: in this case the liquid front can be broken.

On the other hand, when the medium is hydrophobic, the infiltration mechanism and permeability values can be very different, see Fig.4.6. If the forcing is not strong enough to overcome capillary effects which are impeding the infiltration, there will be no infiltration, as well depicted in Fig. 4.7b. In the opposite case, the front can remain uniform or broke. In particular, if the forcing is strong enough, the infiltration can be fast and the front can easily break up, either forming preferential path for the liquid and trapping the gas, as in Fig. 4.7d, or forming preferential path for both phases, as in Fig. 4.7c.

Imbibition and drainage dynamics

In order to investigate the dynamics of liquid front imbibition and drainage in fibrous porous media, further simulations have been performed. Firstly, simulations of front imbibition driven by pressure gradients have been performed with varying the nematic properties of the

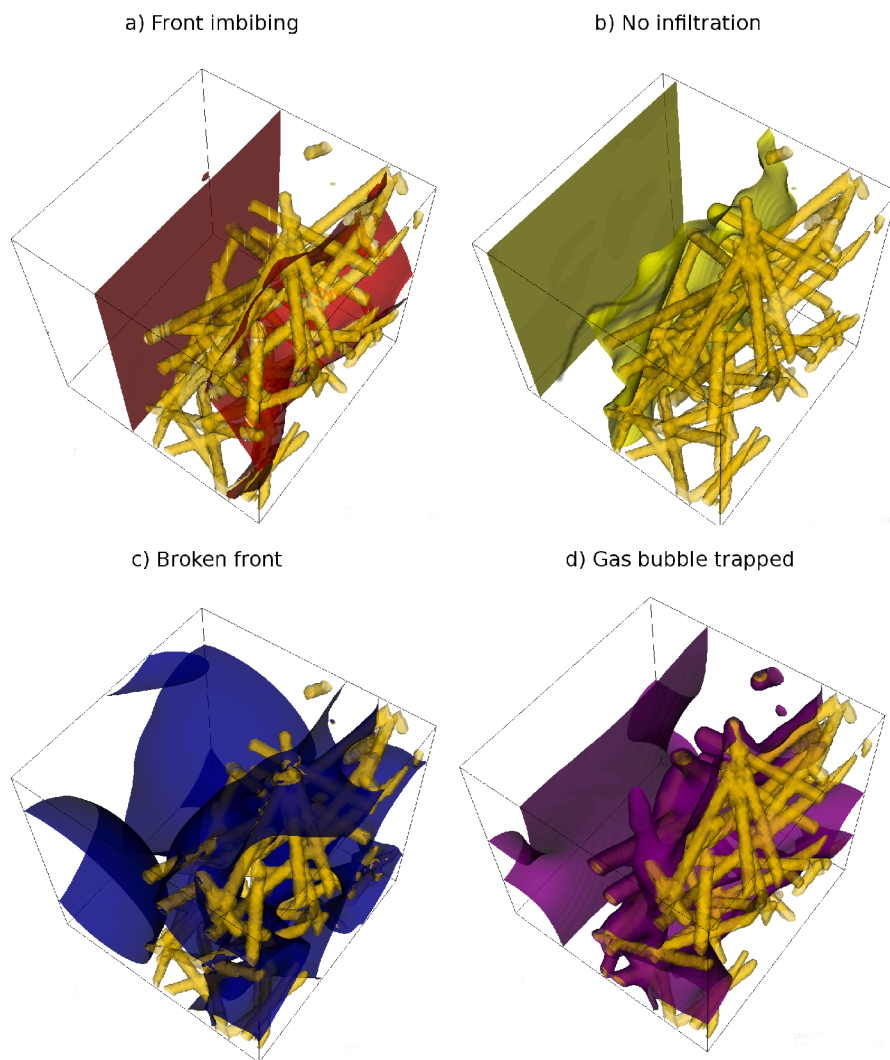


Fig. 4.7 Different cases of imbibition dynamics with varying the forcing and the hydrophobicity, i.e. the ratio $U_\gamma/U_{\Delta P}$; a) $U_\gamma/U_{\Delta P} = -0.58$ imbibition with continuous front, b) $U_\gamma/U_{\Delta P} = -1.6$ no infiltration, c) $U_\gamma/U_{\Delta P} = 0$ fast imbibition with broken front, d) $U_\gamma/U_{\Delta P} = -0.83$ imbibition with broken front and gas trapped.

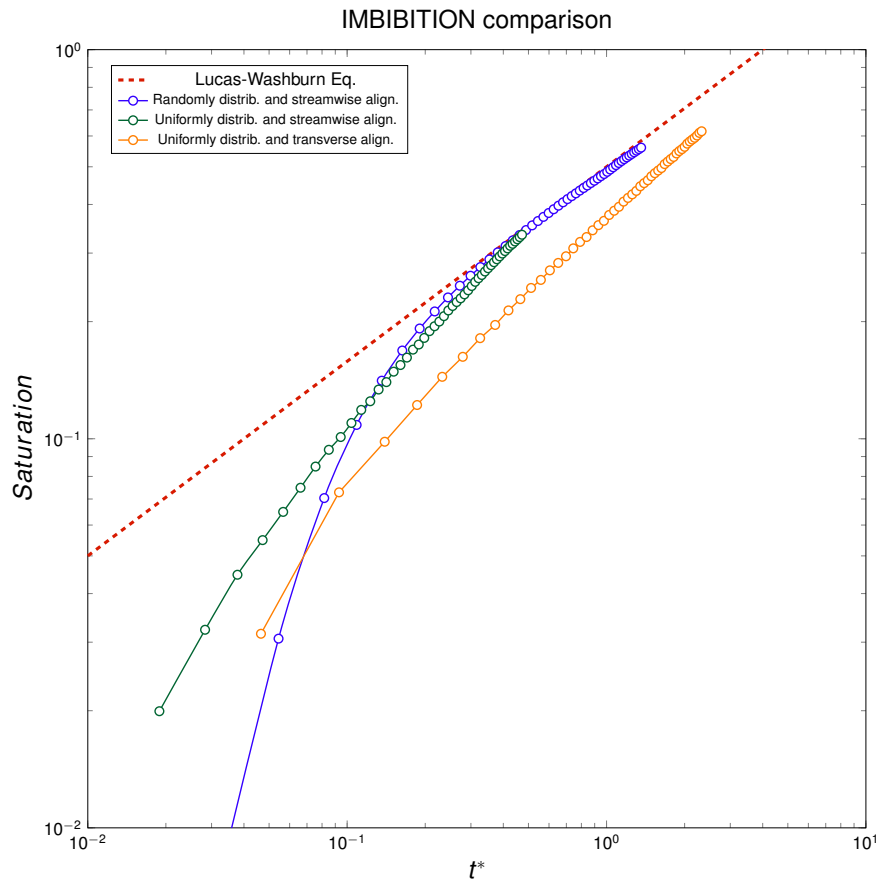


Fig. 4.8 Saturation against non-dimensional time t^* for three different geometries of the porous medium. In all the three cases the contact angle is $\theta = 90^\circ$.

medium, such as fiber orientations. Figure 4.8 depicts the saturation process for three different media: (i) a medium composed of streamwise aligned fibers uniformly distributed, (left panel of Fig. 4.9), (ii) a medium composed of streamwise aligned fibers randomly distributed (central panel), and (iii) a medium composed of transverse aligned fibers uniformly distributed (right panel). In all three cases the characteristic velocity U_γ is null since the equilibrium contact angle is $\theta = 90^\circ$.

In order to correctly scale the three cases, the capillary radius R_c has been determined as half of the maximum distance between fibers, for the uniformly distributed media. In fact results had shown that adopting the hydraulic radius as characteristic length in uniformly distributed media leads to a bad scaling. E.g. for the uniformly distributed fibers streamwise aligned $2R_H = 8.186$ which is more than two times the half of the maximum distance between fibers. Instead, a good scaling can be obtained by approximating the capillary radius with the half distance between fibers, as shown in Fig. 4.8 where curves are approaching the Lucas-Washburn solution. On the other hand, for the randomly distributed media the

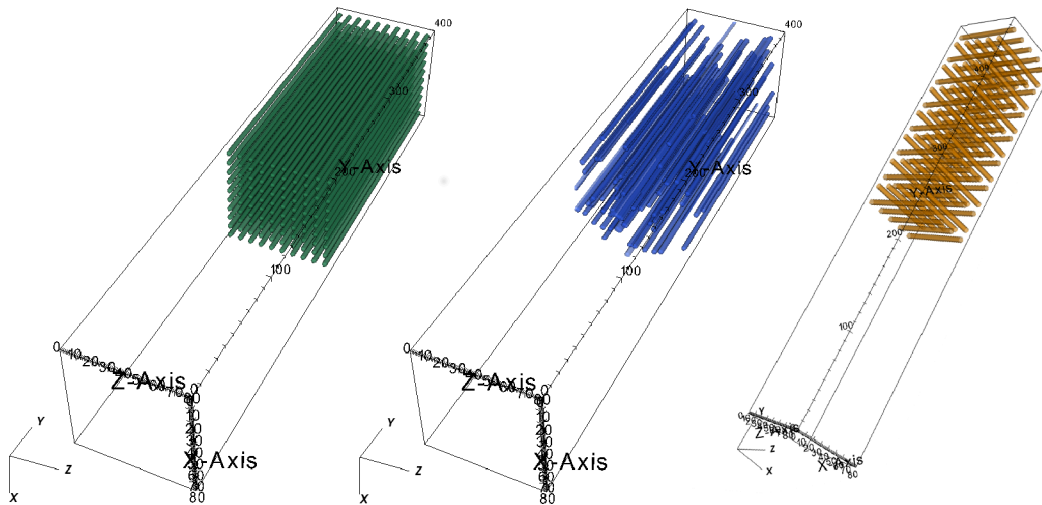


Fig. 4.9 The three different geometries considered for imbibition simulation without wetting, i.e. $U_\gamma = 0$.

capillary radius can be assessed as $R_c = 2R_H$ even for streamwise aligned fibers. This is clearly visible in Fig. 4.8 since the curve of the randomly distributed media is overlapping almost perfectly Washburn solution. In the light of this evidence the approximation $R_c = 2R_H$ has been considered valid for media composed of randomly distributed fibers.

Figure 4.8 also shows that imbibition dynamics follows a power law with $Sat \propto t^{*1/2}$ as expected from Lucas-Washburn equation, Eq. (4.6), except for very short characteristic times. This is not surprising since at very short times inertia is not negligible and the saturation process is expected to follow a power law $Sat \propto t^{*\beta}$ with $\beta \approx 1$. [59]

When fibers are uniformly distributed and oriented along the streamwise direction, the transition from the inertial regime to the viscous one is longer than for the randomly distributed media. This difference can be ascribed to the different time scaling adopted for the two cases. Instead, when fibers are transverse aligned, a slightly faster saturation dynamics can be observed from Fig. 4.8 where the slope of the curve is slightly higher. in comparison with the other cases. Anyway, it should be noted that the flow in this case is encountering fibers and void spaces alternatively. This can suggest that inertia still plays a relevant role when the liquid overcomes fibers and enlarges in the void space, leading to a different dynamic behaviour.

The distribution of fibers in fibrous porous media is not the only factor affecting imbibition dynamics. Wetting properties of the material are expected to have a strong effect, e.g. leading to very fast imbibition or drainage when the medium is strongly hydrophilic or hydrophobic, respectively. In order to catch this mechanism the so-called, “spontaneous imbibition” along

with its counterpart “spontaneous drainage” have been investigated. The former is driven by the hydrophilic properties of the material while the latter by its hydrophobic properties. A liquid front beside and inside the medium has been considered in the case of imbibition and drainage, respectively. The size of the porous medium has been increased respect to the previous simulations, in order to get more statistically significant outcomes: the domain size is $L^3 = 200^3$ computational cells while the porous medium thickness is half of the length, i.e. $H = L/2$. The equilibrium contact angles are $\theta = 50^\circ$ for the hydrophilic material and $\theta = 130^\circ$ for the hydrophobic one. It should be stressed that during the imbibition the only driving force is given by the wetting gradient formed between the void half-part of the domain, where the contact angle is $\theta_{void} = 90^\circ$, ideally, and the other half-part where fibers are hydrophilic. Without loss of generality, in the presence of wetting gradient the characteristic velocity associated with the system can be written as:

$$U_\gamma = \frac{2\gamma(\cos(\theta_2) R_{c2} - \cos(\theta_1) R_{c1})}{\mu H_{12}} \quad (4.11)$$

where $\theta_{1,2}$ are the different contact angles, $R_{c1,c2}$ the different capillary radius and H_{12} the characteristic distance between layers with different wetting conditions. Since $\cos(\theta_1) = \cos(\theta_{void}) = 0$ and $H_{12} = H$ in the present simulation, Eq. (4.11) reduces to Eq. (4.5).

Figure 4.10 shows the time-dependent saturation of the medium. Time has been scaled with the characteristic velocity of the system U_γ . After the initial stage where inertia is clearly not negligible, the curve approaches the predicted behaviour given by Lucas-Washburn Eq. (4.6). A discrepancy can be observed from Fig. 4.10: it can be interpreted by considering that both the capillary radius and the dynamic contact angle are approximated as $R_c \approx 2R_H$ and $\theta_{dyn} \approx \theta$, respectively. However the influence of the latter on this discrepancy should be more relevant than the one of the former since in Fig. 4.8 it has been shown that the hydraulic radius can well approximate the half of the capillary radius in media with randomly placed fibers. On the basis of this evidence, the discrepancy can be ascribed to the inherently dynamic nature of the contact angle. For further information about the dynamic contact angle see [61]. On the other hand, in the inset of Fig. 4.10, spontaneous drainage is depicted. The drainage process approaches a power law $Sat \propto t^{*-3/2}$. Interestingly, drainage process is much faster than imbibition. In order to interpret this different time-dependent behaviour, it can be noticed that during drainage simulations liquid can escape from the medium from both sides, while during imbibition the liquid front is entering from just one side, so that liquid can escape from the medium more easily than infiltrate in it.

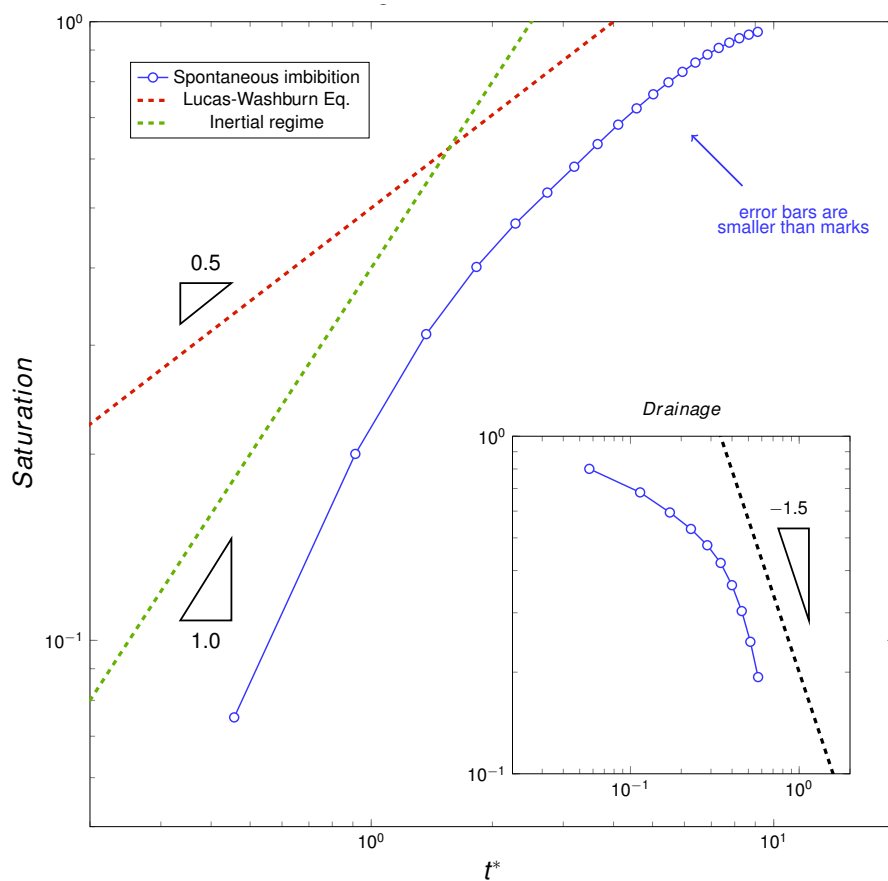


Fig. 4.10 Spontaneous imbibition dynamics. The first part of the curve approaches a law linearly dependent on time, while the second part approaches the Lucas-Washburn theoretical solution. Inset: spontaneous drainage with an hydrophobic medium.

In real gas diffusion layers of fuel cells both pressure gradients and wetting conditions of the medium are contributing to imbibition and drainage processes. A pressure difference is usually applied between the inlet and the outlet of distribution channels, that, in turn, are in contact with the gas diffusion layers. It can be difficult to predict the resulting pressure gradient in the gas diffusion layers. However, the Reynolds number of the liquid phase is expected to be of the order $Re \approx 0.1$, that is, inertial effects are considered negligible. In order to study the combined influence of pressure gradients and wetting conditions, further simulations have been carried out. The porous medium wettability has been varied, with the equilibrium contact angle θ equal to $72^\circ, 90^\circ, 108^\circ$ for the hydrophilic, neutral and hydrophobic case, respectively. Moreover, for each considered case, in order to increase statistics, three different porous media have been subjected to imbibition and drainage process, with varying random uniform distribution of Cartesian positions and azimuthal and polar angles of fibers.

Figure 4.11 depicts the dependence of saturation on time with varying the medium hydrophobicity. In all the considered cases time t has been scaled with the characteristic velocity $U_{\Delta P}$, so that results are considered valid for any value of the pressure gradient, provided that the liquid Reynolds number $Re < 1$ and inertia effects are not negligible only for very short characteristic times.

In the hydrophilic medium and in the neutral one (i.e. with $\theta = 90^\circ$) liquid imbibition dynamics follows again the power law $Sat \propto t^{*1/2}$. Deviations from the theoretical solution of Lucas-Washburn equation can be ascribed to the approximation of the contact angle $\theta_{dyn} \approx \theta$. However, the Lucas-Washburn equation appears to correctly catch the dynamics of the front imbibition. More interestingly the hydrophobic medium shows a different behaviour following a power law $Sat \propto t^{*1/3}$. In order to explain this different behaviour, one should again consider Stokes equation, Eq. (4.2); from a mathematical perspective a power law $\propto t^{*\beta}$ with $\beta \neq 1/2$ can be only justified if there is one time or space-dependent variable in Stokes equation, more than $h(t)$. As aforementioned in the previous section, the contact angle can dynamically and spatially change during infiltration process. Thus, a dynamic contact angle which strongly depends on time and front position can lead to a different time scaling exponent β . When the medium is strongly hydrophobic, some pores can repel liquid water which will not infiltrate through them. As a consequence, liquid will infiltrate along different paths, not only along the streamwise direction, possibly overcoming and rounding small pores where the pressure gradient is not sufficient to overcome surface tension effects, i.e. where $U_\gamma/U_{\Delta P} \leq -1$. The front will be strongly discontinuous in space and the mean contact angle in Eq. (4.4) will be influenced by the time-dependent front position, which

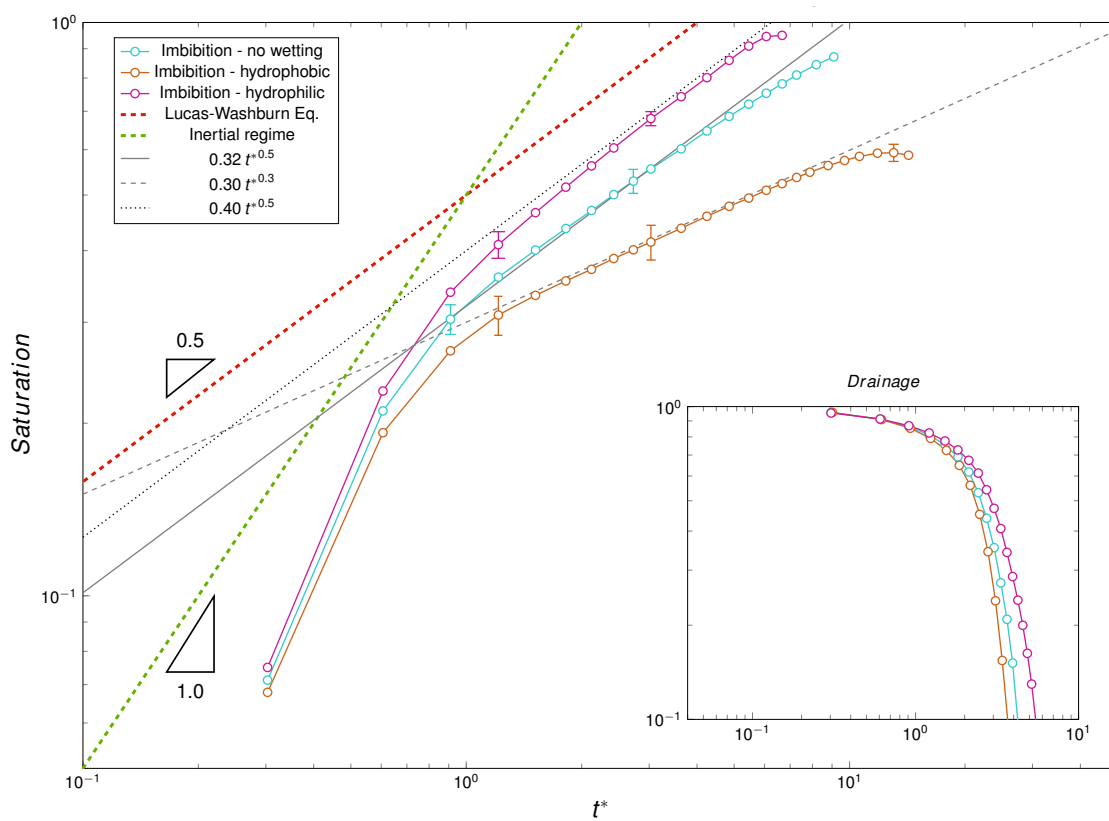


Fig. 4.11 Imbibition dynamics with varying the hydrophobicity of the medium. Neutral (cyan) and hydrophilic (magenta) media saturation dynamics can be described by the Lucas-Washburn law, while the hydrophobic medium (orange) follows a different time scaling with $Sat \approx 1/3t^{*1/3}$. Inset: drainage dynamics of the same media.

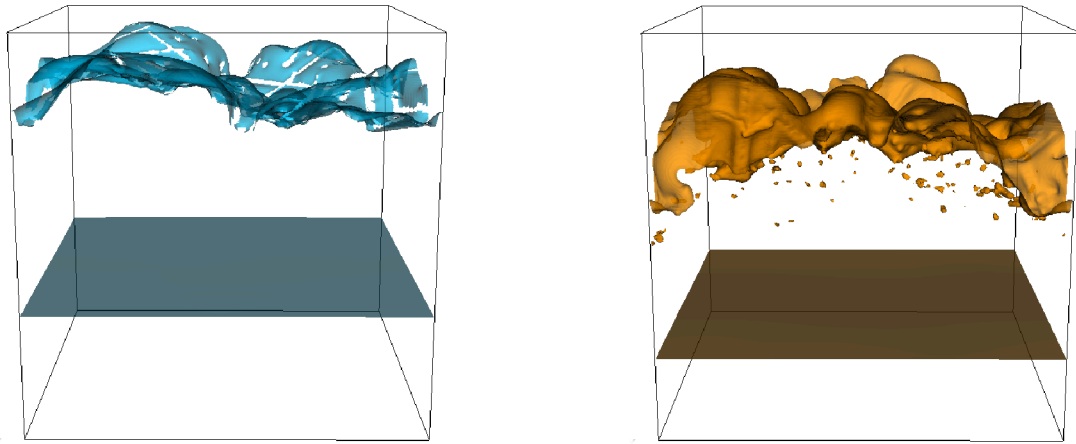


Fig. 4.12 The liquid front in the neutral (left panel) and hydrophobic (right panel) medium. The front infiltration is more discontinuous in the hydrophobic medium with pores being clogged: this behaviour is considered to be responsible of the different time scaling of the imbibition process.

in turn will lead to a different time scaling. The same effect is expected in highly tortuous media where the liquid front is usually discontinuous.

Actually, the Lucas-Washburn solution is a special case of the more general Richards equation. [63] Richards equation reduces to Lucas-Washburn when the so called “soil water diffusivity” is not dependent on local saturation concentration and hence is constant in time. This hypothesis is easily violated when the medium is strongly hydrophobic since the local saturation can be very different than the averaged one.

In other words, the imbibition process in strongly hydrophobic media can significantly deviate from the Lucas-Washburn equation since it is strongly intermittent and discontinuous in space and time. Figure 4.12 shows two snapshots of simulations of neutral (left panel) and hydrophobic (right panel) media which highlight the difference between them.

Double wetting layer

It can be interesting at this point investigate to what extent the imbibition and drainage phenomena can be facilitated in fibrous porous media by tuning the wetting properties of the material. In fact, in fuel cells, water is generally believed to be produced at the catalyst layer, in liquid or vapour form. In the case water is produced in liquid form, it erupted from the microporous layer and reaches the bottom of the gas diffusion layer. It has been

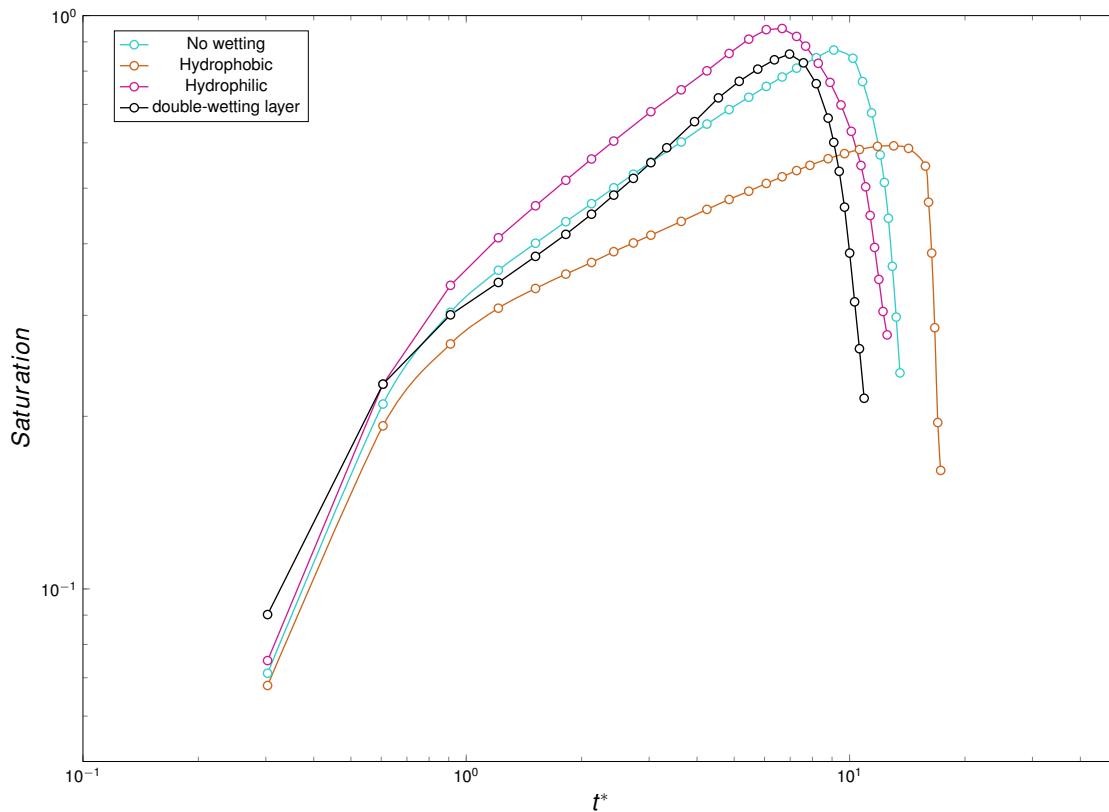


Fig. 4.13 Double-wetting layer with the first and second part hydrophobic ($\theta = 120^\circ$) and hydrophilic ($\theta = 60^\circ$), respectively, compared with a neutral, fully hydrophilic and fully hydrophobic medium. The time spent for a complete imbibition-drainage cycle is smaller for the double-wetting case.

proven that the microporous layer help to fast remove water from the catalyst layer since its microstructure is characterised by very small pores of the order of nanometers, which in turn increase capillary pressure and push away water.

Anyway, when liquid water reaches the GDL, it is not more subjected to high capillary pressure and it can stuck at the MPL-GDL interface. A proper designed medium would promote the water imbibition and drainage at that interface, pushing liquid water in the upper part of the GDL and facilitating the gas-phase transport at the same time. The benefit of using a MPL is given by its capability of repelling water by inducing a pressure gradient along the through-plane direction. In order to reach a similar situation in the GDL, the imbibition and drainage mechanisms of a *double-wetting* layer are investigated in the present section.

The double-wetting medium is hydrophobic in the lower part and hydrophilic in the upper one, with the two contact angles equal to 120° and 60° . Figure 4.13 shows the complete cycle of imbibition and drainage for four different cases of wetting conditions: (i) a neutral medium with $\theta = 90^\circ$, (ii) a hydrophilic medium with $\theta = 60^\circ$, (iii) a hydrophobic medium

Medium	\mathcal{E}
Neutral	0.09
Hydrophobic	0.08
Hydrophilic	0.55
Double-wetting	0.56

Table 4.1 Liquid water transport efficiency of different media.

$\theta = 120^\circ$ and (iv) the double-wetting medium. The imbibition process through the latter, is firstly similar to the hydrophobic one, with saturation following a power law $\propto t^{1/3}$. This is not surprising since the first part of the medium is hydrophobic. However, for higher characteristic times, the behaviour changes: saturation dynamics is much faster following a power law $\propto t^\beta$ with $\beta > 0.5$. This unusual behaviour can be explained by taking into account two effects: from one side, the first hydrophobic part, after first imbibition, tends to push away water while from the other side, the hydrophilic part is pulling water to the final part of the medium. The combination of these two effects is considered to be responsible of this fast imbibition and drainage process.

In order to quantify the capability of the medium to gather and release water, i.e. to perform a complete imbibition and drainage cycle, the following value is identified:

$$\mathcal{E} = \frac{Sat_{max} - 0.1}{t_{0.1}^*} \quad (4.12)$$

where Sat_{max} is the maximum saturation reached at the end of the imbibition and $t_{0.1}^*$ is the time spent to reach a saturation equal to 10% at the end of the drainage. Table 4.1 contains calculated values of the latter quantity for each case. It is clear that the double-wetting medium presents the higher value of efficiency in terms of transported water per time unit, i.e. \mathcal{E} .

Temperature effects

Concerning the temperature dependence of the imbibition and drainage process, no significant effects of temperature and phase change have been observed. Figure 4.14 shows the time-dependent temperature profiles during imbibition and drainage. The temperature change is less than 4% for all the considered cases. Fig. 4.14 also shows that during imbibition and drainage the mean temperature of the system increases and decreases, respectively. Consequently, it appears that the equilibrium temperatures inside and outside the porous medium are slightly different in comparison with the initial ones.

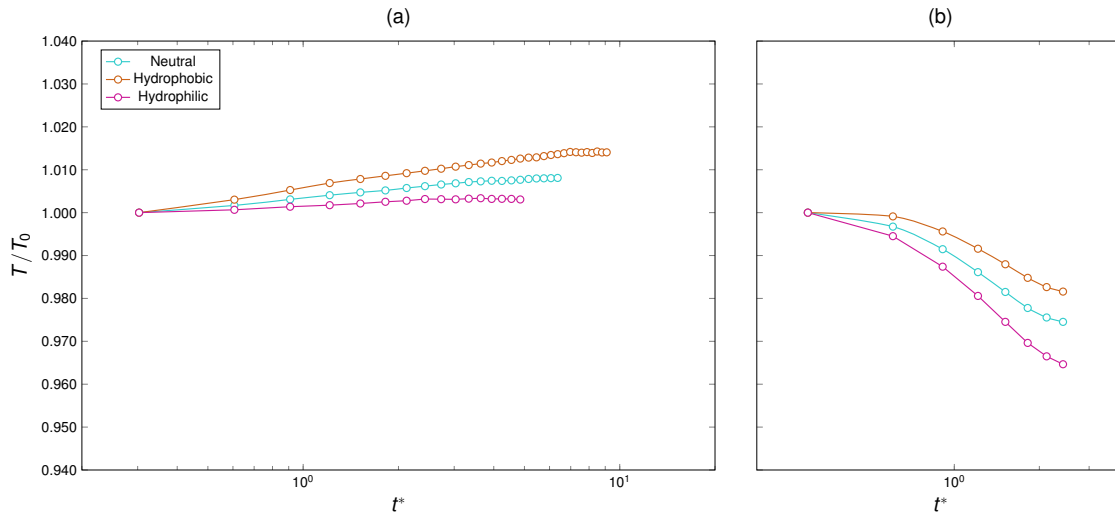


Fig. 4.14 Non-dimensional system temperature T/T_0 variation in time during imbibition (left panel) and drainage (right panel).

Figure 4.15 depicts the change in liquid mass m_{liq} in respect to the initial liquid mass $m_{liq,0}$ as function of the change of temperature T/T_0 . During imbibition temperature and liquid mass slightly increase proportionally, suggesting small condensation with latent heat released. Conversely, during drainage liquid mass increases and temperature decreases. Therefore both during imbibition and drainage a small amount of vapour condenses but the latent heat production is negligible. The amount of condensed vapour is very small (i.e. $2 \div 4\%$) so that the small variations in liquid mass and system temperature can be ascribed to the change in equilibrium densities due to the forcing and phase-change phenomena can be considered negligible in the present study.

4.3 Simulations of condensation and drainage in fuel cells

In real fuel cells, two-phase flows are much more complicated than the ones described by simplified problems of imbibition and drainage which have been discussed in the previous section. Firstly, the upper part of the GDL is in contact with graphite plates in which a serpentine is engraved in order to ensure gas distribution all along the GDL. Thus, the GDL is in contact with both Gas Channels (GC) and ribs. see Fig. 3.3. This can strongly influence liquid mass transport since the temperature of the solid-phase at ribs can be very different than the temperature in the gas-phase in distribution channels. Secondly, the pressure gradient usually acts along the in-plane direction parallel to the channels axes, so that the force which pushes water from the low part of the GDL to the GC is very weak.

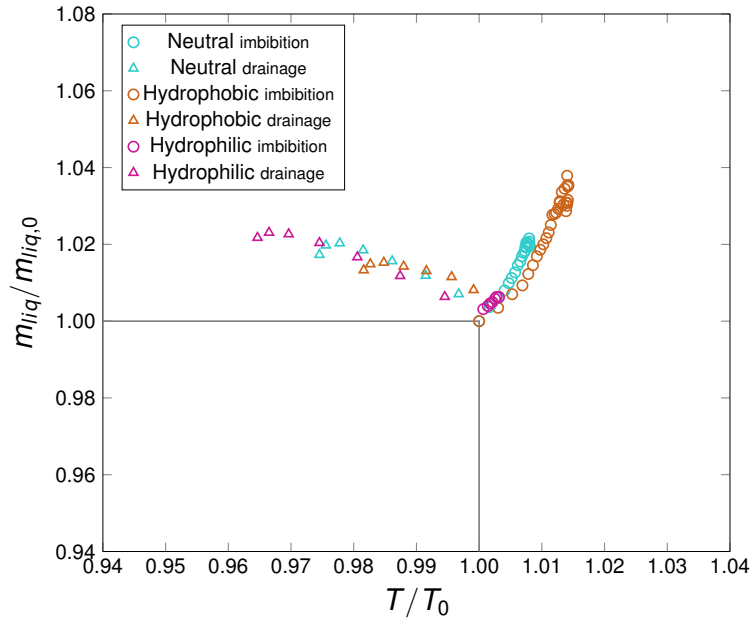


Fig. 4.15 Non-dimensional liquid mass $m_{liq}/m_{liq,0}$ variation as function of the non-dimensional system temperature T/T_0 .

In order to take into account the aforementioned issues, different simulations of the GC-GDL interface have been performed. The domain is composed by both GDL and GC while the Micro-Porous Layer (MPL) has been simulated as a wall with strong hydrophobicity (i.e. $\theta_{MPL} = 140^\circ$) in order to take into account its feature of liquid repulsion. The domain size is 160, 200 and 300 computational cells along the wall-normal, the span-wise and the streamwise direction, respectively. A pressure gradient $\Delta P/L$ has been applied by means of a body force in order to simulate the typical flow inside the cell. Following Eqs. (3.1) and (3.2) the gas channel Reynolds has been fixed as $Re_{GC}^* \approx 70$, taking into account the gas in the cathode side, which is oxygen. Anyway results of this simulation can be applied even to the anode side where the gas channel Reynolds number is expected to be of the same order of magnitude. The ratio between the GDL height and the total GC-GDL height is $h_{GDL}^* = 0.375$, the number of fibers composing the medium is $n_f = 250$ and their length is $\ell_f = 200$. The temperature has been fixed at 70° at all the solid phase. In order to investigate the possible benefits of producing GDLs characterised by different wetting conditions, the following simulations have been performed: (i) a neutral GDL, $\theta = 90^\circ$, (ii) an hydrophobic GDL, $\theta = 120^\circ$, and (iii) a double-wetting GDL with $\theta = 120^\circ$ and 60° in the lower and upper part, respectively. Figure 4.16 schematically represents the three different simulations.

At the initial stage $t^* = 0$ the lower part of the GDL is completely filled of liquid water and its thickness is $\ell_{water} = 10$ computational cells. The latter initial condition has been

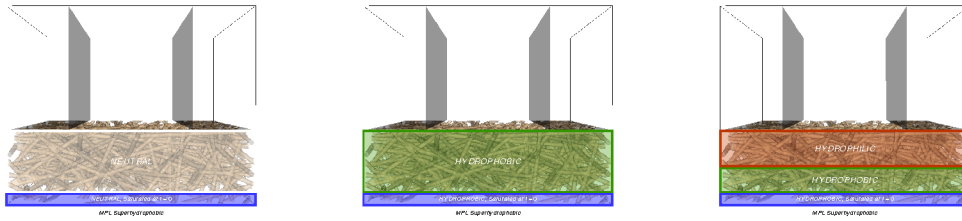


Fig. 4.16 Three different cases of GDL wetting: on the left, a neutral (no wetting) medium; on the centre, a hydrophobic medium; on the right, a half hydrophobic/half hydrophilic medium. The GDL is in contact with both the channel and the ribs of the upper plate. At the initial stage of the simulation the bottom of the GDL is filled with liquid water in order to simulate a possible condition of condensation of the cell. The lower wall is super-hydrophobic, in order to simulate the MPL.

chosen in order to investigate the operative condition of a cell when the water erupts from the MPL in liquid form. A GDL which ensures high performances should be completely dried or at least its lower part. Thus, the time-dependent saturation of the lower part of GDLs highlighted in Fig. 4.17 has been investigated along the wall-normal direction.

Results are shown in Fig. 4.18. Given the presence of a wetting gradient from the lower to the upper part of the GDL and since the pressure gradient is acting along a direction normal to the direction investigated, the characteristic velocity of the system U_γ has been determined following Eq. (4.11). In the first case, the GDL is neutral and the contact angles in Eq. (4.11) are $\theta_1 = 90^\circ$ and $\theta_2 = 140^\circ$, while in the second and third case, $\theta_1 = 120^\circ$ and $\theta_2 = 140^\circ$. It should be noted that the volume of void-space filled with liquid water is about half of the investigated volume of void-space, so that their heights are $H_{filled} = 1/5 H_{GDL}$ and $H_{investigated} = 2/5 H_{GDL}$, respectively. Consequently the expected maximum saturation in the investigated volume is $Sat_{max} \approx 0.5$.

For all the considered cases the maximum saturation is about $Sat_{max} \approx 0.3$, less than expected, indicating that some void parts of the medium cannot be filled with liquid water because they are not connected with the others. When the contact angle is 90° , saturation dynamics is very slow since the pressure gradient is perpendicular to the wall-normal direction and it does not contribute significantly to the liquid imbibition of the investigated volume. Moreover, once liquid infiltrates, it does not move anymore and the drainage process does not take place, as well depicted in Fig. 4.18. When the diffusion layer is completely hydrophobic the imbibition process is much faster but liquid gets stuck on the lower part as well.

Conversely, when a two-wetting layer is adopted, the drainage process is enhanced. In particular, liquid water infiltrates at the same rate as in the fully hydrophobic case but its removal from the lower part of the GDL is possible only if the upper part is slightly

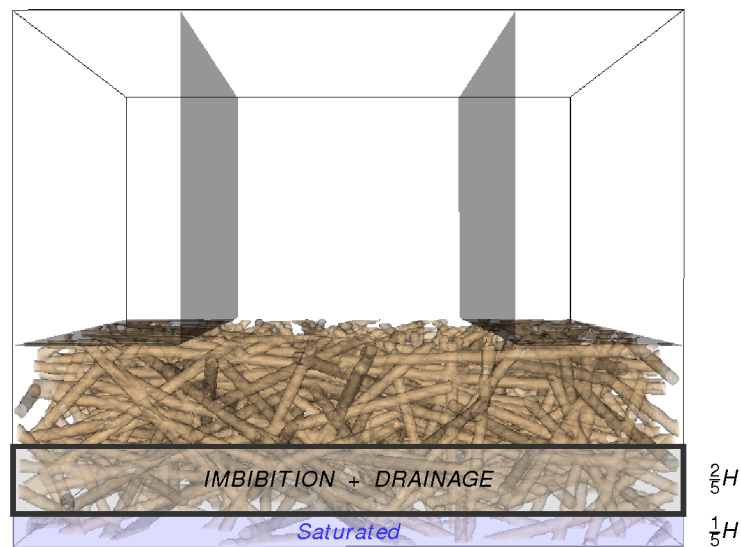


Fig. 4.17 The fuel cell simulated with the lowest part of GDL filled with liquid water. The imbibition and drainage process of the low part of GDL highlighted in black has been studied.

hydrophilic. In other words, wetting gradients along the wall-normal direction support the liquid movement from the MPL to the gas channels. Figure 4.18 also shows how imbibition and drainage processes can be further enhanced by orienting the fibers composing the medium preferentially along an inclined plane forming with streamwise and wall-normal directions an angle of 45° .

In conclusion, it has been shown how wetting properties of a fibrous porous medium affect imbibition and drainage phenomena, by altering the capability of the medium to be penetrated by liquid water. For practical applications, in gas diffusion layers of fuel cells, wetting properties can be tuned in order to enhance liquid removal. In particular, results of present simulations suggest that liquid water can be easily repelled from the bottom of the GDL by treating it half hydrophobically-half hydrophilically.

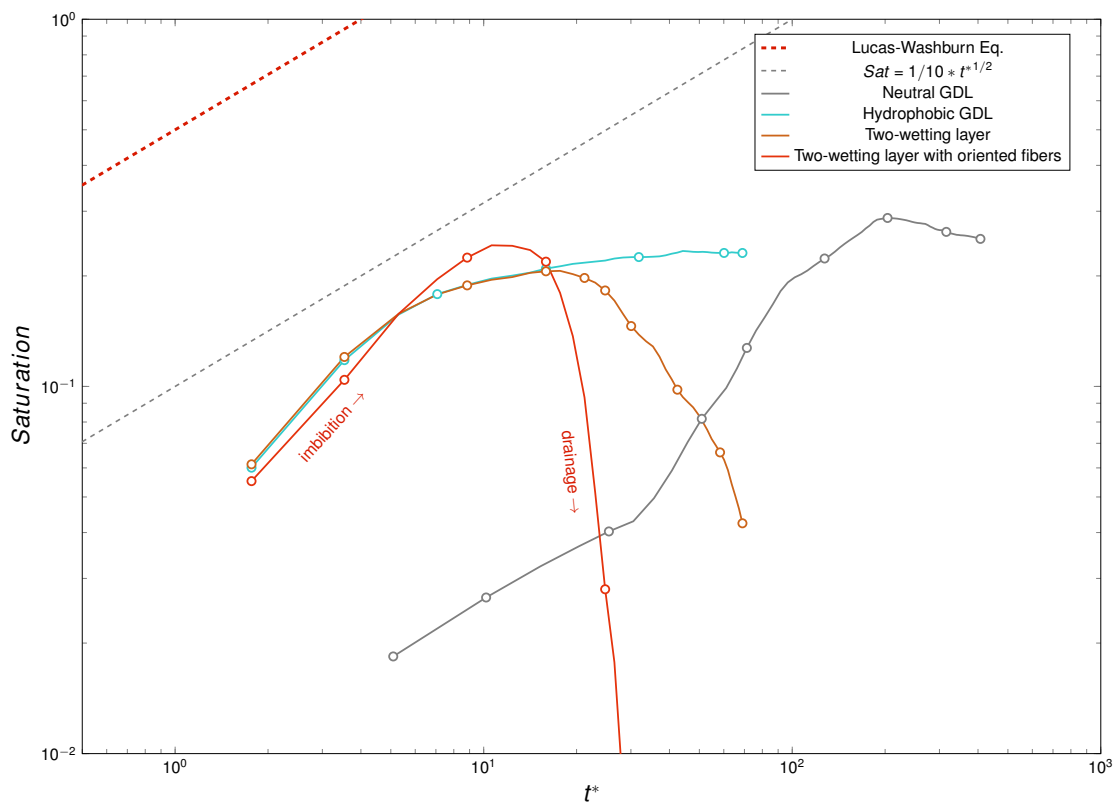


Fig. 4.18 Imbibition and drainage of the low part of the GDL: the red curve indicates the case with two-wetting GDL with oriented fibers, which is the more efficient case in removing the liquid water.

Chapter 5

Fluid Dynamics in Flow Batteries ¹

5.1 Design of flow batteries

In comparison with fuel cells, in flow batteries the fuel is provided by liquid electrolyte solutions which are supplied from external tank. From a fluid-dynamic point of view, since there are not two-phase flow phenomena, the most interesting physical phenomenon is species dispersion inside diffusion layers. The latter are typically composed of carbon fibers as in fuel cells. Reactants are carried by flows inside distributing channels which assist in spreading them uniformly all along porous surfaces.

Obtaining an uniform electrolyte distribution inside the medium is crucial in order to exploit all the battery capacity, but it is not a simple task. In fact, necessarily, the design of distributing channels either entails an high number of stagnation zones or an high value of pressure drops. [10] Consequently, the optimal macroscopic design would ensure a good balance between homogeneity of the electrolyte distribution and pump power demand necessary to guarantee it.

In the present chapter different simulations with varying the flow battery design of distributing channels will be presented and the best configuration for all-Vanadium Redox Flow Batteries will be identified.

¹ A version of this chapter has been published in *Journal of Physics: Conference Series*: S. Bortolin, P. Toninelli, D. Maggiolo, M. Guarnieri and D. Del Col *CFD study on electrolyte distribution in redox flow batteries*, Vol 655, 012049, 2015, DOI:10.1088/1742-6596/655/1/012049

5.2 Study on electrolyte distribution in redox flow batteries

5.2.1 Introduction

The recent attention to environmental problems has led to an increasing use of renewable sources. However, the intermittent nature of most renewable energy sources has posed a serious challenge for widespread application and for an effective replacement of conventional sources. Therefore, energy storage plays a crucial role in the delivery of electricity from renewable sources, such as solar and wind, providing a solution for the balance problem between the generation and the consumption of the electric power. Nowadays, several energy storage technologies, characterised by different levels of development, have been proposed (e.g. pumped hydro, electro-chemical, thermal, compressed air, flywheel...) as reviewed by Alotto *et al.* [4] Among electro-chemical systems, redox flow batteries (RFBs) represent one of the most recent technologies and a highly promising choice for stationary energy storage. Unlike conventional batteries, in which energy is stored in the battery structure, redox flow batteries store energy in two solutions containing different redox couples with proper electro-chemical potentials. The electrolyte is stored in two separated tanks. The most appealing features of this technology are: scalability and flexibility, independent sizing of power and energy, long durability, fast responsiveness, and reduced environmental impact. Such features allow for wide ranges of operational power and discharge time, making RFBs an ideal solution for assisting electricity generation from renewable sources. The power size depends on the flow rate of electrolyte and the configuration of the cell stack, whereas the energy stored depends on the reactants chosen, their concentration and the size of the reactant tanks.

The main element of RFB is the membrane-electrode assembly (MEA) where the reduction and oxidation reactions take place in two liquid electrolytes (aqueous and not-aqueous) that contain a given concentration of metal ions (the active material). The MEA is composed by two catalysed electrodes (porous media such as carbon felt or metallic foam) with an interposed polymeric membrane. Finally, the RFB is closed by two plates containing the frame flow that can have different configurations to guarantee the best electrolyte distribution inside the porous media. During the charge/discharge operations, the electrons obtained from the redox reactions are collected by one electrode and go to the other one through an external circuit, whereas the ions migrate through the membrane. As compared to the conventional electro-chemical batteries, the electrolytes are not permanently sealed, but they are stored in tanks and pumped into the cell stack. Furthermore, if the material of the two electrolytes is

the same, as in the case of the vanadium redox flow batteries, then the cross-contamination problem during operation is limited. For these two aspects, the electrolytes have no degradation and a long life of RFB is guaranteed and can be also improved by its configuration, i.e. number of tanks, regulation of flow, type of electrolytes, electrodes, membrane and so on, as analysed by Cunha *et al.* [64] The RFB can be categorised by the active species or solvent (aqueous and non-aqueous, respectively), as reported in detail by Weber *et al.* [10] and Ponce de León and coworkers [65].

There are three important aspects related to RFBs design:

- the dimension of whole plant: it is pretty large making their use difficult for a mobile application, as reported by Cunha *et al.* [64];
- the electrolyte temperature in the RFB: it can be controlled through the flow rate avoiding the solution precipitation that occurs outside the allowed operating temperature ranges. For example, a numerical investigation on temperature field inside the MEA has been performed by Wei *et al.* [66];
- the flow field design to achieve uniform distribution of the electrolyte with low pressure drop, minimising the mass transfer polarisation and avoiding problems about solubility limits, as analysed by Weber *et al.* [10], Xu *et al.* [67] and Wei *et al.* [66]

This study aims at analysing the flow field inside the MEA where the electro-chemical reactions take place. As mentioned above, the RFB performance is strictly influenced by the electrolyte distribution inside the carbon felt: it is important to investigate the best electrolyte distribution avoiding high pressure drop and stagnation zones inside the porous region. In the following sections, the geometry of different distribution layouts, the setting of CFD simulations and, finally, the results are reported in detail to evaluate the best configuration.

5.2.2 Set-up and numerical methods

In the scientific literature, different configurations have been proposed for the distribution of the electrolyte inside the porous felt where electro-chemical reactions take place. In particular, two types of solutions can be found: with the first method (indirect feeding), the felt is fed by channels machined in the containing plates of the cell (e.g. parallel channels, serpentine channels), whereas the second solution consists of direct feeding the felt without the use of channels. In the present work, the authors have focused their attention on four possible geometrical configurations (table 1), with the aim to improve the electrolyte distribution and to evaluate the pressure drop inside the RFB cell. For all the configurations, the geometry of the carbon felt is the same (length 260 mm, width 160 mm, depth 4.3 mm), beside the

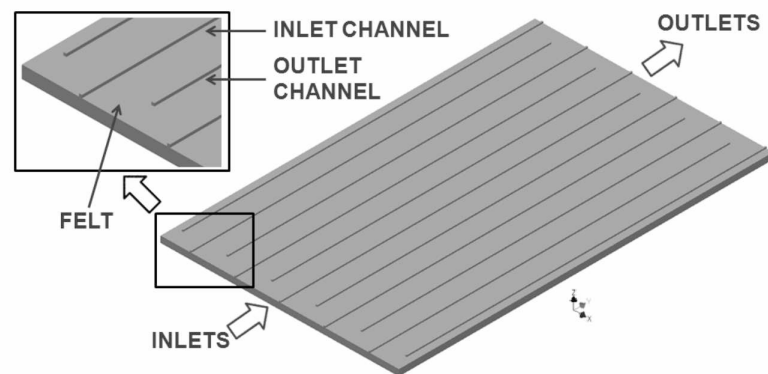


Fig. 5.1 The carbon felt with distribution channels (configuration 1).

Configuration	Feeding	Hydraulic diameter [mm]	Number of channels	Number of outlet channels
1	Indirect	1	5	6
2	Indirect	2	5	6
3	Indirect	2	4	4
4	Direct	1	5	6

Table 5.1 Selected configurations for the distribution of the electrolyte.

number and the hydraulic diameter (h.d.) of the square channels is varied. The first three configurations reported in table 1 are referred, as mentioned above, to the indirect feeding: the electrolyte enters the parallel square channels placed above the carbon felt (Fig. 5.1, case with 5 inlet parallel channels), then it is sent through the porous zone and it finally exits from the outlet channels (Fig. 5.1, case with 6 outlet channels). Instead, in the last configuration, the felt is directly fed with the electrolyte.

The four selected configurations reported in Tab. 5.1 are used to analyse the influence of the following

- geometrical parameters on the electrolyte distribution inside the carbon felt:
- hydraulic diameter of the square channels forming the frame flow inside the MEA;
- number of inlet/outlet channels and their position on the carbon felt; direct/indirect feeding of electrolyte inside the porous zone.

Mesh

For all the configurations, a three-dimensional domain with a structured mesh has been considered. For the purpose of computational time savings, the mesh is finer for regions

n_m	J [A m ²]	A_m [m ²]	α_Q	SOC _{min}	c_V [mol m ⁻³]	F [C mol ⁻¹]
2	2000	0.0416	1	0.25	1600	96000

Table 5.2 Values of the parameters adopted in Eq. (5.1)

near the channels walls and in the contact zone between the felt and the channels, whereas it is much coarser in the rest of the volume. In the case of the first three configurations, the mesh is composed of about $7.0 \div 7.6 \cdot 10^6$ hexahedral cells while, for the last configuration, the mesh is composed of about $5.7 \cdot 10^6$ elements. Furthermore, a mesh independence test has been performed for the first case. A new structured mesh composed of about $3.7 \cdot 10^6$ elements has been designed. The maximum deviation between the velocity field obtained with the two different meshes is about 1%.

Numerical Methods

Three-dimensional and steady-state numerical simulations have been performed with ANSYS Fluent 15. The working fluid is a sulphuric acid water solution in which vanadium oxides are dissolved. The fluid is considered incompressible and its density and dynamic viscosity are, respectively, equal to 1354 kg m^{-3} and 0.006 Pa s , as reported by Blanc and Rufer [68] and Tang et al. [69] In all the simulations, the velocity inlet condition has been calculated from an estimation of the cell volumetric flow rate Q_{cell} that was considered to be the same for all the studied cases. The evaluation of volumetric flow rate has been performed at fixed operational conditions of the RFB, as reported in Eq. (5.1):

$$Q_{\text{cell}} = n_m n_{ch} A_{ch} U_{in} = \frac{J A_m \alpha_Q}{\text{SOC}_{min} c_V F} \quad (5.1)$$

The cell volumetric flow rate Q_{cell} is a function of electrical density current J , membrane area A_m , flow factor α_Q that defines the operational range of cell volumetric flow rate (Tang et al. [70]), minimum state of charge SOC, vanadium molar concentration c_V and, finally, Faraday constant F . In Eq. (5.1) the velocity inlet U_{in} can be obtained from the number of membranes that compose the RFB n_m , the number of inlet channels n_{ch} and the cross section area of the channels A_{ch} . Besides n_{ch} and A_{ch} already reported in Tab. 5.1, the other parameters needed in Eq. (5.1) are shown in detail in Tab. 5.2. As reported by Tang et al. [70], the flow factor α_Q can be chosen in the range of $1 \div 8$. All the simulations have been performed with α_Q equal to 1. A pressure outlet condition is imposed for the outlet channels. Being the Reynolds number at inlet lower than 10, the fluid flow is assumed to be laminar.

Governing equations

The porous media model can be used in many applications including flow through packed beds, filter papers, tube banks, felts, etc. In the present CFD simulations, the presence of the porous media is not physically represented, but it has been evaluated adding two source terms to the standard momentum equations: a viscous loss term and an inertial loss term. Only in these additional terms, the effect of the porous media have been considered. In fact, the porosity has not been taken into account in the convection and diffusion terms of transport equations. This numerical procedure is well-known and the fluid velocity obtained from these modified momentum equations is named superficial velocity, i.e. the velocity that the fluid would have if it flowed through the nominal cross section area of the porous media. There is a more accurate option called physical velocity method, where the true fluid velocity inside the porous media can be evaluated and the porosity can be considered inside the convection and diffusion terms, but no significant difference has been noted between the results of the two methods.

All the simulations have been performed with the superficial velocity method and fluid cells have been divided in two domains: the first one without the porous zone, i.e. the flow in the channels, and the second one with the porous zone, i.e. the flow in the carbon felt, where the additional terms have been calculated for a homogeneous porous media. These momentum sources have been introduced as pressure gradient proportional to the superficial fluid velocity u_i^s :

$$\frac{\Delta P}{\Delta x_i} = - \left(\frac{\mu}{K} u_i^s + \frac{1}{2} C_2 \rho |u_i^s| u_i^s \right) \quad (5.2)$$

As shown in Eq. (5.2), the coefficients of both terms are a function of transport properties of the fluid, i.e. density ρ and dynamic viscosity μ , and geometrical characteristics of the porous media, i.e. permeability K and inertial loss coefficient C_2 , that have been evaluated from the Ergun equation and Blake-Kozeny equations:

$$K = \frac{d_e^2}{150} \frac{\epsilon^3}{(1 - \epsilon)^2} ; C_2 = \frac{3.5 (1 - \epsilon)}{d_e \epsilon^3} \quad (5.3)$$

The geometrical characteristics reported above in equation 3 are functions of the media porosity ϵ and the hydraulic diameter d_e of cylindrical fibers that compose the carbon felt. For all the simulations, the porosity and the diameter of fibers have been imposed, respectively, equal to 0.84 and 10^{-6} m.

It should be noted that, in the present work, the assumption of a thermal equilibrium between the porous media and the fluid flow has been considered and all the numerical simulations have been run excluding the energy equation.

As a first step, all the numerical simulations have been run considering the whole domain without the porous media to obtain an initial field flow and, in a second time, the porous zone has been enabled in the carbon felt domain. Finally, regarding the solution methods employed, a SIMPLE scheme has been used for pressure-velocity coupling, whereas a standard and second order upwind method have been imposed for the spatial discretisation of pressure and momentum.

5.2.3 Simulations of electrolyte distribution

A comparison of velocity fields, velocity distributions and pressure drop has been performed to highlight the different hydraulic performance of the four configurations. This method aims at evaluating the best configuration in terms of velocity field and pressure drop. All the results have been reported in terms of physical velocity $u = u^s \varepsilon$ (i.e. the intrinsic velocity) on the x-y plane, as defined in Eq. (5.4). The physical velocity has been calculated from the porosity ε and the superficial velocity u_i^s obtained directly from the numerical simulations:

$$u = \frac{\sqrt{u_x^{s2} + u_y^{s2}}}{\varepsilon} \quad (5.4)$$

The velocity fields are reported in Fig. 5.2 showing the difference of the fluid flow behaviour in each configuration at 50% of depth inside the carbon felt (the electrolyte enters at the bottom and exits from the top of Fig. 5.2).

As depicted in Figs. 5.4 and 5.5, the planar velocity profiles along nine lines perpendicularly to the main flow direction, see Fig. 5.6, have been calculated to investigate the velocity distribution inside the carbon felt. It should be noted that only the x-y velocity components have been considered at different depths inside the porous media (index i). Beside the velocity trends, an investigation on velocity distributions has been performed to highlight the uniformity of the velocity field inside the felt. In all the configurations, it can be observed that the velocity profiles at lines xz_{1i} and xz_{3i} are affected by the channels inlets/outlets, while in correspondence of lines xz_{2i} the velocity trend is flatter, especially for the first and last configurations. It is worth noting that the velocities are reported at different depths inside the porous media (the index i , equal to 1, 2 or 3, is referred respectively to 25%, 50%, 75% of the depth inside the felt). A non-significant influence of depth on the velocity can be observed: it means that the distribution problem is restricted to the $x - y$ plane and the investigation on planar velocity is thus justified.

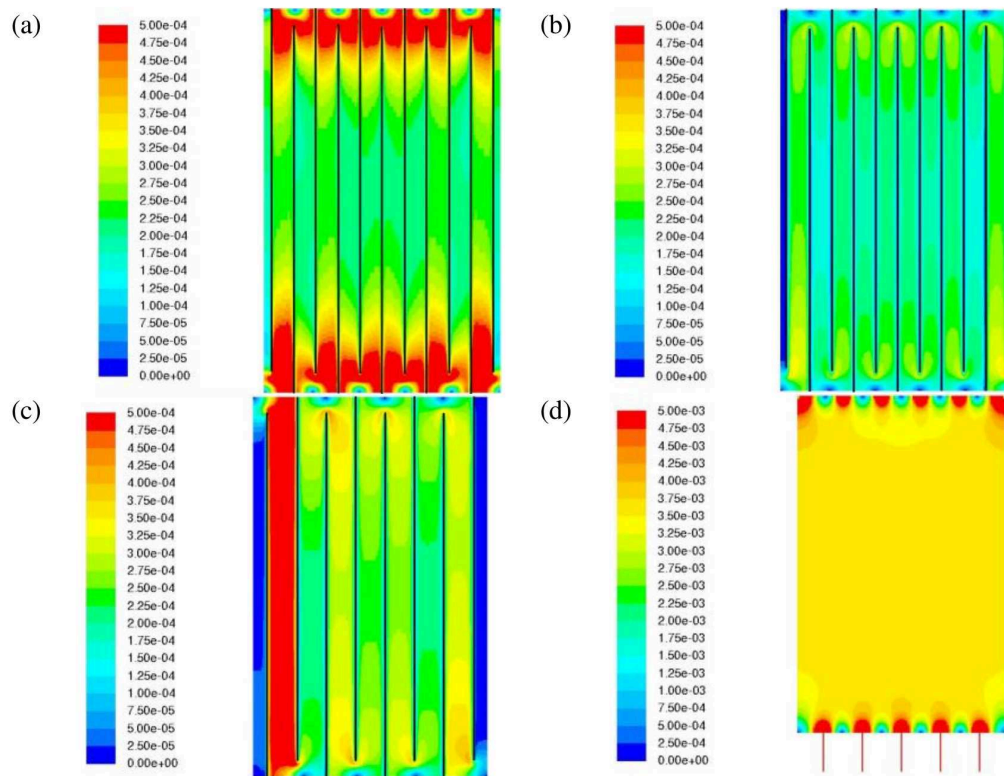


Fig. 5.2 The velocity field in [m s^{-1}] of the 5x6 1 mm h.d. (a), 5x6 2 mm h.d. (b), 4x4 2 mm h.d. (c) configurations with indirect feeding and the velocity field with direct feeding (d).

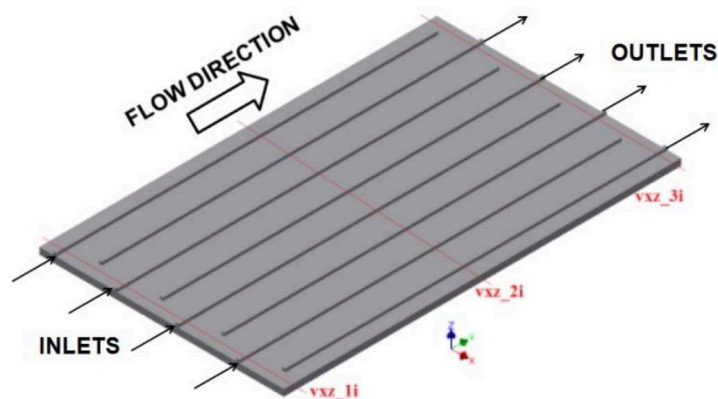


Fig. 5.3 Red lines along which the velocity profiles are calculated. The index i , equal to 1, 2 or 3, is referred to 25%, 50%, 75% of depth inside the felt (configuration 3).

Effect of hydraulic diameter

Regarding the influence of the channel hydraulic diameter on the velocity field, a comparison of velocity profiles between the first and the second configuration can be considered. As mentioned above, the volumetric flow rate is the same for all numerical simulations, hence, for case 1, the velocity and pressure drop inside the channel are higher than those for case 2, due to a lower hydraulic diameter.

In case 1, the electrolyte solution is mostly driven into the carbon felt and the velocity field is increased, as depicted in figure 2. Instead, for configuration 2, the fluid goes slower into the carbon felt creating stagnation zones below the channels and at lateral sides. The high velocity of case 1 causes a more uniform distribution of electrolyte along the lines xz_{2i} . This aspect is highlighted by the calculation of velocity distribution and it can be observed that, in the second case, the velocity values are more dispersed than those observed in the first case along the lines xz_{2i} .

Effect of number of inlet/outlet channels

Concerning the influence of the number of channels on the velocity field, a comparison of velocity trends between the second and the third configuration can be considered. Two different behaviours can be observed:

- reducing the number of channels (case 3), the velocity profiles become flatter and the fluid goes through the felt with a longer path, increasing the pressure drop as compared to case 2. Furthermore, it can be observed that the velocity values in case 3 are closer to the mean value as compared to case 2 and thus the velocity field is more uniform.
- when the number of inlet channels is equal to the number of outlet channels (case 3), an asymmetric flow takes place and a maldistribution effect occurs from left to right, as depicted in Fig. 5.4. For the third case, this effect occurs because the fluid flowing inside the first inlet channel on the left side is forced to go only through the outlet channel on the right, whereas the fluid flowing in the other inlet channels can go through its two neighbour outlet channels. For this reason, the electrolyte flow is higher on the left side as compared at the right side. This phenomenon does not occur in case 2, where the fluid in the first inlet channel can flow through the two neighbour outlet channels, providing a more uniform velocity field.

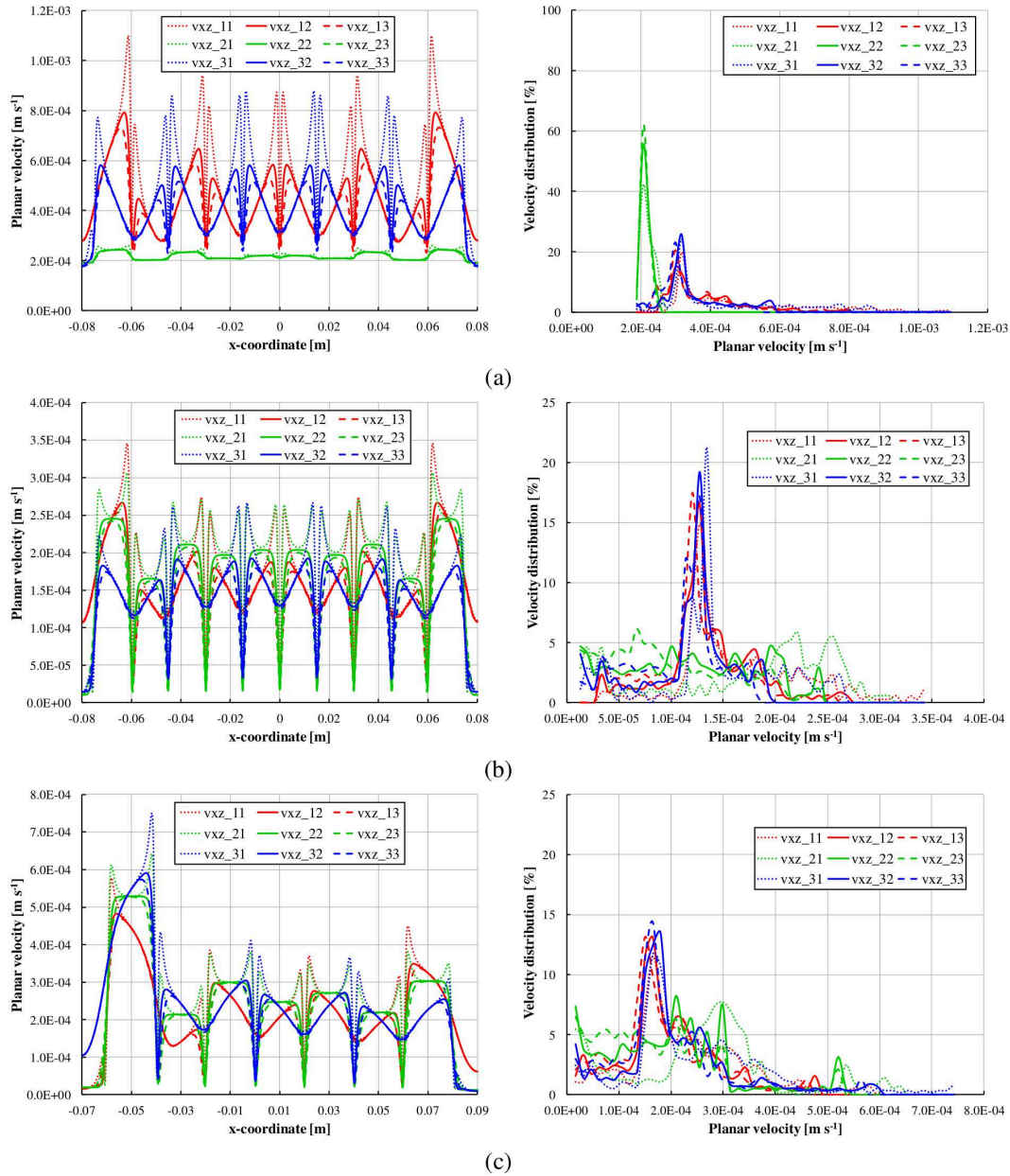


Fig. 5.4 Planar velocity profiles calculated along the lines of Fig. 5.3 (left side) and velocity distribution (right side) for the 5x6 1 mm h.d. (a), 5x6 2 mm h.d. (b) 4x4 2 mm h.d. (c) configuration with indirect feeding.

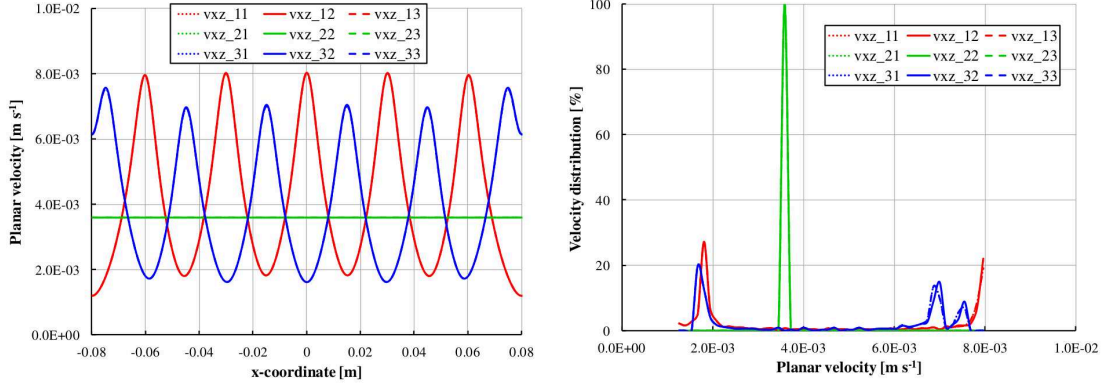


Fig. 5.5 Planar velocity profiles calculated along the lines of Fig. 5.3 (left side) and velocity distribution (right side) for the configuration with direct feeding.

Effect of feeding type

With the aim to study the influence of feeding type on the velocity field, a comparison of velocity profiles between the first and the last configuration can be considered. It is important to notice that, in the case of a direct feeding, the velocity field is higher and more uniform as compared to the first configuration, as depicted in Figs. 5.4 and 5.5. However, using the direct feeding, the pressure drop is higher as compared to the configuration with indirect feeding. Moreover, from Fig. 5.4 (a) and Fig. 5.5 along lines xz_{2i} , for both configurations, the velocities are close to the mean values and the velocity trends are similar. For this reason, it is very interesting to compare the four configurations taking into account the pressure drop. Beside the velocity trends along the different lines, the volume-weighted average of planar velocity inside the carbon felt has been calculated as reported in Eq. (5.5) to consider, at the same time, the effect of high velocity and stagnation zones.

$$U = \frac{1}{V} \int_V u \, dV \quad (5.5)$$

Pressure Drop

In the present section, the pressure drop has been calculated in order to evaluate the performance of the RFB cell in terms of pumping consumption. For the estimation of pressure drop, the area-weighted average of static pressure has been calculated at the inlet and outlet of channels for each configuration.

The relationship between the pressure drop and the velocity distribution can be observed in Tab. 5.3. Indeed, the first and the fourth configurations present the highest value of pressure

Configuration	U [m s ⁻¹]	$P_{in} - P_{out}$ [kPa]
1	3.22 10 ⁻⁴	10.61
2	1.98 10 ⁻⁴	1.40
3	2.71 10 ⁻⁴	2.30
4	3.69 10 ⁻³	210.50

Table 5.3

drop. The pressure drop in case 1 and 4 are higher, respectively, up to 7 and 150 times as compared to the configuration 2 that presents the worst distribution. The second and the third case display the lowest pressure drop but both configurations have many stagnation zones and the third one is affected by maldistribution problems. In conclusion, a good compromise would be the first solution since the velocity is high enough to avoid the presence of stagnation zones and to guarantee a velocity field almost uniform. In addition, the total pressure drop of the first case are limited as compared to the fourth case.

Streamlines

As mentioned above, to improve the performance of RFB it is fundamental to guarantee:

- a good-distribution of the electrolyte in terms of velocity, avoiding stagnation or dry zones inside the porous felt;
- low pressure drop and low pumping consumption.

For this purpose, the importance of the fluid path inside the porous media must be underlined. In fact, if the fluid has a long path inside the porous felt, the probability of electrochemical reaction occurring is higher and the RFB performance can be improved.

From this point of view, the direct feeding of electrolyte inside the carbon felt is the best configuration since the fluid is constrained to cross the whole felt as compared to the indirect feeding. As depicted in Fig. 5.6, it can be observed that, for the second and third configuration, the electrolyte solution flows from inlet to outlet channels through a very short path as compared to the first case where its path inside the felt becomes longer.

5.2.4 Remarks

In this study, four different geometrical configurations have been considered to evaluate the influence of the electrolyte solution distribution system (inlet/outlet number of channels, channels hydraulic diameter, feeding mode) on velocity field and pressure drop inside a

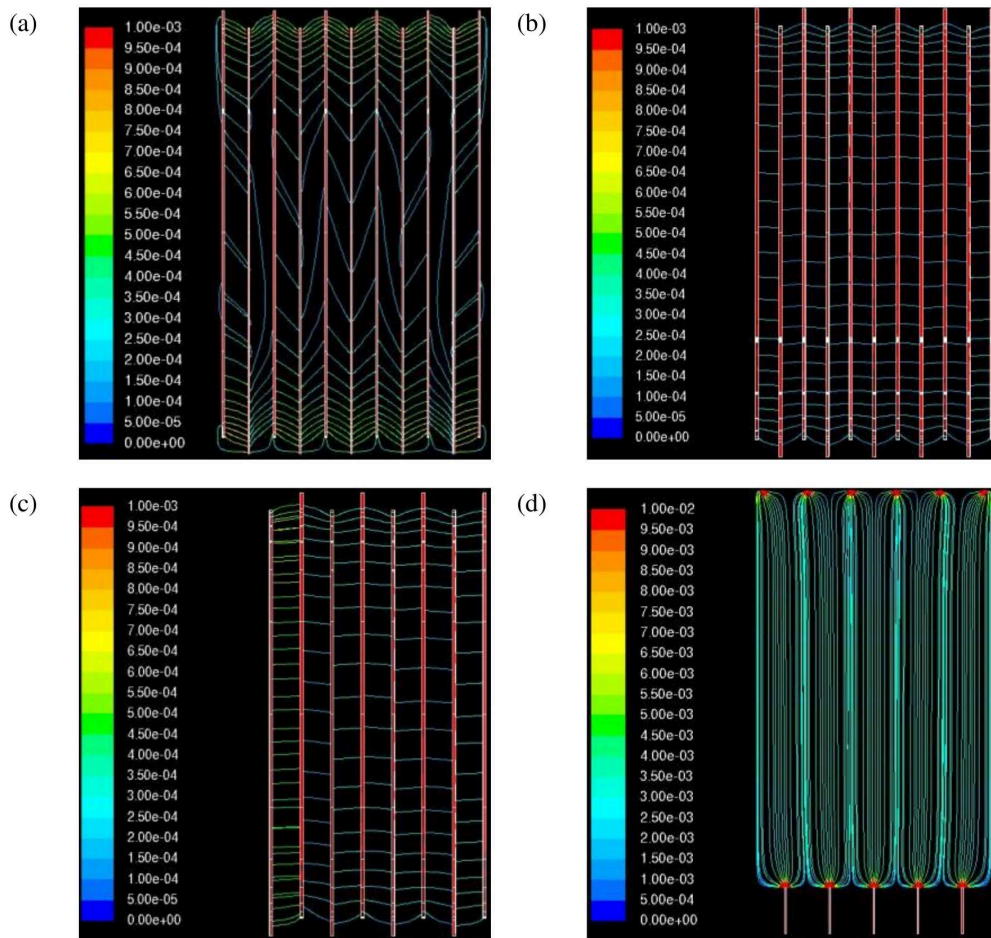


Fig. 5.6 Planar velocity streamlines in $[m s^{-1}]$ for the three configurations with indirect feeding (5x6 1 mm h.d. (a), 5x6 2 mm h.d. (b), 4x4 2 mm h.d. (c)) and for the one with direct feeding (d).

RFB cell. Different parameters have been considered to assess the RFB fluid dynamic performance: planar velocity profiles, pressure drop and velocity streamlines. The following conclusions can be drawn:

- the first and the fourth configuration present an almost uniform velocity field as compared to the second and third case where stagnation zones have been found below the channels and at the lateral sides of the carbon felt;
- a long fluid path inside the carbon felt can improve the performance of the RFB in terms of electro-chemical reactions. For this reason, the second and the third case are the worst configurations due to very short fluid path inside the porous zone;
- the fourth case with direct feeding has the highest pressure drop, up to 150 times higher than the second case. Considering both electrolyte solution distribution and pumping power, the first case results as the best choice according to the present simulations.

Chapter 6

Dispersion Dynamics in Flow Batteries ¹

6.1 Dispersion dynamics in porous media

In flow batteries, the main physical mechanism which determines the distribution of reactants in electrodes, and, in turn, battery performances, is dispersion. While the liquid electrolyte distribution is ensured by distributing channels at the macroscale, the distribution and mixing of species is guaranteed by the porous microstructure. In practice, the molecular dispersion of species in liquid is a very slow process, so that the porous microstructure is essential in order to spread the reactants (i.e. the four oxidation states of vanadium in VRFBs) all along the electrodes. The more homogeneous is reactants concentration in the electrodes, the higher the performances of the battery, since the higher number of active species would contribute to generate electric current.

Since the porous microstructure is actually responsible of mixing of species, it is intuitive to think that distribution and orientation of fibers composing the electrode are affecting species concentration and battery performances to a great extent. Nevertheless, fibers distribution and orientation in electrodes typically used for flow batteries applications are generally ignored as well as the positioning of the electrodes does not follow any specific hint. This issue will be discussed in the present chapter in order to identify the optimal configuration of porous microstructure for increasing flow batteries performances.

¹ A version of this chapter has been published in *Physics of Fluids Journal*: D. Maggiolo, F. Picano and M. Guarnieri, *Flow and dispersion in anisotropic porous media: a lattice-Boltzmann study*, Vol 28, 102001, 2016, DOI:10.1063/1.4963766

6.2 Anisotropy effects on dispersion in fibrous porous media

6.2.1 Introduction

During the last years, the interest in the utilisation of porous media composed of fibers has been considerably increased, especially for energy conversion applications [11, 71]. For instance, carbon papers and carbon felt are by now widely used as gas diffusion layers of fuel cells. But the rapid rise of decarbonated green energy demand does not limit the application of such materials to fuel cells. Flow batteries have recently been perceived as one of the most promising technologies for electro-chemical energy storage. Even though flow batteries are known since the late 1980s, it is only during recent years that the scientific community has focused on improving their performance [4, 10]. A cell of a flow battery is composed by two porous media fibrous electrodes. The inner surfaces of the porous media act as active site where electro-chemical reduction and oxidation reactions of the electrolytes occur. Both half-cells are supplied with the electrolyte solutions which are stored in external tanks and circulated by pumps to keep on the reactions. One limitation to the peak performance of flow batteries consists of the too slow electrolyte transport in the electrodes [4]. The fluid dynamic optimisation of the porous medium which provides both the electro-chemical active surfaces and the mixing volume of the chemical species is one of the main technological issues to be dealt with [10, 72].

In fact, the slow dispersion process of species in water represents a bottleneck for the peak performance of flow batteries. Specifically, the mass diffusion coefficients of the species in water, $D \approx 10^{-10} \text{ m}^2/\text{s}$, are about 10000 smaller than the water kinematic viscosity, $\nu = \mu/\rho = 10^{-6} \text{ m}^2/\text{s}$, indicating that the mass diffusion is 10000 times slower than the momentum transport. Enhancing this diffusivity can produce a dramatic increase in the cell performance. A proper designed geometry of a non-isotropic porous medium can enhance this effective mass transport while minimising the drag, thus improving and optimising the batteries performances.[10]. The present study deals with such analyses, by means of a Lattice Boltzmann model and a Lagrangian Particle Tracking algorithm.

Even if the influence of medium porosity on the flow drag has been largely studied [73, 74], the impact of its microscopic design on the combined mixing/transport mechanisms and drag is still not well assessed [8, 75]. In fact, even though the anomalous (i.e. non-Fickian) behaviour of dispersion in porous media has been widely investigated [76–78], it is not clear to what extent the micro-structure of the medium can impact macroscopic dispersion phenomena. Local heterogeneities at various scales have been considered capable

of generating such anomalous behaviour [79–81]. Berkowitz and Sher [80] claimed that a wide distribution of delay times limiting the transport in porous media results in non-Fickian dispersion which cannot be represented by an equation including a time-dependent dispersion coefficient. Instead, the authors highlighted that all the time evolution of motion must be taken into account, and that the macroscopic advection-dispersion equation (ADE) must be non-local in time.

Whitaker [77] identified different fluid-dynamic variables responsible for the dispersion by means of the Volume Averaging technique. This analysis revealed the presence of different terms in the averaged ADE which act as sources of dispersion and convection. Nevertheless, the volume averaging technique is not sufficient to predict the dispersion behaviour in a general way, since the evaluation of the effective dispersion tensor is limited by some constraints. In fact, in practical applications the value of the effective dispersion tensor may be significantly different than expected, since it depends on the unconditioned statistics of hydraulic permeabilities of the porous medium [82].

Several authors agree that dispersion should tend to the standard Fickian dispersion at a certain temporal or length scale for which all the hypothesis of the central limit theorem are satisfied, i.e. when the particle motion is no more correlated [83, 84]. Such transient anomalous behaviour has been recently recognised in a variety of physical-chemical and socio-economical systems, which can also present non-Gaussian yet Fickian dispersion behaviours [84]. However, the aforementioned time or length scales strongly depend on the medium structure and, thus, they are not easy to determine a priori.

More recently, other causes have been identified as responsible of the anomalous dispersion, such as the presence of three-dimensional vortices [85], particle jumps [86] and different mechanisms of dispersion acting on subgroups of particles [87]. Castiglione et al. [87] suggested that two mechanisms of dispersion (i.e. a weak anomalous dispersion and a strong anomalous dispersion associated to ballistic motion) can give rise to transient anomalous dispersion in several systems. The authors underlined that even though it is not particularly difficult to build up probabilistic models exhibiting anomalous dispersion, understanding anomalous dispersion in nontrivial systems, such as porous media, is much more difficult [87].

A review of the literature about anomalous dispersion revealed that this behaviour is really difficult to predict. Furthermore, to the best of these authors' knowledge, a good understanding of how porous medium micro-structure can enhance macroscopic transport is still lacking, especially for fibrous porous media. Many works on such media have been focused on the geometrical properties which can possibly affect standard Fickian dispersion and reaction, rather than on the intrinsic behaviour of dispersion phenomena [88, 89].

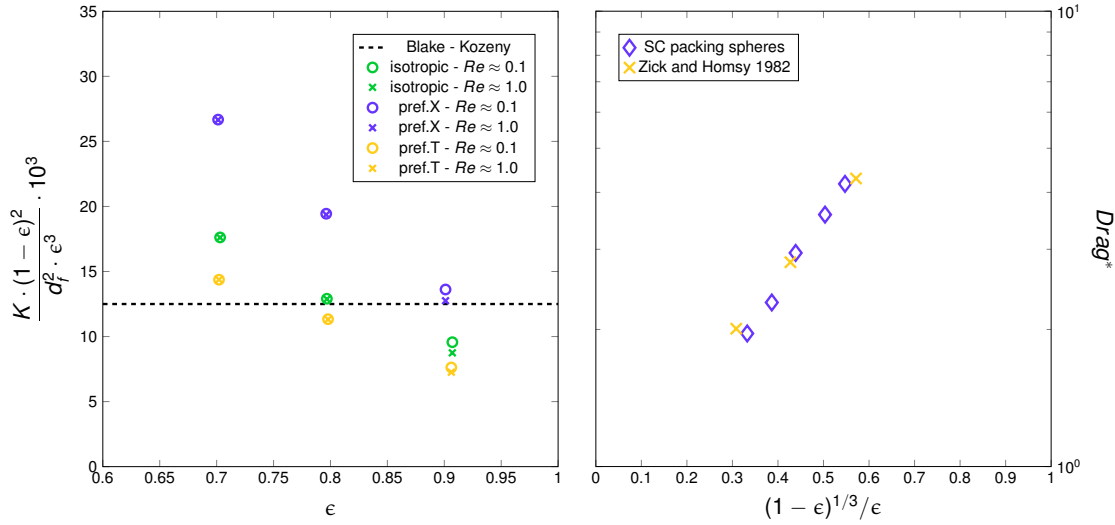


Fig. 6.1 Left Panel: dimensionless permeability values for different cases of porosity ϵ and orientation. Results gather around the predicted value of the Blake-Kozeny equation, as expected. It should be pointed out that the permeability values diminish as the porosity increases, a trend already observed in Whitaker [73]. Right Panel: drag coefficients $Drag^* = 2r_s^2/(9K)1/(1 - \epsilon)$ from numerical simulations of flows through single packed-bed of spheres of radius r_s compared with results of Zick and Homsby [90].

In order to clarify this issue, this study presents results of several simulations at different preferential orientation of fibers, porosity and Reynolds number. A Lattice-Boltzmann-based model coupled with a Lagrangian particle tracking algorithm has been used. The aim of the present study is to clarify how the nematic properties of the porous medium affects the mass and momentum transport mechanisms in order to design optimal porous media with low drag and high effective mass diffusion. The minimisation of drag reduces the pump power demand, while the maximisation of the mixing improves the homogeneity of reacting species all along the porous medium, both effects enhancing the performance of flow batteries. It will be shown, that porous media constituted by fibers preferentially oriented along the flow direction exhibit smaller drag and higher effective diffusion.

6.2.2 Methodology

The present model is a further development of the Lattice-Boltzmann model already validated and used in Maggiolo et al. [91]. The model has been further validated by evaluating the permeability values obtained with different values of porosity, fiber orientation and Reynolds number and the drag exerted by the flow on single packed-beds of spheres. The permeability values K have been obtained by means of the Darcy equation which relates the velocity with the pressure gradient:

$$K = U \varepsilon \mu \left(\frac{\Delta P}{L} \right)^{-1}, \quad (6.1)$$

where the pressure gradient $\Delta P/L$ corresponds to the applied body force, $U = [1/(\varepsilon V)] \int_V u_x dV$ is the bulk intrinsic velocity of the generic cubic domain V along the streamwise direction x , μ is the dynamic viscosity, and ε is the porosity. Figure 6.1 shows values of dimensionless permeability against porosity on the left panel, and the values of drag coefficients of the packed bed of spheres compared with the values of Zick and Homsy [90] on the right panel. Results of these simulations are considered proof of the validity of the model. Dimensionless permeability values $K^* = K/d_f^2$ cluster around the permeability value of the Blake-Kozeny equation [73]:

$$K^* \frac{(1 - \varepsilon)^2}{\varepsilon^3} = \frac{1}{80}. \quad (6.2)$$

Eq. (6.2) has been derived for a medium composed of cylindrical fibers, for which the equivalent diameter (i.e. six times the ratio between the volume of the fiber and its surface) equals three halves of the fiber diameter d_f [82]. Fig. 6.1 also shows that the higher the porosity, the lower the dimensionless permeability and the resulting pressure drop. The fiber Reynolds number has been determined as $Re_f = U d_f / \nu$, where ν is the kinematic viscosity. Preliminary results of dispersion in these media show that the main dispersion features do not depend on the fiber Reynolds number, in the range $Re_f = 0.1 \div 1.0$, and on the porosity, in the range $\varepsilon = 0.7 \div 0.9$, see the end of Section 6.2.3. Conversely, results instead show that dispersion depends on the orientation of the fibers. In light of this, further simulations have been carried out in order to characterise the effective dispersion induced by the porous medium micro-structure with high porosity values; the fiber Reynolds number has been fixed in the order of $Re_f = 10^{-1}$ and the porosity at $\varepsilon = 0.9$, in order to minimise drag.

A triperiodic box has been considered, see Fig. 6.2. The porous medium is composed of 50 fibers with length $\ell_f \approx 160\sqrt{3}$ computational cells, uniformly random distributed throughout the domain. The side of the periodic box is discretised by $L = 160$ Lattice-Boltzmann cells, while the fiber diameter d_f corresponds to 6 cells. Three reference cases of fiber orientation have been investigated: an isotropic medium, an anisotropic medium preferentially oriented along the streamwise direction x and an anisotropic medium preferentially oriented along the transverse directions y and z . Seven isotropic, nine preferentially streamwise-oriented and eight preferentially transverse-oriented media have been considered in order to get a statistically significant samples, making a total of 24 simulations. The flow is driven along the x direction by a mean pressure gradient $(\Delta P/L)$ which implies a fiber Reynolds number in the order $Re_f = 10^{-1}$.

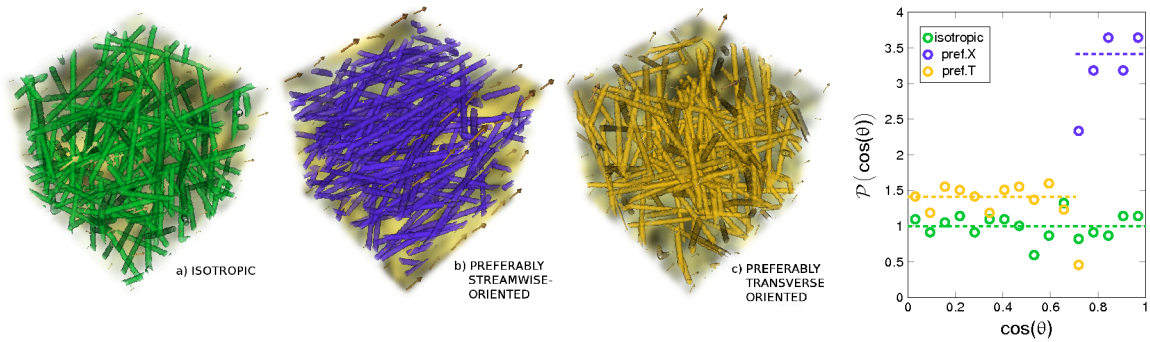


Fig. 6.2 Left Panels: Triperiodic cubic domains generated by numerical modelling where particles are randomly injected and advected by the steady flow field in the porous medium. Three main different orientations have been considered: a) an isotropic medium; b) a medium preferentially oriented along the streamwise direction x ; c) a medium preferably oriented along the transverse directions y and z . The medium is considered preferentially oriented along the streamwise or transverse direction when all the angles θ formed by the axes of the fibers and the x axis are lower or higher than $\pi/4$, respectively. Right Panel: probability distribution functions of $\cos(\theta)$ for different fibrous media.

The mass transport properties have been evaluated following non-Brownian tracer particles injected in the fluid. The LBM stationary flow field has been used as input of the Lagrangian Particle tracking algorithm, and Lagrangian statistics of five thousand particles for each medium have been analysed in order to extract the effective diffusion coefficients in the porous media. Particles have been randomly injected in the fluid phase and their trajectories have been stored in time. All the observables shown in the following analysis have been normalised using the bulk intrinsic velocity U and the fiber diameter d_f .

In the whole text, the statistical observables (e.g. permeability K^* , effective viscosity ν_{eff}^* , Mean Square Displacement MSD^*) are calculated as mean values among all the cases belonging to one of the three main cases of fiber orientation, which are statistically equivalent, i.e. either isotropic, or preferentially streamwise-oriented, or preferentially transverse-oriented. This approach allows to determine the statistical confidence on the data.

6.2.3 Simulations of dispersion

The bulk resistance to the flow induced by fibrous media with different typical fiber orientation is characterised by the permeability K^* described in eq. (6.2). At fixed flow rate, a higher value of permeability corresponds to a lower pressure drop, which is a desirable condition in RFBs because it allows to reduce the pump power needed to flow the electrolyte through the electrodes. The left panel of Fig. 6.3 shows the values of K^* obtained in the three cases

Table 6.1 Fiber Reynolds numbers and dimensionless root mean square velocities along the streamwise, $\langle u_x'^2 \rangle / U^2$, and transverse, $\langle u_t'^2 \rangle / U^2$, directions, for different fiber orientations.

orientation	Re_f	$\langle u_x'^2 \rangle / U^2$	$\langle u_t'^2 \rangle / U^2$
isotropic	0.12739	0.50348	0.10369
pref.X	0.17146	0.41988	0.06058
pref.T	0.10911	0.49803	0.13800

differing for the typical fiber orientation that are parametrised by the mean value of $\cos(\theta)$, with θ the angles between the fibers and the x axis. The medium constituted by preferentially oriented fibers along the streamwise direction presents the highest value of permeability, while that with fibers preferentially transverse to the flow shows the lowest permeability. This behaviour is not surprising considering that the former case presents the lowest projected area of the fibers on the cross-stream plane, while the latter the highest. In particular, it should be noted that media with fibers preferentially aligned along the flow reduce the overall drag by around 35% with respect to isotropic fibrous media.

For later convenience, the same behaviour is quantified in terms of an effective diffusion coefficient of the momentum transport. An effective (kinematic) viscosity ν_{eff} has been defined considering the ratio between driving force $(\Delta P/L)(1/\rho)$ and an effective viscous force given by U/d_f^2 . In dimensionless form, the effective viscosity $\nu_{eff}^* = \nu_{eff}/(Ud_f)$ reads:

$$\nu_{eff}^* = \left(\frac{\Delta P}{L} \frac{1}{\rho} \right) \frac{d_f}{U^2}. \quad (6.3)$$

Being the effective viscosity strictly related to the permeability, it conveys similar information, however it will be useful to determine the dispersion efficiency, dimensionally homogeneous to the effective diffusion coefficient. Although the general behaviours of ν_{eff}^* and $1/K^*$ are equivalent, they are not proportional because the fiber Reynolds number Re_f slightly differs from the cases with constant driving force (Tab. 6.1).

Along with the minimisation of the drag, in the case of flow batteries it is crucial to enhance the mixing of the electrolytes in the porous medium constituting the electro-chemical active regions. To this purpose, it is important to characterise the dispersion properties of tracer particles distributed in the flow. The analysis has been restricted to non-Brownian particles whose trajectories coincide with those of fluid particles. As previously noted, the typical diffusion coefficient of electrolytes is quite small ($D \sim 10^{-10} m^2/s^{-1}$) and usually negligible on the scale of the porous electrode. The main dispersion properties have been evaluated using the (dimensionless) Mean Square Displacements in the streamwise (MSD_x^*)

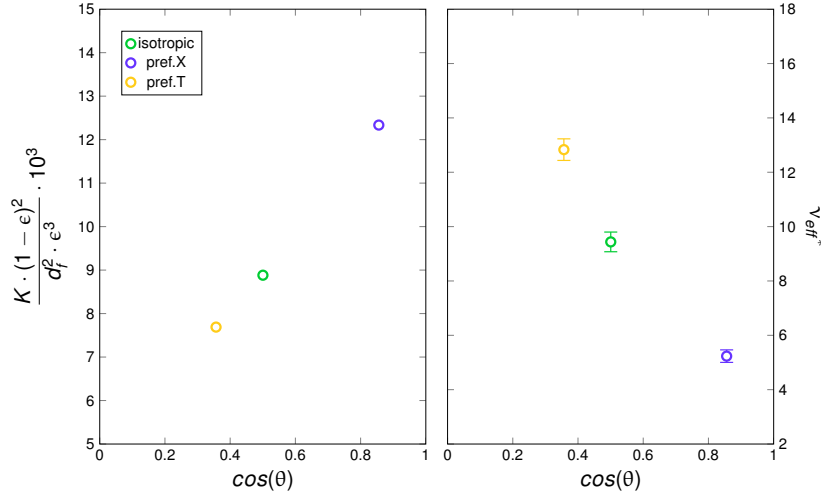


Fig. 6.3 Dimensionless permeability (left panel) and effective viscosity (i.e. ν_{eff}^* , right panel), for the three main fiber orientations, plotted against the mean value of $\cos(\theta)$. The effective viscosity is considerably reduced in the media preferentially oriented along the streamwise direction, indicating a significant reduction of the drag exerted on the medium, and, in turn, of the pressure drop.

and transverse (MSD_t^*) directions evaluated from the statistics of particle displacements dx, dy, dz as follows:

$$\begin{aligned}
 \text{streamwise : } MSD_x^*(t^*) &= \langle dx'^2 \rangle / d_f^2 \\
 \text{transverse : } MSD_t^*(t^*) &= (\langle dy'^2 \rangle + \langle dz'^2 \rangle) / (2d_f^2) ,
 \end{aligned} \tag{6.4}$$

where $t^* = tU/d_f$ is the characteristic time, $dx(t^*)$ is the displacement along a generic direction x , $dx'(t^*) = dx - \langle dx \rangle$ is the displacement fluctuation, and $\langle \cdot \rangle$ indicates the ensemble averaging operator. Figure 6.5 shows the values of the mean square displacement MSD^* along the streamwise and transverse directions as a function of the characteristic time t^* . The MSD^* is initially proportional to t^{*2} , corresponding to a straight line with slope 2 in the log-log plot. This is expected for small characteristic times when the particle motions are strongly correlated with ballistic trajectories. After a characteristic time $t^* \approx 10$, the behaviour of the MSD^* changes as $MSD^* \propto t^{*\alpha}$, with $\alpha \approx 1.50$ and $\alpha \approx 1.25$ along the streamwise and transverse directions, respectively. These exponents correspond to a superdiffusive dispersion behaviour. The superdiffusive dispersion process denotes a fast anomalous dispersion which has been found in biological and other specific physical systems [84]. For longer characteristic times $t^* \gtrsim 100$ the dispersion behaviour changes again. The MSD_x^* becomes proportional to $\approx t^{*1.3}$ along the streamwise direction, i.e. the

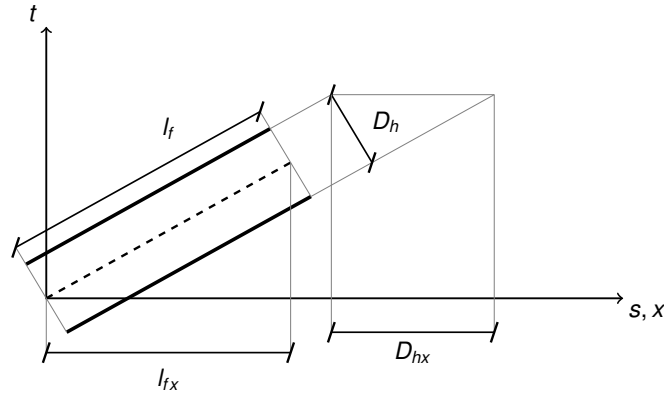


Fig. 6.4 Hydraulic diameter D_h and length l_f of a “tilted” pore and their projections along the streamwise direction D_{hx} and l_{fx} .

dispersion is still superdiffusive but with a different exponent, while it approaches a standard Fickian dispersion with the MSD_t^* proportional to the time t^* along the transverse direction. These different behaviours identifies three main regimes: (i) a typical ballistic dispersion for short times, (ii) a superdiffusive dispersion for intermediate times, and (iii) a third regime for long times which is Fickian in the transverse direction, while still superdiffusive for the streamwise direction. The hydraulic diameter $D_h = 4\varepsilon V/S \approx 9d_f$ has been related to the mean intercept length in porous media [92]. More to the point, it indicates the mean width of the pores formed by the porous micro-structure. In order to take into account the effect of the fibers orientation, one should consider the main pores width and length along the streamwise x direction, that is, $D_{hx} = D_h/\sqrt{1 - \cos(\theta)^2}$ and $l_{fx} = l_f \cos(\theta)$, see Fig 6.4. Following this approach the mean half-width of the pores (i.e. the main radius of the pores) and their mean length result $R_{hx} = 4.8d_f, 5.2d_f, 8.8d_f$ and $l_{fx} = 15d_f, 23d_f, 40d_f$ for the transverse oriented, isotropic and streamwise oriented medium, respectively. In the light of this, the three different behaviours can be interpreted with typical time scales, estimated considering the bulk velocity and the porous radius $\approx R_{hx}$ and the porous length $\approx l_{fx}$ induced by the aspect ratio of the fibers. When $t^* < R_{hx}/d_f$ particles are travelling inside a pore width, possibly rounding one fiber, while, when $t^* \gg l_{fx}/d_f$ particles have crossed the whole pore length and their dispersion becomes Fickian, on the average. Conversely, when $R_{hx}/d_f < t^* \lesssim l_{fx}/d_f$, particles are travelling along the anisotropic pores and their trajectories tend to follow the pores axes, resulting in an enhancement of the dispersion in the medium.

It should be noted that different exponents of the time behaviour in MSD^* have been reported in the literature, considering different porous media, see e.g. [93]. The present data, showing long-time superdiffusive streamwise dispersion, are consistent with the recent

findings of Kang et al. [8] who analysed a numerical simulation of a real porous geometry reconstructed by a micro-tomography. Concerning the difference among the three cases considered which differ for the fiber orientation, a very similar trend for the dispersion in the streamwise direction for all cases has been noted. However for the long time behaviour, the transition from the superdiffusive dispersion with $\alpha \approx 1.5$ to that with $\alpha \approx 1.3$ occurs at shorter times for the isotropic and the preferentially transverse cases so the particles of the preferentially streamwise aligned medium show eventually a slightly larger MSD_x^* for high t^* .

Concerning the differences found in the transverse dispersion, in the ballistic short-time behaviour, the transverse medium shows higher rate of dispersion, followed by the isotropic case and then the streamwise oriented one. In this limit, $MSD_t^* \propto \langle u_t'^2 \rangle / U^2 t^{*2}$, so that t^{*2} ballistic dispersion is imposed by the fluid cross-stream velocity fluctuation levels which are maximal in the transverse case (Tab. 6.1). After the ballistic motion, all the cases show a similar time scale with transition to the super-diffusive behaviour. However, the streamwise oriented medium shows a slightly longer transition time. A similar trend is shown for the second transition from the super-diffusive to the regular Fickian behaviour, where again the streamwise oriented medium shows the longest transition time. The longer permanence time of this case in the ballistic and super-diffusive behaviours allows a recovery of the slower dispersion shown for small t^* . For this reason, all cases show a similar level of MSD_t^* for long time, when they exhibit a Fickian diffusion in the transverse direction. The porous structures created by the streamwise oriented direction, which is possibly able to correlate the motion of a fraction of particles for a much longer time, provides a possible explanation.

To this purpose, it is important to analyse the correlations of the particle motion in order to understand the different behaviours. The dimensionless autocorrelation functions $c_v'^*$ along the streamwise and transverse directions have been determined as follows:

$$\begin{aligned} \text{streamwise : } c_{vx}'^*(t^*) &= \frac{\langle v_x'(t^*) v_x'(0) \rangle}{\langle v_x'(0)^2 \rangle} \\ \text{transverse : } c_{vt}'^*(t^*) &= \frac{1}{2} \left(\frac{\langle v_y'(t^*) v_y'(0) \rangle}{\langle v_y'(0)^2 \rangle} + \frac{\langle v_z'(t^*) v_z'(0) \rangle}{\langle v_z'(0)^2 \rangle} \right) \end{aligned} \quad (6.5)$$

where v_i and $v_i' = v_i - \langle v_i \rangle$ are the particle absolute and fluctuation velocities along the direction $i = x, y, z$.

Results of dimensionless autocorrelation functions $c_v'^*$ for different fiber orientations are plotted against the characteristic time t^* in Fig. 6.6. The velocity autocorrelation $c_{vx}'^*$ along the streamwise direction is significantly higher than the transverse one for all the considered

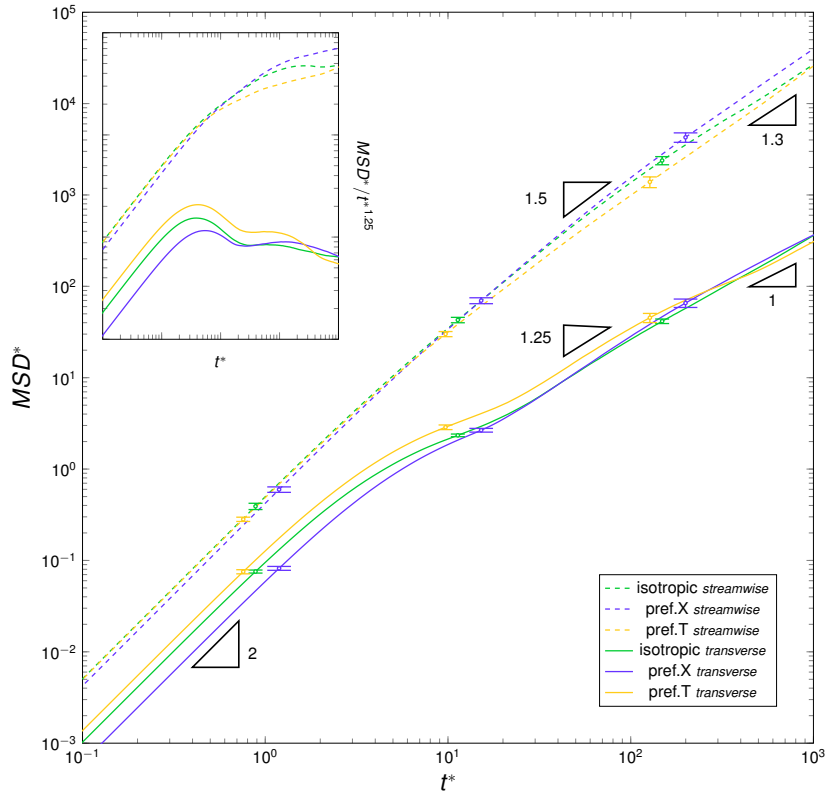


Fig. 6.5 Dimensionless Mean Square Displacement against dimensionless time t^* along the streamwise (MSD_x^* , dashed lines) and transverse (MSD_t^* , solid lines) directions. Three main regimes can be distinguished: 1) a ballistic dispersion for short times; 2) a superdiffusive dispersion for intermediate times; 3) a still superdiffusive dispersion along the streamwise direction and a Fickian standard dispersion along the transverse direction, i.e. $MSD_t^* \propto t$, for long times. The difference in the three main regimes is highlighted in the inset which shows the ratio $MSD^*/t^{*1.25}$ approaching a constant value in the second and third regime along the transverse and streamwise direction, respectively.

cases. Moreover, for long times, the streamwise velocity autocorrelation slowly decays, while that for the transverse direction decorrelates for $t^* \approx 100 \gg l_{f,x}/d_f$. This behaviour reflects the anisotropy induced by the mean flow driven by the mean pressure gradient. The correlation of the streamwise motion for longer times is attributed to two typical particle trajectories, the former to the particle that travels near a stagnation point, the latter to particles which flow in the bulk of some almost streamwise aligned long pores. In both cases the particles tend to reside for long time in the same state characterised by a similar velocity. Before discussing the effect of the preferential fiber alignment, it is interesting to note how different is the autocorrelation of the transverse velocity. It shows a faster decorrelation and shows a negative minimum around $t^* \sim 5 \div 9$, which approximately corresponds to the mean half-width of pores in the medium $R_{h,x}$. This minimum indicates that after that time, the particle motion tend to reverse in the transverse direction and this can be interpreted as an effect induced by the particles which are rounding the fibers. Actually after the minimum, the autocorrelation shows a relative maximum before decorrelating, which can be interpreted as the effect of a successive fiber encountered during the motion. Concerning the effect of the preferential fiber orientation, the autocorrelation of the preferentially streamwise oriented fibers is in general higher for longer times for both the streamwise and transverse motions. In some sense, it appears that the pores created by the almost streamwise fiber are able to be followed by a part of particles for longer times. This induces a higher correlation for both velocities, since the pores are not completely streamwise oriented along the weakly tilted fibers. This results in longer characteristic times which divides the typical dispersion behaviours observed in the MSD^* . As it is well known, the mean square displacement is actually determined by the autocorrelation function as,

$$MSD^* = 2 \langle v'(0)^2 \rangle t^* \int_0^{t^*} \left(1 - \frac{s}{t^*}\right) c_v'^*(s) ds. \quad (6.6)$$

From eq.(6.6), the ballistic behaviour $MSD^* \propto t^{*2}$ can be obtained for $c_v'^* = 1$, while for high t^* and $c_v'^* = 0$ the dispersion becomes regular and Brownian, namely $MSD^* \propto t^*$. If instead for long times it is $c_v'^* \propto t^{*\beta}$, the mean square displacement shows an anomalous diffusion, $MSD^* \propto t^{*\alpha}$ with $\alpha = 2 + \beta$. Hence, the different dynamics noted in the MSD^* analysis reflects in different behaviours of the autocorrelation. It has been previously noticed how the preferentially streamwise oriented medium shows longer characteristic times for the transition among the different dynamics and that this reflects in higher dispersion at longer times. Moreover, the long time behaviour observed for the mean square displacement is consistent with the results of the autocorrelation where a decorrelation is found for the

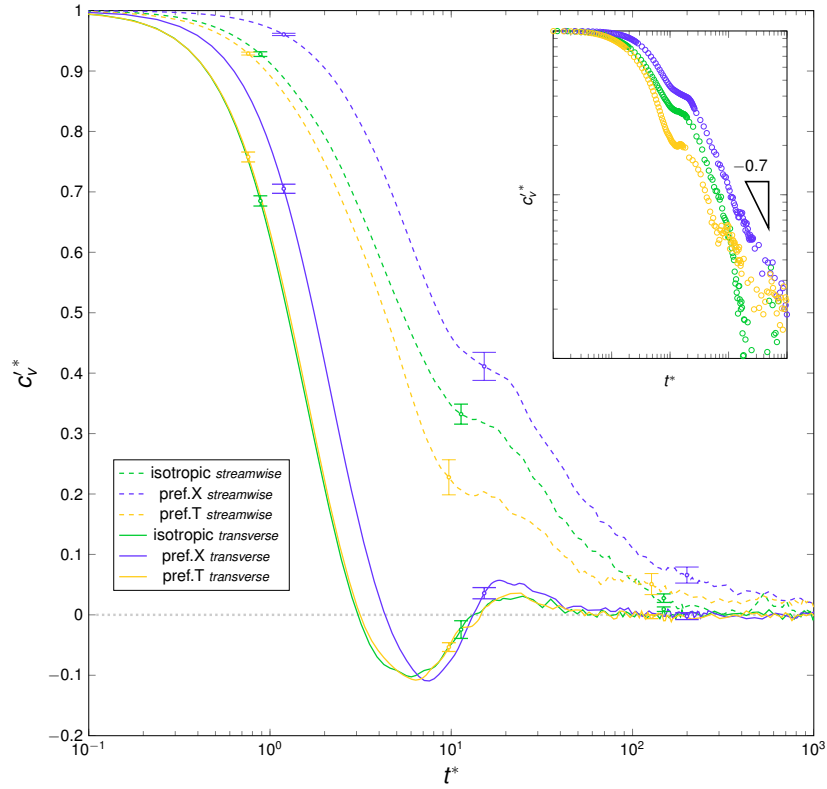


Fig. 6.6 Dimensionless velocity autocorrelation $c_v'^*$ against dimensionless time t^* along the streamwise ($c_{v_x}'^*$, dashed lines) and transverse ($c_{v_t}'^*$, solid lines) directions. The autocorrelation approaches zero along the transverse direction for long characteristic times, i.e. in the third regime observed. The figure highlights that the streamwise-oriented medium presents higher velocity autocorrelations not only along the streamwise direction (as expected since fibers are aligned with the main flow), but also in the transverse direction. The inset represents velocity autocorrelations along the streamwise direction in log-log plot: it can be observed that $c_{v_x}'^*$ decreases proportionally to $t^{*-0.7}$ towards the end, which in turn corresponds to an increasing of the $MSD_x^* \propto t^{*1.3}$.

transverse velocity and a slow decay with $\beta \simeq -0.7$ is observed for the streamwise direction, as shown in Fig. 6.6.

To better highlight the origin of the different anomalous dispersion behaviours, the Probability Distribution Functions (PDF) of the particle displacements along the streamwise and transverse directions are shown in Figures 6.7 and 6.8. The displacements are relative to the mean position and normalised with the square root of the variance (MSD^*) in order to highlight the difference with the corresponding Gaussian distribution. At $t^* = 0$ and for small t^* the PDF of the displacements correspond to that of the flow field u_x , since the particle motion is highly correlated with their initial conditions. Focusing on the streamwise behaviour first, see Fig. 6.7 panel a), the displacements and the underlying velocity field is

strongly non-Gaussian. The mean flow direction induces a highly asymmetric PDF with a steep positive tail. In particular the streamwise velocity field is characterised by low-velocity regions (near stagnation points) and by high-velocity preferential paths which correspond to long pores mainly oriented along the streamwise direction. This behaviour induces a great asymmetry of the displacement at small times with a PDF which is left-truncated and reveals a significant part of particles travelling at speed far higher than the average (right tail of the PDF). Since at $t^* \approx 10$ the streamwise motion is still correlated (Fig. 6.6), the PDF is very similar to the initial one. After a characteristic time $t^* \approx 100$, which identifies the end of the ballistic motion with a power-law decaying correlation, the shape of the PDF starts to approach the Gaussian shape, see panels *c* and *d* of Fig. 6.7, with still a positive tail slightly steeper than a Gaussian. No significant differences emerge from PDFs of different media. The origin of the streamwise anomalous diffusion appears related to the skewed non-Gaussian intermittent flow velocity field induced by the fibrous microstructure. However, the different fiber preferential alignment appears to alter the typical correlation time scales of the flow and not the single-point statistical behaviour.

The PDF of transverse particle displacements is represented in Fig. 6.8. The transverse flow velocity field PDF corresponds to the PDF at $t^* = 0$, panel a), and appears non-Gaussian, but symmetric because of the isotropy of motions in the cross-stream plane. The fibrous microstructure induces very steep tails in the PDF at $t^* = 0$ denoting that the pores are able to transport particles at longer transverse distance with respect to a corresponding Gaussian process. At $t^* \simeq 10$, being the motion in the transverse direction uncorrelated, the displacements PDF differs from the initial one and in particular results more Gaussian. At $t^* \simeq 100$ and $t^* \simeq 500$ is even more Gaussian.

Hence concluding, the dispersion dynamics in fibrous media with different preferential alignment of the fibers show a long-lasting superdiffusive behaviour of the streamwise dispersion which appears induced by the highly non-Gaussian velocity field. On the contrary, in the transverse directions, a long-time regular diffusion has been observed. On the shorter time-scales, the dispersions induced by fibrous media are superdiffusive for both directions. In these regime we found the most important difference among the cases differing for the fiber preferential alignment. The typical time-scale at which these highly dispersive behaviours end is longer when the fibers are preferentially streamwise oriented. This results in a overall mean square displacement for longer times (MSD^*) which is higher or similar to when the medium is constituted by isotropic oriented fibers. In other words, aligning the fibers preferentially along the streamwise direction slightly increases the long-time dispersion. To give an overall measure of the long time dispersion, the dimensionless dispersion coefficients D^* have been computed by fitting the dimensionless mean square displacements

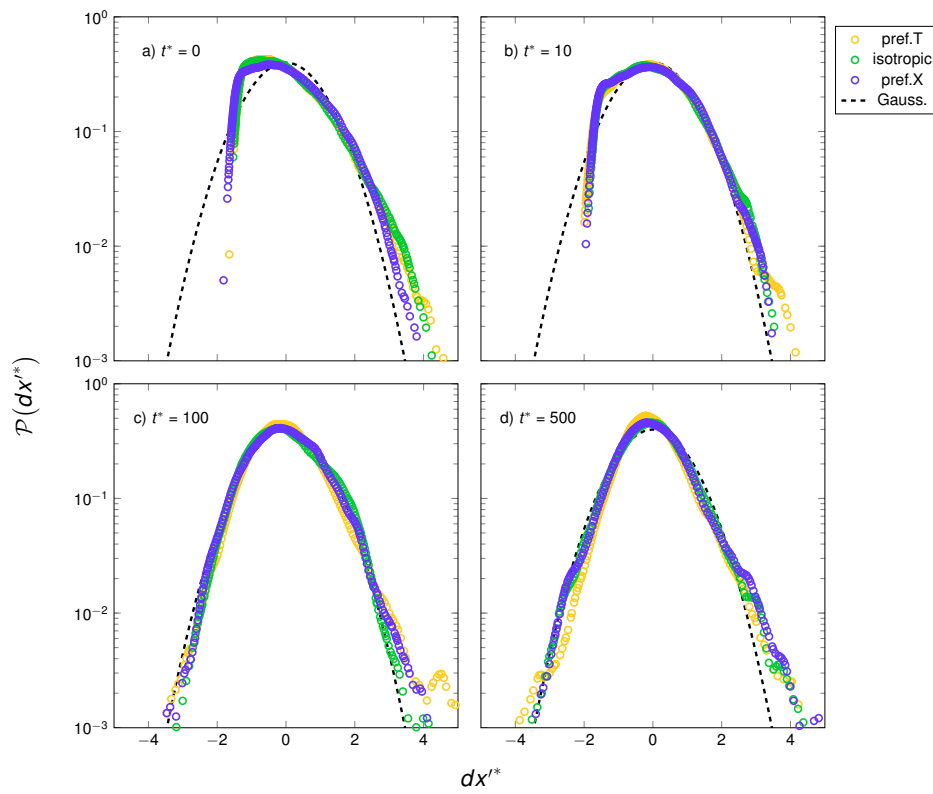


Fig. 6.7 Probability distribution functions (PDF) of dimensionless displacement fluctuations, $dx'^* = (dx - \langle dx \rangle) / \sigma(dx)$ (where $\sigma(dx)$ is the variance), along the streamwise direction, for different fiber orientations. (a) PDF at $t^* = 0$; (b) PDF at $t^* = 10$; (c) PDF at $t^* = 100$; (d) PDF at $t^* = 500$.

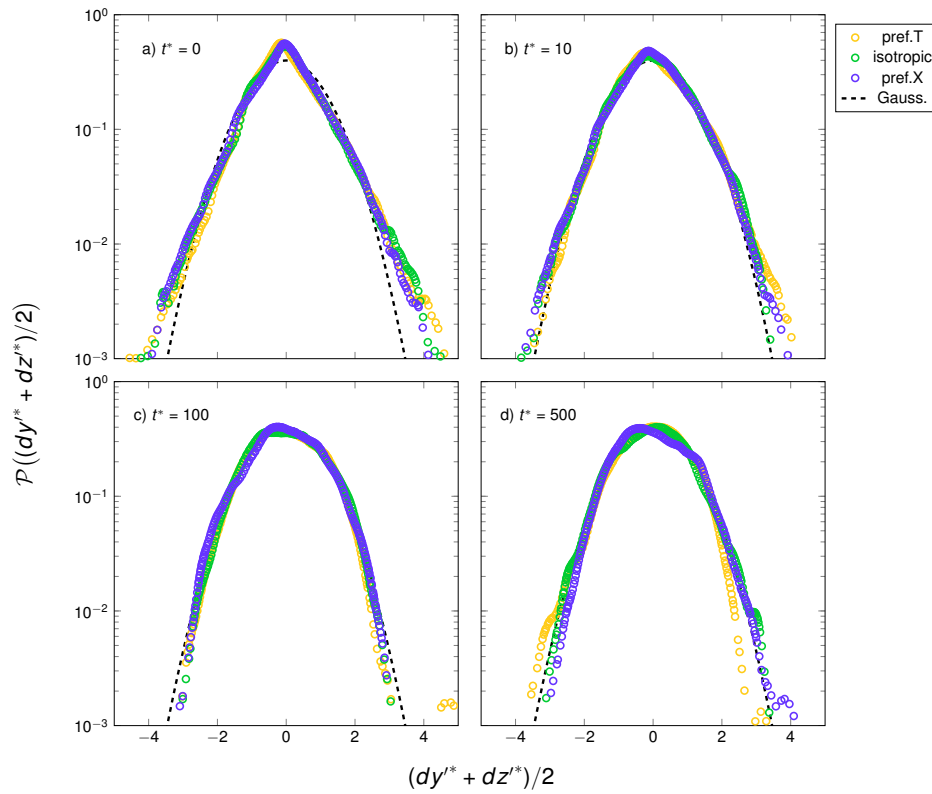


Fig. 6.8 Probability distribution functions of dimensionless displacement fluctuations, $(dy^* + dz^*)/2 = ((dy - \langle dy \rangle)/\sigma(dy) + (dz - \langle dz \rangle)/\sigma(dz))/2$ (where σ is the variance), along the transverse direction, for different fiber orientations. (a) PDF at $t^* = 0$; (b) PDF at $t^* = 10$; (c) PDF at $t^* = 100$; (d) PDF at $t^* = 500$.

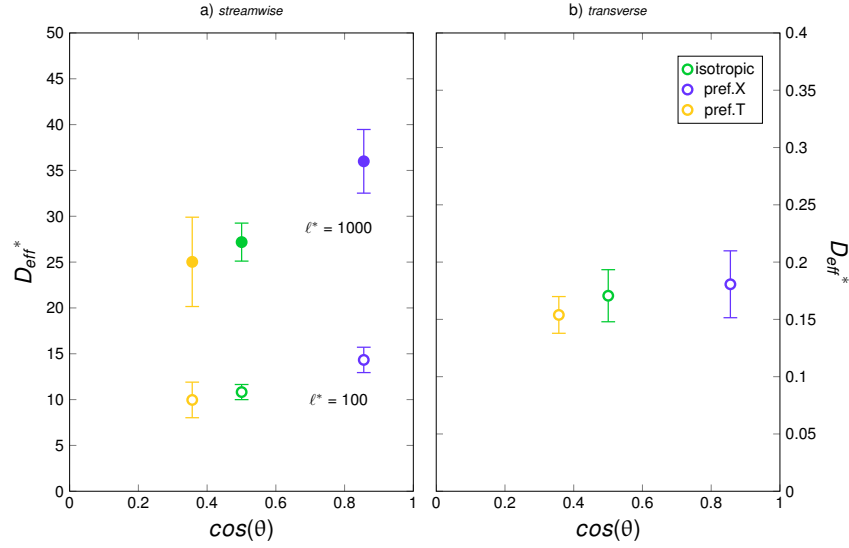


Fig. 6.9 Dimensionless equivalent effective dispersion coefficients D_{eff}^* plotted against the mean value of $\cos(\theta)$, for different cases of fibers orientation, along the streamwise (left panel) and transverse (right panel) direction. In left panel void marks indicate a characteristic displacement length $\ell^* = \ell/d_f = 100$, whereas filled ones indicate $\ell^* = 1000$.

$MSD^* = 2D^*t^{*\alpha}$. When dealing with macroscopic transport of species inside porous media in applications, it is useful to model the mass transport via convection-diffusion-reaction Eulerian equations for the homogenised volume. When a regular diffusion process ($\alpha = 1$) takes place, the only parameter needed is the mass diffusion coefficient D^* . Nonetheless, when $\alpha \neq 1$ the corresponding Eulerian transport equation consists of nontrivial fractional derivatives [94]. In order to overcome this issue at the practical aim, it is convenient to transform the superdiffusive dispersion process in an equivalent regular dispersion process so as to solve a usual convection-diffusion-reaction equation for the Eulerian homogenised mass transport. However, in order to define an equivalent Gaussian system it is necessary to fix a typical displacement length $\ell^* := \ell/d_f$ that characterises the typical size of the system where the anomalous dispersion process occurs. The equivalent system is then obtained matching the actual Mean Square Displacements calculated at the system size, i.e. $MSD^* = \ell^{*2}$, with the equivalent normal diffusion process characterised by D_{eff}^* . The effective mass diffusivity has thus been derived by imposing the following equality:

$$\ell^{*2} = 2D^*t^{*\alpha} = 2D_{eff}^*t^*, \quad (6.7)$$

from which it follows:

$$D_{eff}^*(\ell^*) = 2^{\frac{1-\alpha}{\alpha}} D^{\frac{1}{\alpha}} \ell^{*2\frac{\alpha-1}{\alpha}} \quad (6.8)$$

Figure 6.9 well depicts the effect of fibers orientation on the streamwise and transverse dispersion. Values of D_{eff}^* are plotted against the mean value of $\cos(\theta)$. While no significant differences on the dispersion coefficient are observed along the transverse direction, an increment of dispersion can be achieved along the streamwise direction by choosing to align fibers preferentially along the streamwise direction. Being the process superdiffusive, the larger the typical system scale, the higher the effective diffusion coefficient. E.g. considering the typical streamwise extension of the system in the order of 1000 fiber diameters, the effective diffusion coefficient becomes 100 times larger than that in the transverse direction.

It should be remarked that the medium with fibers aligned along the flow exhibits the lowest resistance to the flow, i.e. the highest permeability. At practical purposes, it is crucial to define an efficiency in terms of ratio between energy spent to drive the flow and mixing achieved in the porous medium. This efficiency as a function of the preferential orientation of the fibers in the medium can be expressed as an effective Schmidt number Sc which corresponds to the ratio between the effective viscosity and diffusion coefficients:

$$Sc = \frac{v_{eff}^*}{D_{eff}^*}. \quad (6.9)$$

The values of effective Schmidt numbers has been reported in Fig. 6.10 which highlights the dispersion efficiency of the differently oriented media. The lower the Schmidt number, the lower the ratio between the effective viscosity and the effective dispersion. In other words, low Schmidt numbers indicate low drag and high dispersion, which in turn increases the electrodes performances. The values of Sc have been evaluated for the same pressure gradient $\Delta P/L$ rather than for the same Re_f , since the same pressure gradient imposes slightly different Reynolds numbers (Tab. 6.1). This is useful for practical applications since the main tunable parameter in real flow batteries systems is $\Delta P/L$. In other words, the effective Schmidt number indicates how much efficient is the dispersion in the fibrous medium, at a fixed $\Delta P/L$.

It should be noted that the Sc number depends on the fiber Reynolds number since the dimensionless effective viscosity v_{eff}^* is inversely proportional to it, while the dimensionless diffusion coefficient D_{eff}^* is independent of it. From a theoretical point of view, it is interesting to note that the effective Peclet number Pe defined as,

$$Pe = Sc Re_f = \frac{\varepsilon}{K^*} \frac{1}{D_{eff}^*}. \quad (6.10)$$

gets rid of the dependence on the fiber Reynolds number since for viscous flow in porous media the dimensionless permeability is independent of the Reynolds number. Figure 6.11

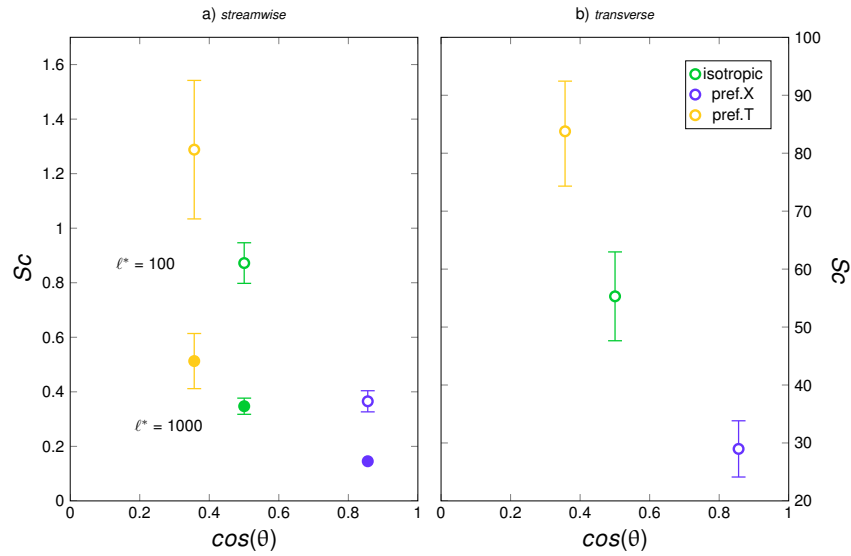


Fig. 6.10 Schmidt number Sc plotted against the mean value of $\cos(\theta)$. Both along the streamwise and transverse directions the medium preferentially oriented along the streamwise direction x presents the lower value of Schmidt number Sc and, consequently, the highest dispersion efficiency.

depicts values of the effective Peclet number. This indicator shows an increase of dispersion efficiency less pronounced but still remarkable.

The behaviour of the Schmidt and Peclet numbers unequivocally show that fibrous media preferentially oriented along the streamwise direction are characterised by higher effective mixing with the lowest pressure loss and appear the optimal configuration for porous electrodes for RFBs.

Effect of the finite Reynolds number on the dispersion

In order to investigate the possible effects of inertia on dispersion dynamics at finite Reynolds number, simulations of flows through isotropic fibrous media have been performed at higher Re number. Interestingly, no significant differences have been found by increasing the Reynolds number up to ≈ 1.0 which can be considered an upper bound for Redox Flow Battery applications. Figure 6.12 shows a comparison between the Mean Square Displacements at $Re \approx 0.1$ and at $Re \approx 1.0$, with the two curves overlapping almost perfectly. Since the Reynolds number range for the present application is $Re = 0.1 \div 1.0$, it can be concluded that the dispersion dynamics on flow batteries does not depend on the Reynolds number and consequently inertial effects are negligible.

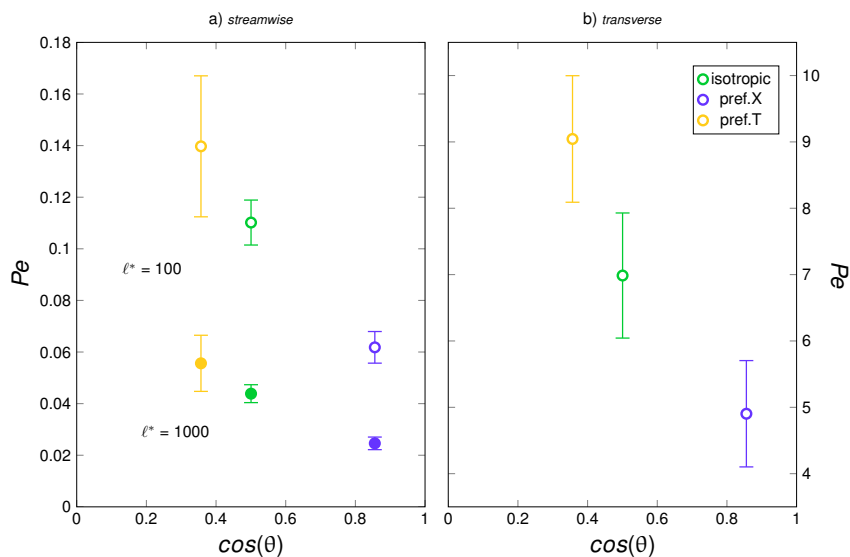


Fig. 6.11 Peclet number Pe plotted against the mean value of $\cos(\theta)$. Both along the streamwise and transverse directions the medium preferentially oriented along the streamwise direction x presents the lowest value of Peclet number.

6.2.4 Remarks

In the present study, the effects of altering the micro-structure of a porous medium composed of fibers have been quantified in terms of permeability and effective dispersion features. In particular, the effect of the fiber orientation has been found to play a major pivotal role not only in the momentum transport behaviour across the medium, but even in the dispersion dynamics. These results are crucial to optimise the fibrous electrodes of Redox-Flow-Batteries.

Microscale modelling of viscous flows through differently oriented fibrous media have been performed by means of a numerical algorithm based on the Lattice-Boltzmann method. Three main categories of fibrous media have been considered: isotropic and preferentially aligned and transverse with the bulk flow. The evolution of passive tracer particles dispersed in the flow has been obtained using a Lagrangian Particle Tracking algorithm.

Results show that, as expected, the permeability value of the medium K^* is increased by preferentially aligning the fibers along the streamwise direction so the overall drag exerted on the flow is diminished. The opposite behaviour is observed for the media with fibers transverse to the flow.

The Mean Square Displacement MSD^* of tracers show different anomalous and regular dispersion behaviours both along the streamwise and transverse directions. Three different regimes have been identified: (i) a ballistic dispersion for very short characteristic times, (ii) a superdiffusive dispersion for intermediate characteristic times and (iii) a still superdiffusive

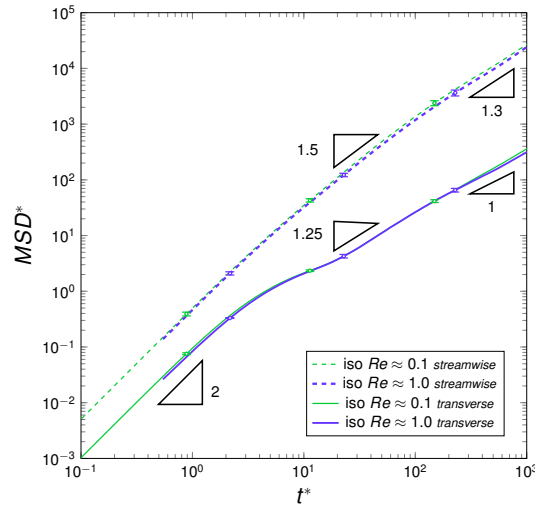


Fig. 6.12 Mean Square Displacement with varying two different finite Reynolds numbers for isotropic fibrous media.

dispersion and a standard Fickian dispersion along the streamwise and transverse directions, respectively, for long characteristic times.

The effect of fiber orientation on the dispersion dynamics has found to be less pronounced in comparison to that on momentum transport. Nevertheless, the medium with fibers preferentially oriented along the streamwise direction shows slightly higher dispersion along both directions. This behaviour has been ascribed to the capability of the latter medium to create pores which could be followed by tracers for longer time in comparison with the isotropic case, since the observed characteristic times of the autocorrelation functions are longer.

Actually, for energy storage applications, such as flow-batteries, the optimal medium should presents both low drag and high dispersion features. Therefore, the values of the effective Schmidt and Peclet numbers which characterise the dispersion efficiency have been determined. The Schmidt numbers give the ratio between the effective diffusion and the overall drag, but depends on the fiber Reynolds number. The Peclet number is instead independent of it. Results clearly show the higher efficiency that can be achieved by aligning the fibers preferentially along the streamwise direction. In particular, by adopting this strategy, one can increase approximately the dispersion efficiency of 60% and 45% along the streamwise and transverse directions, respectively, in terms of Schmidt number, and of 40% and 25% along the streamwise and transverse directions, respectively, in terms of Peclet number, in comparison with an isotropic medium. These numbers can be seen as the fluid mechanics efficiency.

For the sake of completeness, it can be shown that the dimensional effective dispersion coefficients $D_{eff} [m/s]$, evaluated from the calculated dimensionless values D_{eff}^* ,

overwhelm the molecular diffusion coefficients when real electrodes are considered. With regards to All-Vanadium Redox Flow Batteries, the kinematic viscosity and the typical fiber diameter are $\nu_v = 4.4 \cdot 10^{-6} [m^2/s]$ and $d_{fv} = 10 \div 50 [\mu m]$, respectively, whereas the value of typical displacement length ℓ is of the order of centimetres along the stream-wise directions, so that $\ell^* \approx 1000$ [95]. The dispersion coefficients can be thus evaluated as $D_{eff} = D_{eff}^*(\ell^*) Re_f \nu_v$. Along the flow direction the dispersion coefficients are $D_{eff} = 1.5 \cdot 10^{-5} [m^2/s]$ and $D_{eff} = 2.7 \cdot 10^{-5} [m^2/s]$, for the isotropic and the preferentially streamwise-oriented medium, whereas along the transverse direction they result $D_{eff} = 0.96 \cdot 10^{-7} [m^2/s]$ and $D_{eff} = 1.36 \cdot 10^{-7} [m^2/s]$, respectively. It should be noted that the typical molecular diffusion coefficient of Vanadium ions in water is of the order of $D = 10^{-9} \div 10^{-10} [m^2/s]$ so several order of magnitude smaller than the effective diffusion coefficient promoted by the micro-structure of porous media. The results also show that the widely used Bruggeman correction [] to account for the effect of the porosity on the molecular diffusion, $D_b = \varepsilon^{3/2} D$, is negligible for the dispersion of electrolytes in water being $D_b \ll D_{eff}$ ². These considerations highlight the major role of the fibrous medium in the enhancement of mixing in liquids. Finally, the present findings on the effective diffusion can be directly applied to numerically solve advection-dispersion-reaction macroscopic equations for the species flowing in real fibrous media, in order to design optimal electrodes.

²Different is the case when gases in porous media are considered. The typical molecular diffusion of gaseous species is of the order of $10^{-5} [m^2/s]$, so the D_b provides a useful estimate of the effective diffusion being larger than the pore scale induced effective diffusion.

Chapter 7

Conclusions

In the present thesis, a fluid-dynamic numerical analysis of mass and momentum transport mechanisms in fuel cells and flow batteries systems has been presented. The study has been conducted by means of the Lattice-Boltzmann Method, an innovative and promising computational tool for simulating complex multiphysics problems. Several simulations have been performed in order to investigate fundamental physical behaviours of these systems from micro to macroscale. To this end, different Lattice-Boltzmann models have been implemented, tested and validated, depending on the specific case studied: e.g. a two-phase flows model coupled with temperature for studying liquid-vapour transport and phase change phenomena in fuel cells, or a fluid flow model coupled with a Lagrangian Particle Tracking algorithm for studying dispersion of species in flow batteries. It should be stressed that the numerical models used in the present work have been fully implemented in some cases, or improved and expanded in others, by the author, and no commercial software has been utilised, except for the one used in Chapter 5.

Regarding fuel cells, the study has been focused on water management strategies in order to improve fuel cells performances. In Chapter 3, liquid water has been found to preferentially cumulate at the gas channel-diffusion layer interface if it erupts from the catalyst layer in vapour form. Actually this tendency is considered to be promoted by the abrupt change in momentum transport behaviour at the interface which gives rise to laminar separation zones. These regions are therefore considered well suited to host condensation phenomena which should be avoided for obtaining better cell performances. Simulations reveal that increasing the ratio between diffusion layer and gas channel heights diminishes the probability of liquid cumulation at the interface by homogenising the flow field. Consequently, it is believed that gas transport from gas channels to diffusion layers can be enhanced and cell performances increased.

However, in fuel cells, water formed by chemical reactions at the catalyst layer can erupt towards diffusion layers also in liquid form. The dynamics of liquid front imbibition and drainage in porous media is difficult to predict, especially in media composed of fibers with different orientations and wetting conditions. In Chapter 4 this issue has been clarified in order to identify alternative engineering solutions in producing diffusion layers capable of promoting fast liquid removal. Simulations of liquid front imbibition and drainage in fibrous porous media have been performed by varying fibers distribution and orientation as well as wetting properties of microstructure. The imbibition and drainage dynamics have been found to be faster for hydrophilic and hydrophobic media, respectively, as expected. Moreover, the imbibition process has been observed to generally follow the theoretical Lucas-Washburn solution, so that the time-dependent saturation is described by the law $Sat \propto t^{*1/2}$. However, the difficult determination of the capillary radius can lead to wrong prediction when applying the Lucas-Washburn solution. Results confirm that two times the hydraulic radius is a good approximation of the capillary radius in media composed of randomly oriented fibers. Imbibition in highly hydrophobic media has been found to follow a different time-scaling, with $Sat \propto t^{*1/3}$, which reflects a very slow infiltration process caused by a great discontinuity of the liquid front. In order to further enhance the liquid front dynamics, an half hydrophobic/half hydrophilic porous medium has been subjected to imbibition and drainage process. In comparison with fully hydrophilic or hydrophobic media, the latter “two-wetting” medium promotes faster liquid water transport. In the same Chapter 4 simulations of fuel cells with two-wetting diffusion layers have been compared with typical cells equipped with hydrophobic or neutral diffusion layers. In particular their capability of draining the lower part of the cell has been investigated. Results show that by adopting half hydrophobic/half hydrophilic media liquid water removal is tremendously enhanced, suggesting easier through-plane gas transport to the catalyst layer, especially in the lower part of diffusion layers, and higher cell performances.

On the other hand, concerning flow batteries, the focus has been set on macroscopic design of distributing channels and on microstructure effects on dispersion dynamics. Chapter 5 presents results of simulations of electrolyte distribution with varying the design of distributing channels. Among the cases investigated, interdigitated channels have been found to guarantee a good balance between uniformity of the electrolyte distribution and pressure drops. Specifically, the optimal configuration for all-Vanadium Redox Flow Batteries is achieved when the ratios between channels hydraulic radius and cell width and between ribs width and cell width equal approximately $6 \cdot 10^{-3}$ and $8.5 \cdot 10^{-2}$, respectively.

Another key factor for ensuring high performances in flow batteries is mixing of reactants. The higher the mixing and the dispersion inside porous electrodes, the higher the rate of

chemical reactions and, consequently, the current density. In liquid electrolytes molecular dispersion is almost negligible so that dispersion of active species is guaranteed by the porous microstructure. Chapter 6 deals with the effects of fibers orientation on dispersion dynamics. The complex flow field inside differently oriented media has been solved by a Lattice-Boltzmann model. Then, the influence of nematic properties of electrodes on dispersion dynamics has been evaluated by analysing the statistics of five thousand tracers that experience flow. In order to evaluate the fluid-mechanic efficiency of differently oriented media, effective viscosity and dispersion coefficients have been determined for each case. Results show that drag can be significantly reduced and dispersion enhanced by orienting fibers preferentially along the streamwise direction. This finding suggests that anisotropic media oriented preferentially along the main direction of the flow are able to correlate the motion of tracers for longer time in comparison with isotropic media and, in addition, their permeabilities are significantly higher. The fluid-mechanics efficiency of flow batteries in terms of amount of power spent for mixing has been found to be significantly increased along both streamwise and transverse directions.

Results of the present thesis work had clarified some fundamental physical phenomena happening inside fuel cells and flow batteries systems. They give some guideline for improving both technologies and provide innovative engineering solutions that can be experimentally tested in real industrial systems.

List of figures

1.1	Sketch of a fuel cell.	3
1.2	Polarisation curve of a cell. The activation and mass transport losses are highlighted.	4
1.3	Schematic outline of the present thesis.	7
2.1	Two-dimensional lattice cell in LGCA and in LBM	14
2.2	Example of collision in LGCA	15
2.3	The 92-neighbours fluid sites of the two-belt three dimensional lattice; the dark and grey circles indicate sites belonging to the first and second belt respectively.	20
2.4	One-dimensional example of interpolation algorithm.	23
2.5	Flow field (left panel) and shear stress partitioning (right panel). At the bottom the total wall shear stress calculated from the LB flow field is correctly balancing the stresses computed in the medium, as predicted by the VANS equation.	25
2.6	Non-dimensional permeability K/d_f^2 against porosity ϵ compared with the theoretical solution of Gebart et al.	27
2.7	Gas volume void fraction ϵ_{gas} plotted with the vapour quality Q	28
2.8	Left panel: condensed film thickness δ_{film} plotted with distance x . The numerical solution is well overlapping the theoretical solution of Asano et al. Right panel: the slope of the curve represents the latent heat λ_h which is approximately constant along the film thickness.	29
3.1	Characteristic length scales in fuel cells.	32
3.2	Sketch of the simulation domain $h = 0.3$, $d_p = 33 \mu\text{m}$, $d_s = 67 \mu\text{m}$, $\phi = 0.69$ and density fields at the equilibrium. The darker zones indicate liquid density.	34
3.3	Scheme of GC and GDL cross section of a PEMFC. The dashed lines indicate the simulation domain cross-sectional area.	35

3.4	Comparison between the Lattice-Boltzmann EOS and the Rimbach and Chatterjee EOS. The square-shaped markers indicate the gas (i.e. $\rho_{gas} \sim 0.028$) and liquid (i.e. $\rho_{liq} \sim 2.5$) equilibrium phases at P_{sat}	37
3.5	Number of liquid sites over total fluid sites versus the relative GDL height $h = H_{GDL}/H$: (a) for a fixed pressure gradient and (b) for a fixed Reynolds number in the GC.	38
3.6	Number of liquid sites over total fluid sites in the Transition Layer (TL) versus the relative GDL height $h = H_{GDL}/H$: (a) for a fixed pressure gradient and (b) for a fixed Reynolds number in the GC.	39
3.7	Liquid-phase fluid sites location in the cross-sectional area and transition layer location for three different values of the relative GDL height h : (a) $h = 0.3$, (b) $h = 0.6$ and (c) $h = 0.9$	40
3.8	mean density values of sites that overcome the initial metastable density value in the TL and in the whole domain with varying the relative GDL height h for: (a) $\phi = 0.69$, $dp = 33\mu\text{m}$, $ds = 67\mu\text{m}$ AND (b) $\phi = 0.84$, $dp = 50\mu\text{m}$, $ds = 50\mu\text{m}$	41
4.1	a) Polarisation curve and possible mass losses due to pores blocked by FEP; b) sketch of FEP blocking pores as in the experimental observation of Lim and Wang.	44
4.2	a) Capillary imbibition model. b) Real porous medium imbibition; the blue surface represent the liquid-vapour interface	46
4.3	Forcing pressure gradient $\Delta P/L$ and equilibrium contact angle θ values for all the considered cases of initial imbibition in lattice units.	48
4.4	Characteristic velocity $U_{\Delta P}$ plotted against the other characteristic velocity of the system U_{γ} . Cross, triangle and circle markers indicates no infiltration, slow infiltration and fast infiltration, respectively. Yellow, red and violet markers refer to hydrophobic media while blue and green markers refer to "neutral" and hydrophilic media, respectively.	49
4.5	Neutral and hydrophilic cases. Dimensionless permeability values K/d_f^2 for gas phase plotted against the dimensionless permeability for the liquid phase. Values gather around the dashed lines (the bisection $y = x$), indicating similar velocities of the phases and uniform fronts for low values. For higher values of permeability the front is broken up.	50
4.6	Hydrophobic case. Dimensionless permeability values K/d_f^2 for gas phase plotted against the dimensionless permeability for the liquid phase.	51

4.7	Different cases of imbibition dynamics with varying the forcing and the hydrophobicity, i.e. the ratio $U_\gamma/U_{\Delta P}$; a) $U_\gamma/U_{\Delta P} = -0.58$ imbibition with continuous front, b) $U_\gamma/U_{\Delta P} = -1.6$ no infiltration, c) $U_\gamma/U_{\Delta P} = 0$ fast imbibition with broken front, d) $U_\gamma/U_{\Delta P} = -0.83$ imbibition with broken front and gas trapped.	52
4.8	Saturation against non-dimensional time t^* for three different geometries of the porous medium. In all the three cases the contact angle is $\theta = 90^\circ$	53
4.9	The three different geometries considered for imbibition simulation without wetting, i.e. $U_\gamma = 0$	54
4.10	Spontaneous imbibition dynamics. The first part of the curve approaches a law linearly dependent on time, while the second part approaches the Lucas-Washburn theoretical solution. Inset: spontaneous drainage with an hydrophobic medium.	56
4.11	Imbibition dynamics with varying the hydrophobicity of the medium. Neutral (cyan) and hydrophilic (magenta) media saturation dynamics can be described by the Lucas-Washburn law, while the hydrophobic medium (orange) follows a different time scaling with $Sat \approx 1/3t^{*1/3}$. Inset: drainage dynamics of the same media.	58
4.12	The liquid front in the neutral (left panel) and hydrophobic (right panel) medium. The front infiltration is more discontinuous in the hydrophobic medium with pores being clogged: this behaviour is considered to be responsible of the different time scaling of the imbibition process.	59
4.13	Double-wetting layer with the first and second part hydrophobic ($\theta = 120^\circ$) and hydrophilic ($\theta = 60^\circ$), respectively, compared with a neutral, fully hydrophilic and fully hydrophobic medium. The time spent for a complete imbibition-drainage cycle is smaller for the double-wetting case.	60
4.14	Non-dimensional system temperature T/T_0 variation in time during imbibition (left panel) and drainage (right panel).	62
4.15	Non-dimensional liquid mass $m_{liq}/m_{liq,0}$ variation as function of the non-dimensional system temperature T/T_0	63

4.16	Three different cases of GDL wetting: on the left, a neutral (no wetting) medium; on the centre, a hydrophobic medium; on the right, a half hydrophobic/half hydrophilic medium. The GDL is in contact with both the channel and the ribs of the upper plate. At the initial stage of the simulation the bottom of the GDL is filled with liquid water in order to simulate a possible condition of condensation of the cell. The lower wall is super-hydrophobic, in order to simulate the MPL.	64
4.17	The fuel cell simulated with the lowest part of GDL filled with liquid water. The imbibition and drainage process of the low part of GDL highlighted in black has been studied.	65
4.18	Imbibition and drainage of the low part of the GDL: the red curve indicates the case with two-wetting GDL with oriented fibers, which is the more efficient case in removing the liquid water.	66
5.1	The carbon felt with distribution channels (configuration 1).	70
5.2	The velocity field in (m s^{-1}) of the 5x6 1 mm h.d. (a), 5x6 2 mm h.d. (b), 4x4 2 mm h.d. (c) configurations with indirect feeding and the velocity field with direct feeding (d).	74
5.3	Red lines along which the velocity profiles are calculated. The index i , equal to 1, 2 or 3, is referred to 25%, 50%, 75% of depth inside the felt (configuration 3).	74
5.4	Planar velocity profiles calculated along the lines of Fig.3 (left side) and velocity distribution (right side) for the 5x6 1 mm h.d. (a), 5x6 2 mm h.d. (b) 4x4 2 mm h.d. (c) configuration with indirect feeding.	76
5.5	Planar velocity profiles calculated along the lines of Fig.3 (left side) and velocity distribution (right side) for the configuration with direct feeding.	77
5.6	Planar velocity streamlines in (m s^{-1}) for the three configurations with indirect feeding (5x6 1 mm h.d. (a), 5x6 2 mm h.d. (b), 4x4 2 mm h.d. (c)) and for the one with direct feeding (d).	79
6.1	Left Panel: dimensionless permeability values for different cases of porosity ε and orientation. Results gather around the predicted value of the Blake-Kozeny equation, as expected. It should be pointed out that the permeability values diminish as the porosity increases, a trend already observed in Whitaker 1996. Right Panel: drag coefficients $Drag^* = 2r_s^2/(9K) 1/(1 - \varepsilon)$ from numerical simulations of flows through single packed-bed of spheres of radius r_s compared with results of Zick and Homsby.	84

- 6.2 Left Panels: Triperiodic cubic domains generated by numerical modelling where particles are randomly injected and advected by the steady flow field in the porous medium. Three main different orientations have been considered: a) an isotropic medium; b) a medium preferentially oriented along the streamwise direction x ; c) a medium preferably oriented along the transverse directions y and z . The medium is considered preferentially oriented along the streamwise or transverse direction when all the angles θ formed by the axes of the fibers and the x axis are lower or higher than $\pi/4$, respectively. Right Panel: probability distribution functions of $\cos(\theta)$ for different fibrous media. 86
- 6.3 Dimensionless permeability (left panel) and effective viscosity (i.e. v_{eff}^* , right panel), for the three main fiber orientations, plotted against the mean value of $\cos(\theta)$. The effective viscosity is considerably reduced in the media preferentially oriented along the streamwise direction, indicating a significant reduction of the drag exerted on the medium, and, in turn, of the pressure drop. 88
- 6.4 Hydraulic diameter D_h and length ℓ_f of a “tilted” pore and their projections along the streamwise direction D_{hx} and ℓ_{fx} 89
- 6.5 Dimensionless Mean Square Displacement against dimensionless time t^* along the streamwise (MSD_x^* , dashed lines) and transverse (MSD_t^* , solid lines) directions. Three main regimes can be distinguished: 1) a ballistic dispersion for short times; 2) a superdiffusive dispersion for intermediate times; 3) a still superdiffusive dispersion along the streamwise direction and a Fickian standard dispersion along the transverse direction, i.e. $MSD_t^* \propto t$, for long times. The difference in the three main regimes is highlighted in the inset which shows the ratio $MSD^*/t^{*1.25}$ approaching a constant value in the second and third regime along the transverse and streamwise direction, respectively. 91

- 6.6 Dimensionless velocity autocorrelation c'_{v^*} against dimensionless time t^* along the streamwise (c'_{vx^*} , dashed lines) and transverse (c'_{vt^*} , solid lines) directions. The autocorrelation approaches zero along the transverse direction for long characteristic times, i.e. in the third regime observed. The figure highlights that the streamwise-oriented medium presents higher velocity autocorrelations not only along the streamwise direction (as expected since fibers are aligned with the main flow), but also in the transverse direction. The inset represents velocity autocorrelations along the streamwise direction in log-log plot: it can be observed that c'_{vx^*} decreases proportionally to $t^{*-0.7}$ towards the end, which in turn corresponds to an increasing of the $MSD_x^* \propto t^{*1.3}$ 93
- 6.7 Probability distribution functions (PDF) of dimensionless displacement fluctuations, $dx'^* = (dx - \langle dx \rangle) / \sigma(dx)$ (where $\sigma(dx)$ is the variance), along the streamwise direction, for different fiber orientations. (a) PDF at $t^* = 0$; (b) PDF at $t^* = 10$; (c) PDF at $t^* = 100$; (d) PDF at $t^* = 500$ 95
- 6.8 Probability distribution functions of dimensionless displacement fluctuations, $(dy'^* + dz'^*)/2 = ((dy - \langle dy \rangle) / \sigma(dy) + (dz - \langle dz \rangle) / \sigma(dz)) / 2$ (where σ is the variance), along the transverse direction, for different fiber orientations. (a) PDF at $t^* = 0$; (b) PDF at $t^* = 10$; (c) PDF at $t^* = 100$; (d) PDF at $t^* = 500$ 96
- 6.9 Dimensionless equivalent effective dispersion coefficients D_{eff}^* plotted against the mean value of $\cos(\theta)$, for different cases of fibers orientation, along the streamwise (left panel) and transverse (right panel) direction. In left panel void marks indicate a characteristic displacement length $\ell^* = \ell/d_f = 100$, whereas filled ones indicate $\ell^* = 1000$ 97
- 6.10 Schmidt number Sc plotted against the mean value of $\cos(\theta)$. Both along the streamwise and transverse directions the medium preferentially oriented along the streamwise direction x presents the lower value of Schmidt number Sc and, consequently, the highest dispersion efficiency. 99
- 6.11 Peclet number Pe plotted against the mean value of $\cos(\theta)$. Both along the streamwise and transverse directions the medium preferentially oriented along the streamwise direction x presents the lowest value of Peclet number. 100
- 6.12 Mean Square Displacement with varying two different finite Reynolds numbers for isotropic fibrous media. 101

List of tables

3.1	Parameters used in the four sets of simulations> in each set the relative height has been varied within the range $h = 0.3 - 0.9$	36
4.1	Liquid water transport efficiency of different media.	61
5.1	Selected configurations for the distribution of the electrolyte.	70
5.2	Values of the parameters adopted in Eq.(5.1)	71
5.3	78
6.1	Fiber Reynolds numbers and dimensionless root mean square velocities along the streamwise, $\langle u_x'^2 \rangle / U^2$, and transverse, $\langle u_t'^2 \rangle / U^2$, directions, for different fiber orientations.	87

References

- [1] European Commission. Proposal for a council decision establishing the specific programme implementing horizon 2020 – the framework programme for research and innovation (2014-2020). *COM(2011)*, 811(Final), 2011.
- [2] Martin Winter and Ralph J Brodd. What are batteries, fuel cells, and supercapacitors? *Chemical reviews*, 104(10):4245–4270, 2004.
- [3] Matthew M Mench. *Fuel cell engines*. John Wiley & Sons, 2008.
- [4] Piergiorgio Alotto, Massimo Guarnieri, and Federico Moro. Redox flow batteries for the storage of renewable energy: A review. *Renewable and Sustainable Energy Reviews*, 29:325–335, 2014.
- [5] S Maass, F Finsterwalder, G Frank, R Hartmann, and C Merten. Carbon support oxidation in pem fuel cell cathodes. *Journal of Power Sources*, 176(2):444–451, 2008.
- [6] ZH Wang, CY Wang, and KS Chen. Two-phase flow and transport in the air cathode of proton exchange membrane fuel cells. *Journal of Power Sources*, 94(1):40–50, 2001.
- [7] Chao-Yang Wang. Fundamental models for fuel cell engineering. *Chemical reviews*, 104(10):4727–4766, 2004.
- [8] Peter K Kang, Pietro Anna, Joao P Nunes, Branko Bijeljic, Martin J Blunt, and Ruben Juanes. Pore-scale intermittent velocity structure underpinning anomalous transport through 3-d porous media. *Geophysical Research Letters*, 41(17):6184–6190, 2014.
- [9] Toshihiko Yoshida and Koichi Kojima. Toyota mirai fuel cell vehicle and progress toward a future hydrogen society. *The Electrochemical Society Interface*, 24(2):45–49, 2015.
- [10] Adam Z Weber, Matthew M Mench, Jeremy P Meyers, Philip N Ross, Jeffrey T Gostick, and Qinghua Liu. Redox flow batteries: a review. *Journal of Applied Electrochemistry*, 41(10):1137–1164, 2011.
- [11] Antonino Salvatore Arico, Peter Bruce, Bruno Scrosati, Jean-Marie Tarascon, and Walter Van Schalkwijk. Nanostructured materials for advanced energy conversion and storage devices. *Nature materials*, 4(5):366–377, 2005.
- [12] Ki Jae Kim, Min-Sik Park, Young-Jun Kim, Jung Ho Kim, Shi Xue Dou, and M Skyllas-Kazacos. A technology review of electrodes and reaction mechanisms in vanadium redox flow batteries. *Journal of Materials Chemistry A*, 3(33):16913–16933, 2015.

-
- [13] S. Succi. *The Lattice Boltzmann Equation: for Fluid Dynamics and Beyond*. Oxford University Press, 2001.
- [14] Guy McNamara and Berni Alder. Analysis of the lattice boltzmann treatment of hydrodynamics. *Physica A: Statistical Mechanics and its Applications*, 194(1):218–228, 1993.
- [15] Uriel Frisch, Brosl Hasslacher, and Yves Pomeau. Lattice-gas automata for the navier-stokes equation. *Physical review letters*, 56(14):1505, 1986.
- [16] Guy R McNamara and Gianluigi Zanetti. Use of the boltzmann equation to simulate lattice-gas automata. *Physical Review Letters*, 61(20):2332, 1988.
- [17] FJ Higuera et al. Boltzmann approach to lattice gas simulations. *EPL (Europhysics Letters)*, 9(7):663, 1989.
- [18] YH Qian, Dominique d’Humières, and Pierre Lallemand. Lattice bgk models for navier-stokes equation. *EPL (Europhysics Letters)*, 17(6):479, 1992.
- [19] Dominique d’Humières and Irina Ginzburg. Viscosity independent numerical errors for lattice boltzmann models: From recurrence equations to “magic” collision numbers. *Computers & Mathematics with Applications*, 58(5):823–840, 2009.
- [20] Zhaoli Guo, Chuguang Zheng, and Baochang Shi. Discrete lattice effects on the forcing term in the lattice boltzmann method. *Physical Review E*, 65(4):046308, 2002.
- [21] P. Yuan and L. Schaefer. Equations of state in a lattice boltzmann model. *Physics of Fluids*, 18(4), 2006. article no. 042101.
- [22] X. Shan and H. Chen. Lattice boltzmann model for simulating flows with multiple phases and components. *Physical Review E*, 47(3):1815–1819, 1193.
- [23] G. Falcucci, Gino Bella, G. Chiatti, S. Chibbaro, M. Sbragaglia, and S. Succi. Lattice boltzmann models with mid-range interactions. *Communications in Computational Physics*, 2(6):1071–1084, 2007.
- [24] M. Sbragaglia, R. Benzi, L. Biferale, S. Succi, K. Sugiyama, and F. Toschi. Generalized lattice boltzmann method with multirange pseudopotential. *Physical Review E*, 75(2), 2007. article no. 026702.
- [25] Peng Yuan and Laura Schaefer. A thermal lattice boltzmann two-phase flow model and its application to heat transfer problems—part 1. theoretical foundation. *Journal of Fluids Engineering*, 128(1):142–150, 2006.
- [26] L Biferale, P Perlekar, M Sbragaglia, and F Toschi. Simulations of boiling systems using a lattice boltzmann method. *Communications in Computational Physics*, 13(03):696–705, 2013.
- [27] Junfeng Zhang and Fuzhi Tian. A bottom-up approach to non-ideal fluids in the lattice boltzmann method. *EPL (Europhysics Letters)*, 81(6):66005, 2008.

- [28] M'hamed Bouzidi, Mouaouia Firdaouss, and Pierre Lallemand. Momentum transfer of a boltzmann-lattice fluid with boundaries. *Physics of Fluids (1994-present)*, 13(11):3452–3459, 2001.
- [29] Vladimir Nikora, Ian McEwan, Stephen McLean, Stephen Coleman, Dubravka Pokrajac, and Roy Walters. Double-averaging concept for rough-bed open-channel and overland flows: Theoretical background. *Journal of Hydraulic Engineering*, 133(8):873–883, 2007.
- [30] BR Gebart. Permeability of unidirectional reinforcements for rtm. *Journal of composite materials*, 26(8):1100–1133, 1992.
- [31] Wilhelm Nusselt. Die oberflächen kondensatin des wasser dampfes. *Zeitschrift des Vereines Deutscher Ingenieure*, 60(27):541–546, 1916.
- [32] KOICHI ASANO, YOSHIMI NAKANO, and MASASHI INABA. Forced convection film condensation of vapors in the presence of noncondensable gas on a small vertical flat plate. *Journal of Chemical Engineering of Japan*, 12(3):196–202, 1979.
- [33] A. Bazylak. Liquid water visualization in pem fuel cells: A review. *International Journal of Hydrogen Energy*, 34(9):3845–3857, 2009.
- [34] M. Yamauchi, K. Sugiura, T. Yamauchi, T. Taniguchi, and Y. Itoh. Proposal for an optimum water management method using two-pole simultaneous measurement. *Journal of Power Sources*, 193(1):1–8, 2009.
- [35] S. Ge and C. Y. Wang. Liquid water formation and transport in the pefc anode. *Journal of the Electrochemical Society*, 154(10):B998–B1005, 2007.
- [36] J. B. Siegel, D. A. Mckay, A. G. Stefanopoulou, D. S. Hussey, and D. L. Jacobson. Measurement of liquid water accumulation in a pemfc with dead-ended anode. *Journal of the Electrochemical Society*, 155(11):B1168–B1178, 2008.
- [37] C. Hartnig, I. Manke, R. Kuhn, N. Kardjilov, J. Banhart, and Werner Lehnert. Cross-sectional insight in the water evolution and transport in polymer electrolyte fuel cells. *Applied Physics Letters*, 92(13), 2008. Article no. 134106.
- [38] X. Li, I. Sabir, and J. Park. A flow channel design procedure for pem fuel cells with effective water removal. *Journal of Power Sources*, 163(2):933–942, 2007.
- [39] A. Turhan, K. Heller, J. S. Brenizer, and M. M. Mench. Passive control of liquid water storage and distribution in a pefc through flow-field design. *Journal of Power Sources*, 180(2):773–783, 2008.
- [40] A. K. Srouji, L. J. Zheng, R. Dross, A. Turhan, and M. M. Mench. Performance and mass transport in open metallic element architecture fuel cells at ultra-high current density. *Journal of Power Sources*, 218:341–347, 2012.
- [41] J. A. Ochoa-Tapia and S. Whitaker. Momentum transfer at the boundary between a porous medium and a homogeneous fluid. i. theoretical development. *International Journal of Heat and Mass Transfer*, 38(14):2635–2646, 1995.

- [42] J. A. Ochoa-Tapia and S. Whitaker. Momentum transfer at the boundary between a porous medium and a homogeneous fluid. ii. comparison with experiment. *International Journal of Heat and Mass Transfer*, 38(14):2647–2655, 1995.
- [43] C. Manes, D. Pokrajac, I. McEwan, and V. Nikora. Turbulence structure of open channel flows over permeable and impermeable beds: A comparative study. *Physics of Fluids*, 21(12), 2009. Article no. 125109.
- [44] A. Nabovati and C. H. Amon. Hydrodynamic boundary condition at open-porous interface: A pore-level lattice boltzmann study. *Transport in Porous Media*, 96(1):83–95, 2013.
- [45] D. Maggiolo, P. Alotto, A. Marion, and M. Guarnieri. Lattice-boltzmann-based model for the channel-porous interface of pemfc. *Proceedings of EFC2013 - Fifth European Fuel Cell Technology and Applications Conference - Piero Lunghi Conference*, 2013.
- [46] R. Benzi, L. Biferale, M. Sbragaglia, S. Succi, and F. Toschi. Mesoscopic modeling of a two-phase flow in the presence of boundaries: The contact angle. *Physical Review E*, 74(2), 2006. article no. 021509.
- [47] H. Rimbach and N. D. Chatterjee. Equations of state for h_2 , h_2O , and $\text{h}_2\text{-h}_2\text{O}$ fluid mixtures at temperatures above 0.01°C and at high-pressures. *Physics and Chemistry of Minerals*, 14(6):560–569, 1987.
- [48] S. Chibbaro. Capillary filling with pseudo-potential binary lattice-boltzmann model. *The European Physical Journal E*, 27(1):99–106, 2008.
- [49] Zhigang Qi and Arthur Kaufman. Improvement of water management by a microporous sublayer for pem fuel cells. *Journal of Power Sources*, 109(1):38–46, 2002.
- [50] Ugur Pasaogullari, Chao-Yang Wang, and Ken S Chen. Two-phase transport in polymer electrolyte fuel cells with bilayer cathode gas diffusion media. *Journal of the Electrochemical Society*, 152(8):A1574–A1582, 2005.
- [51] Chan Lim and CY Wang. Effects of hydrophobic polymer content in gdl on power performance of a pem fuel cell. *Electrochimica Acta*, 49(24):4149–4156, 2004.
- [52] Gu-Gon Park, Young-Jun Sohn, Tae-Hyun Yang, Young-Gi Yoon, Won-Yong Lee, and Chang-Soo Kim. Effect of ptfе contents in the gas diffusion media on the performance of pemfc. *Journal of Power Sources*, 131(1):182–187, 2004.
- [53] Kui Jiao and Xianguo Li. Water transport in polymer electrolyte membrane fuel cells. *Progress in Energy and Combustion Science*, 37(3):221–291, 2011.
- [54] Martin Blunt, Michael J King, and Harvey Scher. Simulation and theory of two-phase flow in porous media. *Physical Review A*, 46(12):7680, 1992.
- [55] DG Avraam and AC Payatakes. Flow regimes and relative permeabilities during steady-state two-phase flow in porous media. *Journal of Fluid Mechanics*, 293:207–236, 1995.

- [56] Jean-Baptiste Gorce, Ian J Hewitt, and Dominic Vella. Capillary imbibition into converging tubes: Beating washburn's law and the optimal imbibition of liquids. *Langmuir*, 32(6):1560–1567, 2016.
- [57] Jeffrey T Gostick, Michael W Fowler, Marios A Ioannidis, Mark D Pritzker, Yu M Volfkovich, and A Sakars. Capillary pressure and hydrophilic porosity in gas diffusion layers for polymer electrolyte fuel cells. *Journal of Power Sources*, 156(2):375–387, 2006.
- [58] Edward W Washburn. The dynamics of capillary flow. *Physical review*, 17(3):273, 1921.
- [59] N Fries and M Dreyer. The transition from inertial to viscous flow in capillary rise. *Journal of colloid and interface science*, 327(1):125–128, 2008.
- [60] Alexandre Ponomarenko, David Quéré, and Christophe Clanet. A universal law for capillary rise in corners. *Journal of Fluid Mechanics*, 666:146–154, 2011.
- [61] Alain Siebold, Michel Nardin, Jacques Schultz, André Walliser, and Max Oppliger. Effect of dynamic contact angle on capillary rise phenomena. *Colloids and surfaces A: Physicochemical and engineering aspects*, 161(1):81–87, 2000.
- [62] Ahmed Hamraoui and Tommy Nylander. Analytical approach for the lucas–washburn equation. *Journal of colloid and interface science*, 250(2):415–421, 2002.
- [63] Yakov Pachepsky, Dennis Timlin, and Walter Rawls. Generalized richards' equation to simulate water transport in unsaturated soils. *Journal of Hydrology*, 272(1):3–13, 2003.
- [64] Álvaro Cunha, Jorge Martins, Nuno Rodrigues, and FP Brito. Vanadium redox flow batteries: a technology review. *International Journal of Energy Research*, 39(7):889–918, 2015.
- [65] Carlos Ponce de León Albarrán, Ángel Frías Ferrer, José González García, DA Szánto, and Frank C Walsh. Redox flow cells for energy conversion. *Journal of Power Sources*, 2005.
- [66] Zhongbao Wei, Jiyun Zhao, Maria Skyllas-Kazacos, and Binyu Xiong. Dynamic thermal-hydraulic modeling and stack flow pattern analysis for all-vanadium redox flow battery. *Journal of Power Sources*, 260:89–99, 2014.
- [67] Qian Xu, TS Zhao, and PK Leung. Numerical investigations of flow field designs for vanadium redox flow batteries. *Applied energy*, 105:47–56, 2013.
- [68] Christian Blanc and Alfred Rufer. Multiphysics and energetic modeling of a vanadium redox flow battery. In *2008 IEEE International Conference on Sustainable Energy Technologies*, pages 696–701. IEEE, 2008.
- [69] Zhijiang Tang, Douglas S Aaron, Alexander B Papandrew, and Thomas A Zawodzinski. Monitoring the state of charge of operating vanadium redox flow batteries. *ECS Transactions*, 41(23):1–9, 2012.

- [70] Ao Tang, Simon Ting, Jie Bao, and Maria Skyllas-Kazacos. Thermal modelling and simulation of the all-vanadium redox flow battery. *Journal of Power Sources*, 203:165–176, 2012.
- [71] Yunpu Zhai, Yuqian Dou, Dongyuan Zhao, Pasquale F Fulvio, Richard T Mayes, and Sheng Dai. Carbon materials for chemical capacitive energy storage. *Advanced materials*, 23(42):4828–4850, 2011.
- [72] S Bortolin, P Toninelli, D Maggiolo, M Guarnieri, and D Del Col. Cfd study on electrolyte distribution in redox flow batteries. In *Journal of Physics: Conference Series*, volume 655, page 012049. IOP Publishing, 2015.
- [73] Stephen Whitaker. The forchheimer equation: a theoretical development. *Transport in Porous media*, 25(1):27–61, 1996.
- [74] Graham W Jackson and David F James. The permeability of fibrous porous media. *The Canadian Journal of Chemical Engineering*, 64(3):364–374, 1986.
- [75] Matteo Icardi, Gianluca Boccardo, Daniele L Marchisio, Tiziana Tosco, and Rajandrea Sethi. Pore-scale simulation of fluid flow and solute dispersion in three-dimensional porous media. *Physical Review E*, 90(1):013032, 2014.
- [76] Shlomo P Neuman. Universal scaling of hydraulic conductivities and dispersivities in geologic media. *Water Resources Research*, 26(8):1749–1758, 1990.
- [77] Stephen Whitaker. The method of volume averaging. theory and applications of transport in porous media. *The Netherlands Kluwer Academic*, 1999.
- [78] Céline Bruderer and Yves Bernabé. Network modeling of dispersion: Transition from taylor dispersion in homogeneous networks to mechanical dispersion in very heterogeneous ones. *Water Resources Research*, 37(4):897–908, 2001.
- [79] Shlomo P Neuman and Daniel M Tartakovsky. Perspective on theories of non-fickian transport in heterogeneous media. *Advances in Water Resources*, 32(5):670–680, 2009.
- [80] Brian Berkowitz and Harvey Scher. On characterization of anomalous dispersion in porous and fractured media. *Water Resources Research*, 31(6):1461–1466, 1995.
- [81] Donald L Koch and John F Brady. Anomalous diffusion in heterogeneous porous media. *Physics of Fluids (1958-1988)*, 31(5):965–973, 1988.
- [82] Brian D Wood, Fabien Cherblanc, Michel Quintard, and Stephen Whitaker. Volume averaging for determining the effective dispersion tensor: Closure using periodic unit cells and comparison with ensemble averaging. *Water resources research*, 39(8), 2003.
- [83] Monica Moroni and John H Cushman. Three-dimensional particle tracking velocimetry studies of the transition from pore dispersion to fickian dispersion for homogeneous porous media. *Water Resources Research*, 37(4):873–884, 2001.
- [84] Bo Wang, James Kuo, Sung Chul Bae, and Steve Granick. When brownian diffusion is not gaussian. *Nature Materials*, 11(6):481–485, 2012.

-
- [85] M Bayani Cardenas. Three-dimensional vortices in single pores and their effects on transport. *Geophysical Research Letters*, 35(18), 2008.
- [86] Mark M Meerschaert, David A Benson, and Boris Baeumer. Operator lévy motion and multiscaling anomalous diffusion. *Physical Review E*, 63(2):021112, 2001.
- [87] P Castiglione, Andrea Mazzino, P Muratore-Ginanneschi, and A Vulpiani. On strong anomalous diffusion. *Physica D: Nonlinear Phenomena*, 134(1):75–93, 1999.
- [88] S Torquato and CLY Yeong. Universal scaling for diffusion-controlled reactions among traps. *methods*, 13:20–23, 1997.
- [89] Manolis M Tomadakis and Teri J Robertson. Pore size distribution, survival probability, and relaxation time in random and ordered arrays of fibers. *The Journal of chemical physics*, 119(3):1741–1749, 2003.
- [90] AA Zick and GM Homsy. Stokes flow through periodic arrays of spheres. *Journal of fluid mechanics*, 115:13–26, 1982.
- [91] Dario Maggiolo, Costantino Manes, and Andrea Marion. Momentum transport and laminar friction in rough-wall duct flows. *Physics of Fluids (1994-present)*, 25(9):093603, 2013.
- [92] Francis AL Dullien. *Porous media: fluid transport and pore structure*. Academic press, 2012.
- [93] Peter K Kang, Marco Dentz, Tanguy Le Borgne, and Ruben Juanes. Anomalous transport on regular fracture networks: Impact of conductivity heterogeneity and mixing at fracture intersections. *Physical Review E*, 92(2):022148, 2015.
- [94] Rina Schumer, David A Benson, Mark M Meerschaert, and Stephen W Wheatcraft. Eulerian derivation of the fractional advection–dispersion equation. *Journal of Contaminant Hydrology*, 48(1):69–88, 2001.
- [95] Ao Tang, Jie Bao, and Maria Skyllas-Kazacos. Studies on pressure losses and flow rate optimization in vanadium redox flow battery. *Journal of power sources*, 248:154–162, 2014.